



HORIZON 2020  
THEME SC5-2017



---

European Climate Prediction system

(Grant Agreement 776613)

**European Climate Prediction system (EUCP)**

**Deliverable D4.3**

***Outlook of future hazards***

Deliverable Title	<i>Outlook of future hazards</i>	
Brief Description	<i>Ensemble-based outlook of trends in (cross)-sectoral indicators: Develop sectoral and cross-sectoral indicators to assess future hydro-meteorological risks (e.g., flash flood, river flood, storm surge, coastal erosion, wind droughts) at various spatial scales relevant to end users in support of monitoring SDGs 13 and 6</i>	
WP number	4	
Lead Beneficiary	<i>Frederiek Sperna Weiland, Deltares Albrecht Weerts, Deltares</i>	
Contributors	<i>Peter Greve, IIASA Shuang Yu, IPSL Robert Vautard, IPSL Jaroslav Mysiak, CMCC Carlos Delgado-Torres, BSC Balakrishnan Solaraju-Murali, BSC Panos Athanasiou, Deltares Marjanne Zander, Deltares</i>	
Creation Date	10-02-2022	
Version Number	1.0	
Version Date	14-02-2022	
Deliverable Due Date	28/02/2022	
Actual Delivery Date	25/02/2022	
Nature of the Deliverable	X	<i>R – Report</i>
		<i>P – Prototype</i>
		<i>D - Demonstrator</i>
		<i>O – Other</i>
Dissemination Level/ Audience	PU	<i>PU – Public</i>
		<i>PP - Restricted to other programme participants, including the Commission services</i>
		<i>RE - Restricted to a group specified by the consortium, including the Commission services</i>
		<i>CO - Confidential, only for members of the consortium, including the Commission services</i>

Version	Date	Modified by	Comments
0.9	14-2-2022	Frederiek Sperna Weiland	Draft for WP4 internal review
0.91	14-2-2022	Albrecht Weerts / Frederiek Sperna Weiland	Concept version shared with UKMO for review
0.92	23-2-2022		Review Carol McSweeney UKMO
1.0	25-2-2022	Frederiek Sperna Weiland	Improved based upon review comments UKMO



**Table of contents**

1	Executive summary.....	5
2	Project objectives.....	8
3	Detailed report.....	9
3.1	Assessing future changes in flash flood frequency and occurrence over the European Alps.....	10
3.2	Long term variation and projection of hub-height wind speed in Europe during twenty-first century.....	16
3.3	Attribution of winter wind energy drought in Europe.....	21
3.4	Sandy beach erosion induced by sea level rise.....	26
3.5	Efficient dune erosion prediction at the Dutch coast.....	33
3.6	Multi-year forecast of drought and heat stress condition over global wheat harvesting region.....	38
3.7	Multi-year forecast of surface wind.....	43
3.8	Projected streamflow changes for Europe from an ensemble of climate and hydrological models.....	50
3.9	Ensemble hydrological impact simulations and projections under different forcing.....	56
3.10	Pluvial flood hazard and risk, and risk reduction measures – city of Milan 64	
3.11	Projected impacts of extreme sea level and benefit-cost assessment of adaptation measures along Upper Adriatic Sea costs.....	71
4	Lessons learned and links established.....	76
	References.....	78

## 1 Executive summary

With this report we demonstrate the applicability of the within EUCP developed climate datasets for providing (cross-)sectoral hazard and impact outlooks for case-studies throughout Europe. The aim of the case-studies was the development of future hydro-meteorological risks indicators related to amongst others flash floods, river floods, storm surge, coastal erosion and wind droughts at various spatial scales relevant to end users. We focus on four different types of climate models simulations:

- (i) Decadal projections from WP1;
- (ii) Global Climate Model (GCM) projections and weighting methods (WP2);
- (iii) Regional Climate Model (RCM) simulations from WP3 and EURO-CORDEX;
- (iv) Convection Permitting Regional Climate model (CP-RCM) simulations from WP3.

We evaluate their applicability for the assessment of the following sectoral impacts:

- (i) The impact of multi-decadal droughts in the agricultural sector
- (ii) The impact of wind drought and wind speed changes for the wind power sector;
- (iii) The impact of climate change on flash flood frequency of occurrence and severity in the Alps;
- (iv) The impact of changes in urban pluvial and coastal flooding in Italy
- (v) The impact of climate change on streamflow changes throughout Europe;
- (vi) The impact of sea level rise and storm surge changes on coastal erosion;

An overview of the case-studies is provided in Table 1.1.1. This report presents the technical modelling workflows developed to translate the climate model outputs into sectoral hazard and impact indicators. The end-user perspective will be evaluated in deliverable 4.5. Overall, we were able to derive valuable and state-of-the-art information within the different case-studies using mostly existing modelling and post processing techniques. Some key findings we find include:

- Not all required climate variables are by default reported as output from the climate simulations. Within EUCP there was strong interactions with climate modelers and the case-studies expressed their specific needs. Still, interpolation and machine learning were required to derive wind speed at 100meters (hub height) for assessing impact on energy production;
- The CP-RCM simulations provide hourly precipitation fields at resolutions of 1 – 4 km and the models resolve convective storms which is extremely valuable for future urban and flash flooding assessments. Although process representations have strongly advanced over time, biases in precipitation may remain. When interested in absolute values instead of relative changes there may be a need for bias-correction but high-resolution large scale homogeneous hourly and (even) daily observational datasets required for such correction hardly exist;
- The length of CP-RCM simulations is limited to about one decade due to the high computational costs. In the flash flooding case-study we presented a method to trade space-

for-time using a regional pooling approach and were able to assess changes in flash flood occurrence and severity over the whole European Alpine domain;

- Only a few decadal prediction systems provide sub-daily data for the components of surface wind (i.e., the uas and vas variables), which are necessary to compute the surface wind speed. One possible approach to overcome the limited ensemble size is to use climate indices computed with monthly data (which are provided by all the forecast systems) as predictors. But provision of sub-daily data by the climate modelers would be the preferred solution.
- Not all the decadal forecast systems are available in near-real time, this limits the multi-model ensemble size for a potential operational climate service provision. A larger number of predictions contributing to the multi-model ensemble could increase the skill in predicting variables with a low signal-to-noise ratio such as the precipitation or the surface wind speed.
- There is a difference in climate change projections provided by the individual climate models due to, amongst others, differences in real world process representation and model parameterization. Ensembles of climate models are in the meantime available for all of the above-mentioned types of climate models. They provide a way to address the inter-model uncertainties and to provide future projections with a realistic spread;
- The use of multi-model ensemble datasets was further enhanced by applying weighting techniques developed by WP2 partners, herewith a more robust climate change signal can be obtained.

In deliverable 4.4 we will further discuss the opportunities and draw-backs of the climate model datasets, provided under EUCP and available through other initiatives. Deliverable 4.4 will not only address the application within the EUCP project but also elaborate on future cross-sectoral applications.

Table 1.1.1: Overview of the WP4 case-studies of EUCP.

Case study topic	Lead	Source climate projections	Inter WP-linkages and collaborations
Flash flood projections for the Alps	Deltares	WP3 CP-RCM simulations	Application of WP3 datasets
Projections of future wind droughts	IPSL	EURO-CORDEX	Interaction with wind energy sector in Brittany
Projections of coastal erosion under future storm conditions and Sea Level Rise	Deltares	Jackson and Jevrejeva (2016) – IPCC AR5	Collaboration with end-user JRC and interaction with the Dutch water authority
Multi-year forecast of drought and heat stress conditions over global wheat harvesting region	BSC	Decadal forecasts (forecast years 1 to 5) from WP1. 42 members from 4 GCMs	Collaboration with end-user JRC (science area: Agriculture and food security). The study was further developed under the framework of the Copernicus Climate Change Services (contract number: C3S_34c) that developed a prototype climate service product
Multi-year forecast of surface wind	BSC	Decadal predictions from the Decadal Climate Prediction Project of CMIP6	Application of WP1 datasets in WP4

Coastal and urban flood impacts Italy	CMCC	CP-RCM, Sea Level Rise scenarios	Application of WP3 datasets
Ensemble streamflow projections European rivers	Deltares	EURO-CORDEX	Collaboration with WP4 partners and end-user JRC. Application of weighting methods from WP2
Ensemble streamflow projections Europe – antropoghenic + climate influence	IIASA	EURO-CORDEX + Pseudo-global warming (PGW) experiment KNMI	Collaboration with WP4 partners. PGW simulations from KNMI WP2

## 2 Project objectives

The deliverable has contributed to the following EUCP objectives:

No.	Objective	Yes	No
1	Develop an ensembles climate prediction system based on high-resolution climate models for the European region for the near-term (~1-40 years)	X	
2	Use the climate prediction system to produce consistent, authoritative and actionable climate information	X	
3	Demonstrate the value of this climate prediction system through high impact extreme weather events in the near past and near future	X	
4	Develop, and publish, methodologies, good practice and guidance for producing and using EUCP's authoritative climate predictions for 1-40 year timescales	X	

### 3 Detailed report

This report summarizes the case-studies conducted under EUCP in WP4. The aim of the case-studies was the development of sectoral and cross-sectoral indicators to assess future hydro-meteorological risks (e.g., flash flood, river flood, storm surge, coastal erosion, wind droughts) at various spatial scales relevant to end users. Herewith the case-studies demonstrate the value of the climate prediction system through assessing the impacts of future high extreme weather events. All case-studies aimed at deriving actionable indicators by translating the climate data developed in the other work packages of EUCP (e.g., WP1, WP2 and WP3) for specific applications.

This deliverable mainly focusses on the technical description of the case studies and the assessment of the sectoral climate impacts. The most important stakeholder interactions, for example for the coastal erosion case study, have been included, but Deliverable 4.5 reports on the end-user perspective in more detail. Deliverable 4.4 focuses on the lessons learned and the opportunities and drawbacks of the newly developed climate models and climate datasets. The work for the outermost regions will be reported in a separate deliverable that is due end of March.

Most of the case-studies are finalized, where possible the results have been shared with end-users (see deliverable 4.5). Several scientific papers have been published as indicated in the individual chapters. For a few case-studies, such as the flash flooding in the Alps, the last steps will be completed and published (submitted for peer reviewed international journals) in the final project months. The progress and main results are presented in the remainder of this chapter.

Next to the scientific publications, for most of the case-studies the summary and results are presented in storyboards developed by eScienceCenter: [EUCP Storyboards \(eucp-project.github.io\)](https://eucp-project.github.io)

## 3.1 Assessing future changes in flash flood frequency and occurrence over the European Alps

### 3.1.1 Brief introduction to the case-study

Flash floods are sudden local floods triggered by high-intensity, short duration rainfall. They can cause serious economic damage and lead to mortalities and mainly occur in mountainous terrain, like the Alps. Increases in extreme rainfall have been observed (Förster and Thiele, 2020) and climate change may further influence the severity and occurrence of extreme rainfall events that potentially lead to flash floods.

The recently developed Convection Permitting Regional Climate Models (CP-RCMs) have grid resolutions of 1 to 4 km. This enables the simulation of orographic precipitation as well as the explicit computation of convection. They provide hourly simulations that represent the diurnal cycle of the modelled rainfall (Ban et al., 2021). One drawback is that this increase in spatial resolution comes with a high computational cost and thus runtime, the simulation periods are therefore often limited to about a decade which creates a challenge for extreme value analysis. Building upon existing local and event-based flash flood studies where CP-RCMs are connected to hydrological models to assess future changes in flash flood occurrence and severity (Kay et al., 2015; Schaller et al., 2020) a regional approach was chosen for simulating flash floods in the European Alps. Ten-year transient CP-RCM simulations available from WP3 are used as input for a high-resolution hydrological model. With this regional approach, the hypothesis is that we can trade space for time. Given the relatively short simulation periods of 10 years available but using a large enough spatial domain, we will be able to statistically assess future changes in flash flood frequency and magnitude over the European Alpine.

*A manuscript with a detailed description of this case-study has been submitted for publication:*

Zander, M.J., Viguurs, P.J., Sperna Weiland, F.C. and A.H. Weerts. Future changes in flash flood frequency and magnitude over the European Alps Weather and Climate Extremes (submitted), 2021.

*Planned future publications:*

Zander, M.J., F.C. Sperna Weiland, C. Liguori, A.H. Weerts, 2022. Hydrological evaluation of a high-resolution multi-model convection permitting climate model ensemble over the European Alps. to be submitted to Env. Res. Letters, 2022.

Zander, M.J., F.C. Sperna Weiland, and A.H. Weerts, 2022. High Resolution Multi-model convection permitting climate model ensemble-based assessment of future changes in flood frequency and severity over the European Alps, to be submitted, 2022.

### 3.1.2 Methods

#### **CASE-STUDY AREA**

The case-study focuses on the European Alps and has been sub-divided in the upstream parts of the Rhone, Rhine, Danube, Adige and Po river basins (see Fig. 3.1.1). Most flash floods in the European Alps occur in late summer and autumn. The high Mediterranean Sea surface temperature of late summer can load the atmosphere with substantial amounts of water vapor. The conditionally unstable air masses advect to the coast where they are forced to lift and are channeled due to the orography. This can lead to intense convective rainfall events which cause flash floods (Tarolli et al., 2012).

#### **HYDROLOGICAL MODEL**

The wflow-sbm hydrological model developed at Deltares was schematized for the separate Alpine river basins (Imhoff et al., 2020; Eilander et al., 2021). wflow\_sbm is a distributed hydrological model developed to maximise the use of high-resolution spatial data from Earth observations. An advantage of the model concept is its flexibility in spatial resolution and its performance without calibration. Models can be set up (automated) for river basins around the globe using open data at various spatial resolutions. The model parameters are estimated from point-scale (pedo)transfer functions. For this study the models were set-up at a regular grid resolution of ~1km that allows for detailed streamflow simulations.

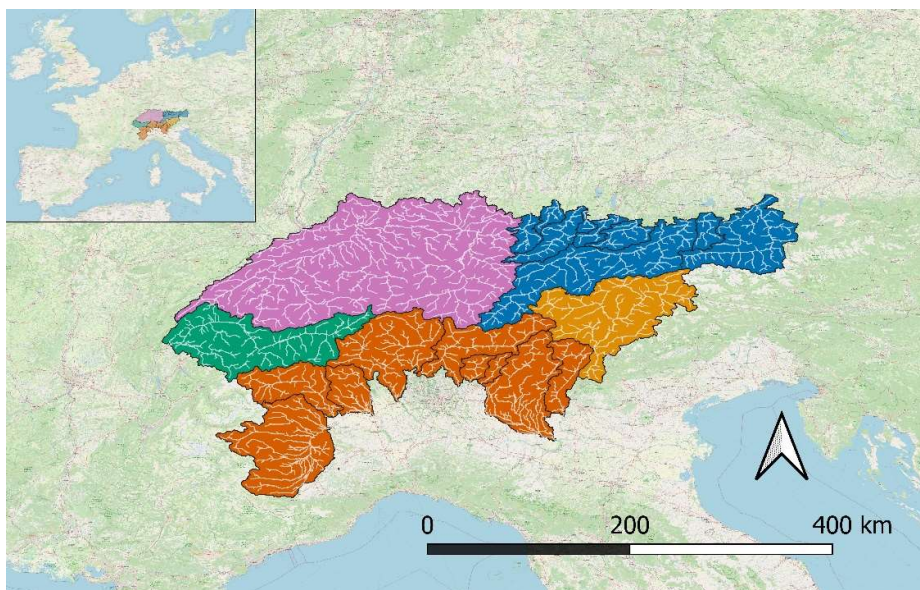


Figure 3.1.1: Hydrological modelling domain over the European Alps with the basins Adige (yellow), Danube (blue), Alpine tributaries to the Po (orange), Rhine (pink) and Rhone (green)

#### **CONVECTION PERMITTING REGIONAL CLIMATE MODEL**

The first part of this study builds upon the Unified Model (UM), MetOffice Hadley Center UKMO 2.2 km (Berthou et al., 2018)<sup>1</sup>. Three UM simulations are used, see Table 3.1.1. The current climate is simulated for the period of 1998-2007 ('Current Climate') and for the climate change scenario the period 2096 - 2105 is simulated with RCP 8.5 ('Future Climate'). The Historical simulation serves to

<sup>1</sup> In the final months of this project the case-study is being extended with a larger ensemble of CP-RCM models to account for model uncertainties, this work is still to be finalized.

assess the quality of the model, while the Current Climate and Future Climate simulations are to assess the differences that could be attributed to climate change. The climate data was converted to the hydrological model grid at an hourly temporal resolution at the JupyterLab environment developed by eScienceCenter as part of the EUCP project to enable big data processing.

Table 3.1.1: Hydrological model simulations

Simulation	Driving Data	Time Period	Source Spatial Resolution	Temporal Resolution
Validation	ERA-5	01/01/1979 - 31/12/2019	0.25°	daily
Historical	ERA-Interim	01/01/2000 - 31/12/2012	2.2km	hourly
Current Climate	GCM	01/01/1998 - 31/12/2007	2.2km	hourly
Future Climate	GCM, RCP 8.5	01/01/2096 - 31/12/2105	2.2km	hourly

### 3.1.3 Results

#### HYDROLOGICAL MODEL PERFORMANCE

As can be seen in figure 3.1.2, that presents the performance (KGE values) for the wflow\_sbm run forced with the ERA5 historical reference dataset, the hydrological model is able to simulate the annual cycle of discharge with low flows in winter and snow melt leading to discharge peaks from May to July. For most stations the KGE ranges from 0.4 to 0.7.

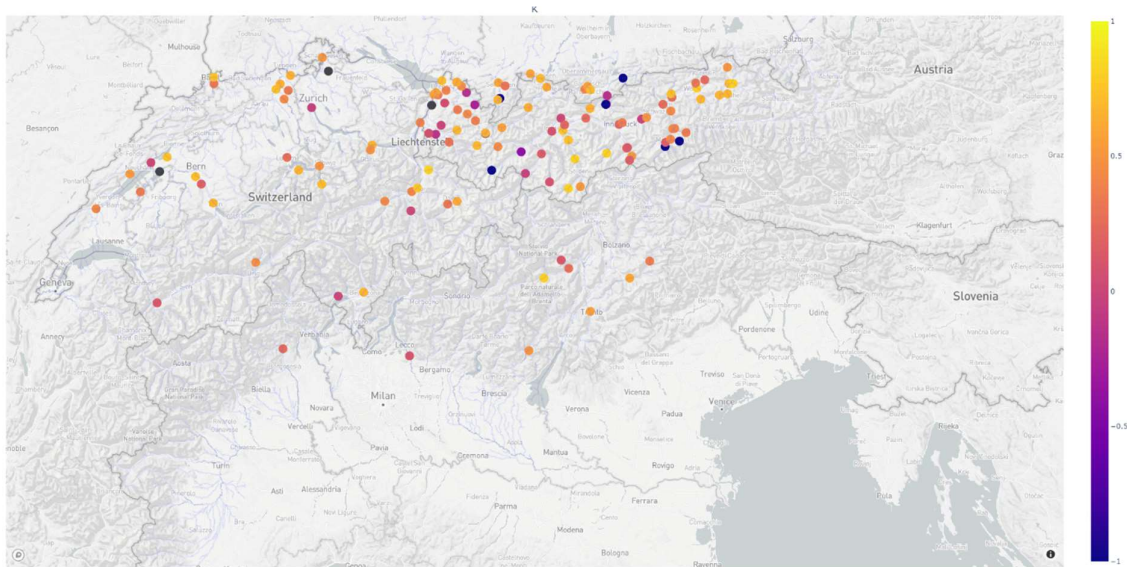


Figure 3.1.2: Map of the Kling-Gupta Efficiency for the 130 stations for daily discharges for 2002-2012 for the ERA5 Validation simulation.

The ERA-5 driven validation simulations generally clearly outperforms the Historical simulation, as can be seen from the higher KGE values in figure 3.1.3. This indicates that the CP-RCM downscaled ERA-Interim precipitation is not as good as the more recently released ERA5 data.

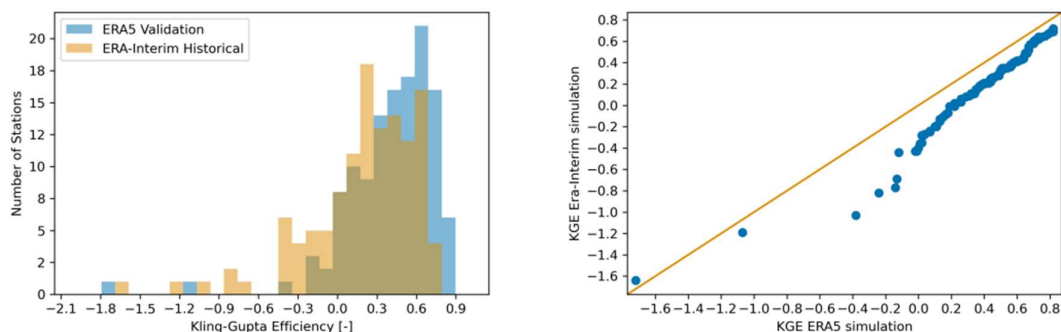


Figure 3.1.3: Performance comparison between observed and modelled daily discharges for 2002-2012 Validation ERA5 and Historical ERA-Interim simulations for the 130 stations using the Kling-Gupta Efficiency.

### FLASH FLOOD VALIDATION

For the validation of flash flood simulation and definition of a threshold for flashflood occurrence this study relies upon two databases of recorded flood events from which the flash floods were selected, the EuroMedeFF (Amponsah et al., 2018) and Hanze (Paprotny et al., 2017) flood databases

Table 3.1.2: Recorded flash floods and simulated peak specific discharges in the Historical ERA-Interim driven simulation

start recorded date	regions & rivers	modelled unit peak discharge	time of unit peak discharge	source
5-6-2002	Sesia (Po)	1.18	5-6-2002	EuroMedeFF
6-6-2002	Rhone	1.22	5-6-2002	Hanze
6-6-2002	Danube. Rhine	2.18	6-6-2002	Hanze
8-9-2002	Rhone	0.48	9-9-2002	Hanze
24-3-2005	Rhine	0.47	24-3-2005	Hanze
3-10-2006	Isarco. Passirio (Adige)	0.49	3-10-2006	EuroMedeFF
8-6-2007	Zuerich (Rhine)	2.39	7-6-2007	Hanze
12-7-2008	Po	1.35	9-7-2008	Hanze
4-8-2012	Vizze (Adige)	0.66	6-8-2012	EuroMedeFF

All recorded flash flood occurrences from the flood databases correspond to high modeled unit peak discharges as can be seen in Table 3.1.2. The modelled peak unit discharge ranged from 0.49 to 2.4  $\text{m}^3\text{s}^{-1}\text{km}^{-2}$ . Based on that information the threshold for modelled flash floods was set to  $0.5 \text{ m}^3\text{s}^{-1}\text{km}^{-2}$ .

### FUTURE FLASH FLOODS

Figure 3.1.4 shows the number of days on which the flash flood threshold for peak specific discharge was reached or exceeded for the Future and Current Climate simulations for summer and autumn. The summers have more threshold exceedances than autumns in both Current Climate and Future Climate simulations. In summer there are more days with threshold exceedances for the Current Climate scenario than for the Future climate while in autumn we see hardly any difference between the number of days with threshold exceedances in the Future Climate scenario. The decrease in flash flood occurrence can be a result of decreases in mean precipitation and increases in evaporation that lead to drier soil moisture conditions offering more storage during extreme events (Gaume et al., 2009). In addition, in line with these results the CP-RCM also indicates a decrease in the occurrence of heavy precipitation events, but an increase in the heavy precipitation amount (the p99.9 value).

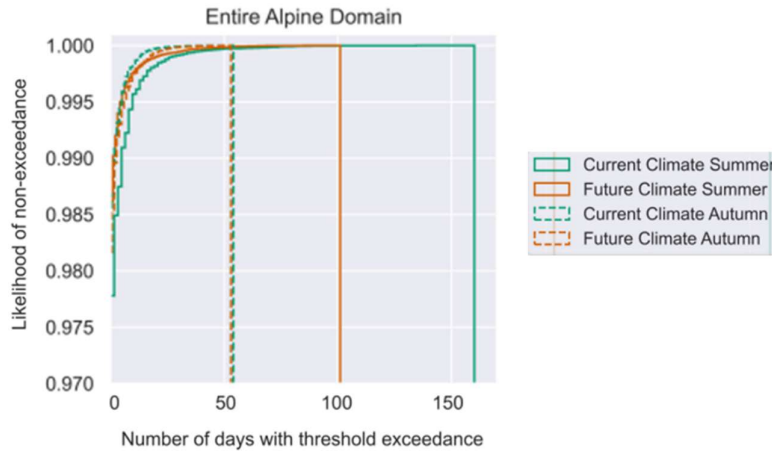


Figure 3.1.4: Cumulative distribution of the number of days on which the flash flood threshold is reached in summer (JJA, solid lines) and autumn (SON, dashed lines) for the Current Climate (green) and Future Climate simulation (orange).

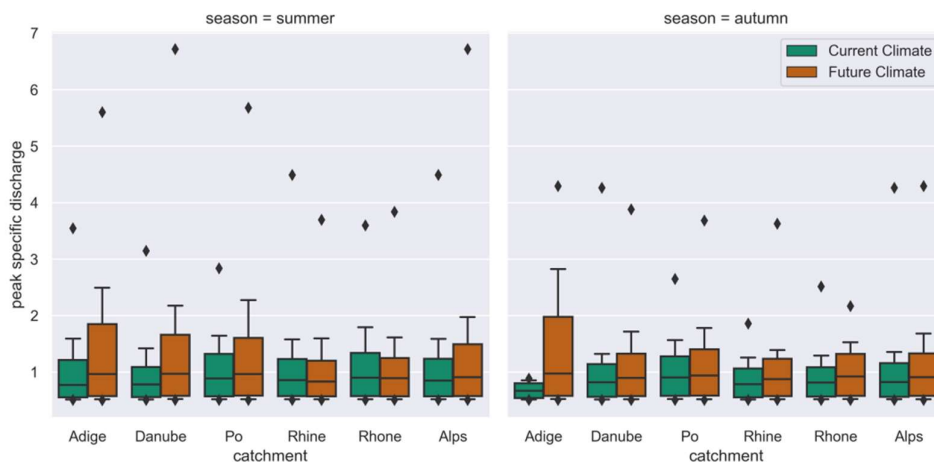


Figure 3.1.5: Boxplots for maximal daily specific discharge exceeding the  $0.5 \text{ m}^3\text{s}^{-1}\text{km}^{-2}$  specific threshold for summer (JJA) and autumn (SON) for the Current Climate and Future Climate simulation. The boxplots show the 25th, 50th & 75th percentile, with whiskers for the 2.5th & 95th percentile and diamonds for the maximal value.

Figure 3.1.5 shows box-and-whisker plots of the magnitude of the daily maximal peak specific discharges for each of the threshold exceedances. Over the entire Alpine domain, both the Future Climate summer and autumn have a higher 75 and 97.5th percentile of threshold exceedances. This indicates increases in the more extreme flash floods. The median magnitude remains more or less the same. The difference between current and future climate is largest for the Adige river. Here the median size flash floods are indicated to increase and the increases in the more extreme flash floods are larger than for the other basins.

### 3.1.4 Lessons learned and conclusions

The available time-series from CP-RCMs are limited to 10 years. With such time slices it is possible to move beyond event-based climate impact studies (Felder et al., 2018), but derivation of local statistics of change is hampered. Similar to Alfieri et al. (2015) and Rudd et al. (2020) this study presented a regional approach, aggregating results over larger regions. Yet one cannot estimate return periods of extreme events as the simulation periods are too short to warrant such an approach.

The CP-RCM may be biased both for the GCM driven and ERA-interim driven simulations. It was explicitly chosen not to apply a bias correction, downscaling or a delta change approach to the climate model data as these techniques can disturb the change signal. Additionally, no homogeneous datasets exist for bias correction for the entire modelled Alpine domain at the resolution and time-step of the CP-RCM data. Because we directly compare the two GCM driven climate simulations and thus focus on relative changes, the influence of biases for quantifying changes in flash flood frequency and magnitude is limited.

Similar to the work of Rudd et al. (2020), this study shows added benefit of using the combination of convection-permitting climate model and hydrological modelling. Changes in precipitation do not translate one-on-one into changes in flash floods. The hydrological model is required to estimate frequency of occurrence and magnitude of the specific peak discharge that represents flash floods.

Up till now these kind of regional analysis have been based on RCM data, to evaluate the added value of CP-RCM simulations it would be good to compare the results of the flash flood analysis for an ensemble of modelling chains set-up with CP-RCM data and RCM data as input.

Assuming a relation between the flood peak and the flood impacts, we speculate that although overall the number of flash floods will decrease, they will become more devastating.

Finally, the construction of climate models always involves simplified presentation of real-world processes and need for parameterizations. To account for these uncertainties the here presented work is being extended with an assessment based on a multi-model ensemble of CP-RCMs as became available during the project (WP3). This will also include a hydrological evaluation of the different CPM models

## 3.2 Long term variation and projection of hub-height wind speed in Europe during twenty-first century

### 3.2.1 Brief introduction to the case

This case-study focuses on the multiannual and multidecadal decreasing trend in surface winds, known as “wind stilling” or potential surface wind declines (Vautard et al., 2010). Based on 822 surface weather stations, Vautard (2010) found that the surface wind speeds have declined by 5-15% over most continental areas in the northern mid-latitudes. The decline of wind speed in many regions of the world is expected to decrease wind power production (Tian et al., 2019), as wind speed is the most effective factor for comprehensive wind resource assessment (Jang and Byon, 2020). Compared with surface wind data, which is abundantly available in datasets, 100m wind speed (w100) data are more relevant for an accurate assessment of wind energy resources, as the hub height ( $h_{\text{hub}}$ ) of large wind turbines is about 100m (Rehman and Al-Abbadi, 2007). However, w100 data is limited in observations and climate models report output at specific pressure levels instead of absolute elevation, which brings challenges to the assessment of wind energy resources. In general, the 100 meters wind speed is estimated from the surface wind speed by an empirical relation (often a calibrated multiplicative factor) which turns out in many cases to be too approximative to be useful. In particular, in many places, and in stable weather conditions (nighttime, wintertime under anticyclonic conditions), the 100m wind speed is disconnected from the surface. For instance, the diurnal cycle of the wind speed is relatively “flat” at 100m while at surface it is pronounced with a peak in the daytime.

To fix this, the present study focused on developing a machine learning method to establish a transfer model for constructing the hourly grided w100 dataset in European region. The model, developed in this study, can be applied to calculate w100 output of global climate models flexibly and efficiently. It can thus be used in the assessment and estimation of long-term 100m wind speed in European region from past to the future. We hope to obtain more accurate estimation of long-term wind-power changes.

### 3.2.2 Methods

#### **TRADITIONAL METHOD (BASELINE)**

Most previous studies extrapolate the ground wind speed to hub-height wind speed based on a simple equation as follows:

$$x_{\text{hub}} = x_g \left( \frac{h_{\text{hub}}}{h_g} \right)^E \quad (1)$$

where  $x_g$  is the wind speed near the ground,  $h_g$  the height where  $x_g$  was measured and  $E$  is the power law exponent most often considered to be 0.143 (Olaofe, 2016). The results of the traditional method will be used as reference in the evaluation of the here developed machine learning model.

#### **RANDOM FOREST**

The Random Forest (RF) method was used to establish the transfer model in this study. The RF method is based on CART DT (Breiman, 2001) and produces numerous independent trees to reach a final decision through random bagging resampling (Prasad et al., 2006) to the selection of a random subset of training samples and a random subset of candidate variables at each node of a tree. Due to the randomization, RF has the robustness to counteract the noise, outliers and overfitting potentially suffered by a DT model (Rhee et al., 2014). RF provided mean decrease accuracy or mean decrease Gini index in classification when a variable is permuted. The greater this decrease in accuracy, the more important the variable.

**WIND SPEED MODEL CONSTRUCTION USING MACHINE LEARNING METHODS**

In the present research, machine learning methods were used to construct the 3-hourly 100m wind speed based on the ERA5 dataset. The methodology of this study is presented in Fig. 3.2.1.

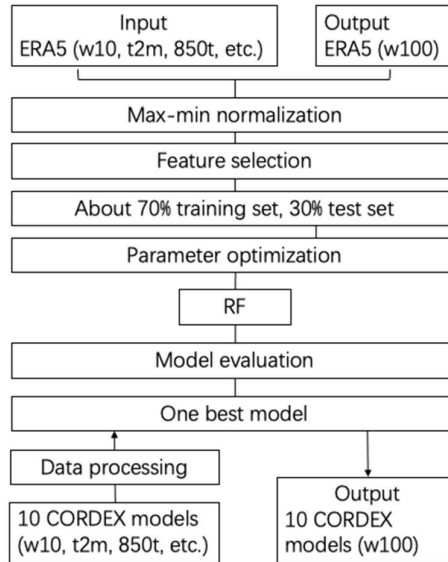


Fig. 3.2.1 Workflow of the machine learning model-based w100 construction algorithm.

For establishing the input feature set, we selected meteorology features, including t2m, t850, roughness, t850-t2m (temp\_diff), w10(t) and the w10 value at its eight neighbor moments, including w10(t-4), w10(t-3), w10(t-2), w10(t+1), w10(t+1), w10(t+2), w10(t+3) and w10(t+4); geographical location, including longitude, latitude, land-ocean (land=2 and ocean=1); time feature: hour (0 UTC = 0, 3 UTC = 1, 6 UTC = 2, 9 UTC = 3, 12 UTC = 4, 15 UTC = 5, 18 UTC = 6, 21 UCT = 7). This choice accounts for atmospheric stability with simple, easily available parameters (temp\_diff), and for the hourly wind evolution. The output label is 3-hourly w100 of ERA5 dataset. Maximum and minimum normalization is used to scale the input and output to between 0 and 1. Lasso method was used in feature selection (Fonti and Belitser, 2017).

We selected 400.000 samples from 1979-2005 in the research area. The sampling process was random and covered all the research periods and areas. We set 20% samples as the test set, 20% samples as the validation set and the other samples as the train set. Several popular statistical indices, including Mean Absolute Error (MAE), Root mean squared error (RMSE) and Mean squared error (MSE), were used to quantitatively evaluate the performance of the machine learning models.

We applied the ML transfer model for 10 Euro-CORDEX climate simulations to obtain the 100m wind speed output of each model. Before applying the model variables to the best algorithm, we pre-processed the model output variables so that the variables can be applied to the trained algorithm. Firstly, we interpolated the model data on a 0.25°grid based on a bilinear interpolation method to make its spatial resolution consistent with that of the ERA5. Then, the bias of each variables between ERA5 and models were removed following Miao (2016). Finally, the changes of hub-height wind speed in Europe from past to future could be explored in this research.

### 3.2.3 Results

#### FEATURE SELECTION

The goal of feature selection is to underline which explanatory variables are more relevant to predict the response variable. Fig. 3.2.2 illustrates that the variable that has the highest influence on the w100 in a selected time t is w10(t). It shows steadily positive impact. Another important variable is the land-ocean difference, which also positively affects the w100; as we can see clearly the temp\_diff negatively affects the w100.

Furthermore, other important variables, such as w10(t-1), roughness, latitude and longitude, 850t, w10(t+3), w10(t+1), time, w10(t+2), w10(t+4) and w10(t-4), can also be selected to establish the RF model in the next step.

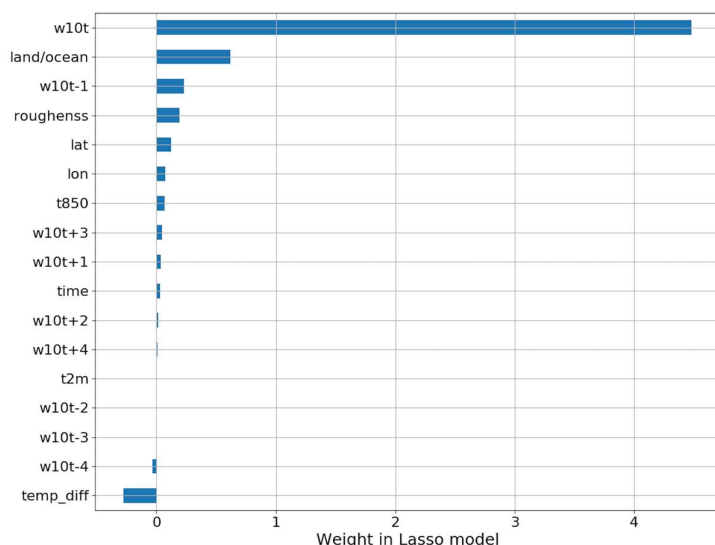


Fig.3.2.2 The regression coefficients in Lasso, which show the weights corresponding to different variables.

#### MODEL EVALUATION

We compared the performance of machine learning and the traditional algorithm in reflecting the temporal changes of w100 during 1979-2005 (Fig.3.2.3a). For traditional algorithm, the MSE and RMSE in the test set were 2.133 and 1.461, respectively. The machine learning methods produced much higher accuracy than traditional model. The RMSE was 0.572, showing a clear improvement.

For diurnal cycle of w100 in the whole region (Fig.3.2.3c), the results simulated by RF were consistent with the real nature, which was higher during the day and lower at night. The reason is that the high-altitude wind speed is less affected by ground factors, such as trees and buildings. During the night, the surface temperature is lower than the air temperature in high altitude. The atmospheric stratification is more stable, which leads to higher wind speed in high altitude. However, for traditional algorithm, it was difficult to reflect the nonlinear change of wind speed from low altitude to high altitude. The result of the traditional model showed that the w100 was lower during the day and higher during the night, which was not consistent with the real nature. For seasonal cycle (Fig.3.2.3d), traditional algorithms overestimated the seasonal variation of w100, especially in the winter. The machine learning algorithms can well reflect the seasonal changes of wind speed with higher accuracy. For the spatial evaluation of the algorithms (Fig.3.2.3b), RF showed good performance in each grid with the RMSE value <1. However, the accuracy of the algorithms was declined near the coastline, suggesting that the variables with land and ocean difference information need to be added into the model establishment.

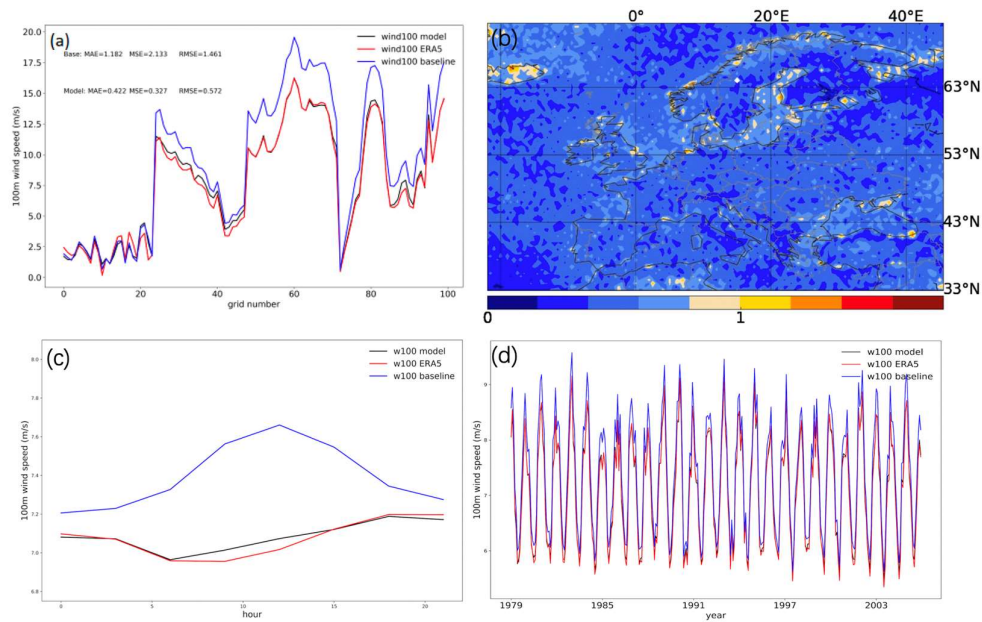


Fig.3.2.3 (a) The  $w_{100}$  obtained by ERA5 and the RF simulations point by point. Only the results from the first 100 samples were shown in this figure. (b) The RMSE of  $w_{100}$  in each grid of the region based on ERA5 and RF. The (c) diurnal cycle and (d) seasonal cycle of  $w_{100}$  based on ERA5 and RF simulations during 1979–2005.

In summary, compared with the traditional algorithm, the machine learning-based algorithm is powerful in constructing the gridded 100m wind speed. RF has good performance on the hourly scale, which corrects the poor performance of the diurnal cycle characteristic using the traditional algorithm.

### MODEL APPLICATION

The RF model was applied to the output of the 10 high-resolution climate models to obtain the  $w_{100}$  outputs in each model. Thus, the future changes of hub-height wind speed in Europe can now be explored. We applied the RF algorithms to the 10 climate models and investigated the characteristics of  $w_{100}$  under RCP8.5 emissions. The results showed that in the whole of Europe, the  $w_{100}$  showed significant decreasing trend in the past fifty years (rate= $-0.019 \text{ m}\cdot\text{s}^{-1}\cdot\text{decade}^{-1}$ ,  $p<0.01$ ). The decreasing trend will be slightly enhanced in the next 100 years (Fig. 3.2.4), which is projected to reduce of wind energy resources in Europe. However, the trends are much lower than the observed trends during the past period 1980–2010, of the order of  $0.1 \text{ m}\cdot\text{s}^{-1}\cdot\text{decade}^{-1}$ . This trend was largely attributed to changes in land use/land cover and the induced change in surface roughness. However, a recent recovery was also found in the last decade (Zeng et al., 2019), which indicates that part of the observed trend at least is due to natural variability.

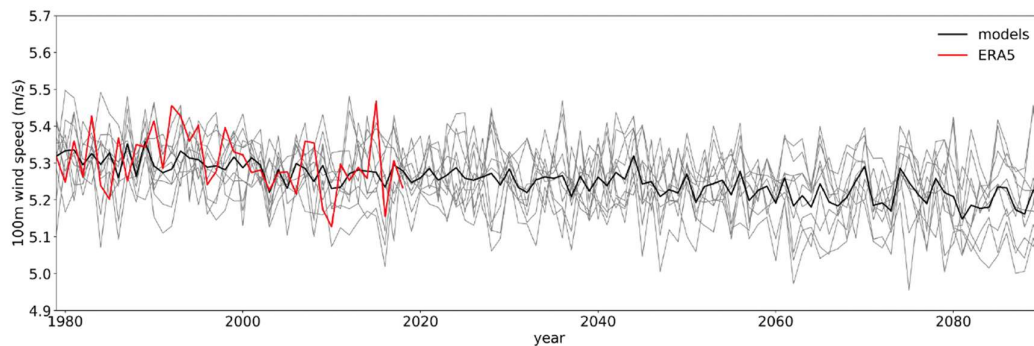


Fig.3.2.4 Regional mean series of  $w_{100}$  for the 10 climate model outputs (gray lines) for the period 1979–2090. The black line showed the ensemble mean result for the 10 climate model outputs.

### 3.2.4 Lessons learned

In this study, a transfer method to construct a hub-height wind speed gridded dataset based on machine learning was developed. The presented results demonstrated that machine learning algorithms are versatile tools for estimating the wind speed in 100m high, which is meaningful to estimate the hourly gridded wind resource in Europe. In this research, the RF algorithm was applied in 10 climate models. The result shows that the 100m wind speed decreased significantly in most of Europe during the period 1979-2019. The decreasing rate might be enhanced in the future, which indicates an adverse effect for the development of wind power generation in Europe. While this decrease is not critical for wind energy development, local reductions can be larger and may be critical for some projects. It is therefore important that new wind power projects and their funding account for these changes.

## 3.3 Attribution of winter wind energy drought in Europe

### 3.3.1 Brief introduction to the case

Decline of wind speed in many regions of the world is expected to negatively impact wind power production. While the general climate-change driven decrease of wind speed remains limited on average to a few tenths of meters per second, wind power generation and power supply can also be perturbed by episodic periods of “wind droughts” when most of Europe lacks wind, especially during cold winter days when demand is high.

This problem was pinpointed by a local wind energy producer in Brittany, but also several others. In the Brittany case, a succession of low-wind seasons was recently observed, with wind speed values lower than those observed during the test period for the wind farm, leading to this question. Past and future changes in wind energy drought as well as their underlying drivers remain poorly understood. As the occurrence of wind drought events receives increasing attention, two questions should be discussed in this study. Will the decrease in wind energy resources continue in the future? How much of the current “wind energy drought” is caused by human activities?

It is helpful to consider the attribution technique to explore the above questions. Attribution of extreme climate events is an emerging scientific area (Stott et al., 2016) to explore extremes with specific magnitude, time scale and spatial scale. It could be used to examine whether human influence could impact wind energy drought at different time scales. Thus, the aim of this case study is to examine whether human influence on climate could have affected the wind energy drought events in Europe and analyse the different risks under 1.5, 2, 3 and 4 °C global warming scenarios. Such a question was raised in a recent attribution study of the December 2016 low-wind month (Vautard et al., 2017) and it was suggested that monthly wind droughts were increasing with climate change. However, this trend was not studied in a more systematic manner and over other regions than North-Western Europe.

### 3.3.2 Data and Methods

#### **DATA**

The area selected for this study comprises most of the land in Europe, bounded by -22°W, 33°S and 45.5°W, 72.5°N. Only land data were considered in this research. The gridded dataset was taken from the ERA5 dataset for the period from 1979 to 2018 with a spatial resolution of 0.25°×0.25° (Hersbach et al., 2020). It was used in this study to estimate the observed trends in hub-height wind speed (Jourdier, 2020). In this study, we used 10 high-resolution climate projections from the EURO-CORDEX (Coordinated Regional Climate Downscaling Experiment) ensemble (Jacob et al., 2014), with 4 Global climate Models downscaled by 4 Regional Climate Models. For these 10 models, the 100m wind speed outputs were calculated following the Machine Learning method in the previous chapter. For these ensembles, natural forcing simulations were not available, but anthropogenic forcing was assumed dominant in explaining the differences between two climate periods during 1971-2000 and 2000-2029. We compared the extreme distribution from three time periods (1971-2000, previous; 2000-2029, current; and 2041-2070, future) to analyze the effect of anthropogenic climate change on low wind energy generation episodes. The all forcing projections (2006-2100) under Representative Concentration Pathways (RCPs), RCP8.5 were used (a high-emission scenario).

### EVENT DEFINITIONS

Load Factors were used to measure the wind energy in this study. Fig. 3.3.1 shows the power curve that was used in this study. For onshore and offshore wind turbine power curve, the cut-in wind speed is 3 m/s, the peak wind is 10 m/s and 12.5m/s, respectively and the cut-off wind speed is 22.5 m/s and 25.5 m/s, respectively (Jamil et al., 2019).

The classical method defined an extreme event as an exceedance of a threshold in the tail of the distribution of an event indicator. The indicator used here to describe wind energy stagnation was the minimum monthly mean Load Factor in each winter (December-February). We referred it as minimum Load Factor (MLF) in this research. For each day, the maximum daily Load Factor was calculated firstly from hourly data; then, for each winter, the MLF was calculated as the minimum regional mean value during the winter in the whole region. Once the indicator is defined, a threshold was calculated as the return value of MLF corresponding to the 10-year return period in the current climate (2000-2029). The probability of MLF lower than the threshold could be calculated in the three different periods. For a more quantitative result, the risk ratio was calculated to indicate the different probabilities of the wind energy drought between two climate periods. When the risk ratio <1, the low wind energy winter is more frequent in the earlier climate period.

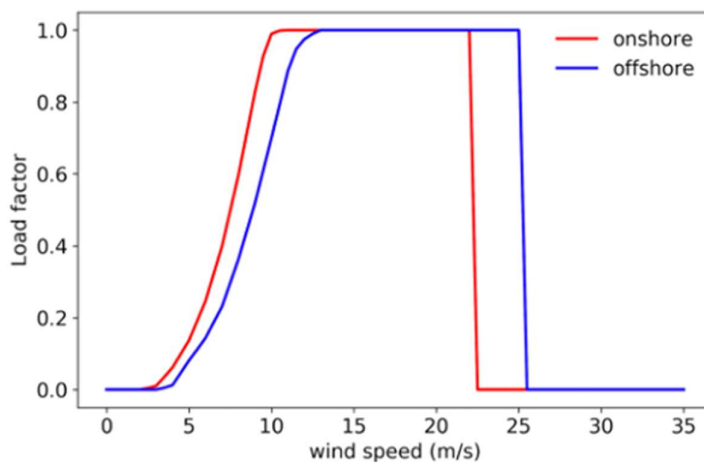


Fig.3.3.1 Load Factor functions based on 100m wind speed used here, including offshore and onshore wind turbines.

### STATISTICAL METHODS

The attribution of the extreme event consists of comparing probabilities of the MLF exceeds the threshold in different climate periods. For model ensemble, a nonparametric approach was used by pooling all MLF of each ensemble member into a single pool and computing the probability by counting the number of exceedances of the threshold. Bootstrapping (Efron and Tibshirani, 1994) was used to obtain confidence intervals by randomly sampling 1000 times. The 95% confidence intervals are calculated by taking the 5th and the 95th return periods of the bootstrap sample (Vautard et al., 2017), with the median value serving as the best estimate. When a value was selected in the bootstrap, the entire model series would be selected. The risk ratios were calculated in the same method. The current climate (2000-2029) was used as the reference period, and the risk ratios were calculated relative to this period. When the confidence interval of this ratio does not include 1, one concludes that the probability is significantly changing due to climate change.

### 3.3.3 Results

#### MODEL EVALUATION

The linear trend in the regional winter Load Factor for ERA5 (Fig.3.3.2) is  $-0.004$  decade<sup>-1</sup> during 1979-2018, which is not statistically significant ( $p>0.05$ ). All winter months are considered. The Load Factor changes based on model ensemble mean has similar characters when compared to ERA5, with a correlation of 0.26. We also compared the distribution of the Load Factor based on ERA5 and each model simulation. The quantile-quantile plots of the distributions of the Load Factor showed the model simulation slightly underestimates the larger Load Factor values (upper tail of the distribution), while it matches well with the ERA5 for the low Load Factor values (lower tail of the distribution). These comparisons suggest that the model simulations gave a good description of the Load Factor distribution in Europe during the current period.

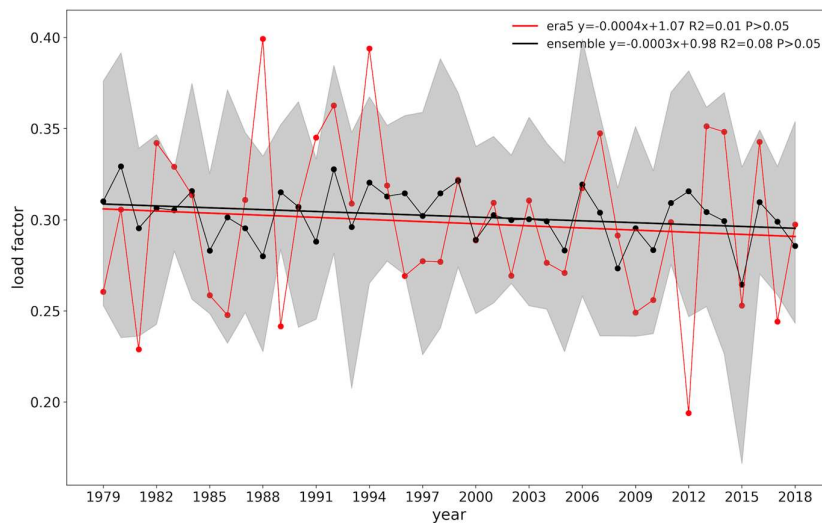


Fig.3.3.2 Changes of mean Load Factor for each winter in the whole Europe during 1979-2019, based on observation, ERA5 (red curve) and ensemble mean of the models (black curve). Grey area: same calculation but shows 5%-95% range of 10 climate models.

#### ATTRIBUTION IN THE WHOLE EUROPE AND A CASE STUDY IN FRANCE

To estimate the probability ratio in different climate periods, we restricted the average over the research region and defined a load factor threshold (0.242) - the return value of MLF corresponding to the 10-years events in the current climate (details in section 2.2). Then, the probability was calculated as the MLF lower than the threshold under different climate periods. The return period of this low wind energy event is about 10.3 years, which suggests the MLF lower than threshold become more than 1.03 times as probable in the current climate than in the 1971-2000 climate, which is not a statistically significant change. The low wind energy winter has become more frequent in recent years and the increase will continue in the future. During 2041-2070, the return period becomes 6.6 years, and the probability ratio is about 1.5 [1.2, 1.8] (i.e. 50% more probable), which remains significant when taking all ensemble members together. Therefore, in the whole of Europe, the probability of low wind energy winter is marginally significantly different between past and current periods. In addition, a case study was investigated on most of France, bounded by  $-4.8^{\circ}\text{W}$ ,  $42.3^{\circ}\text{S}$  and  $8.3^{\circ}\text{W}$ ,  $51.1^{\circ}\text{N}$  (Fig.3.3.3) and the results show that the MLF threshold for 10 years event is lower, but wind energy drought events do not significantly occur more frequently from the past to the future. The attribution analysis can also be applied to specific wind farms to assess the impact of wind drought events on wind energy companies.

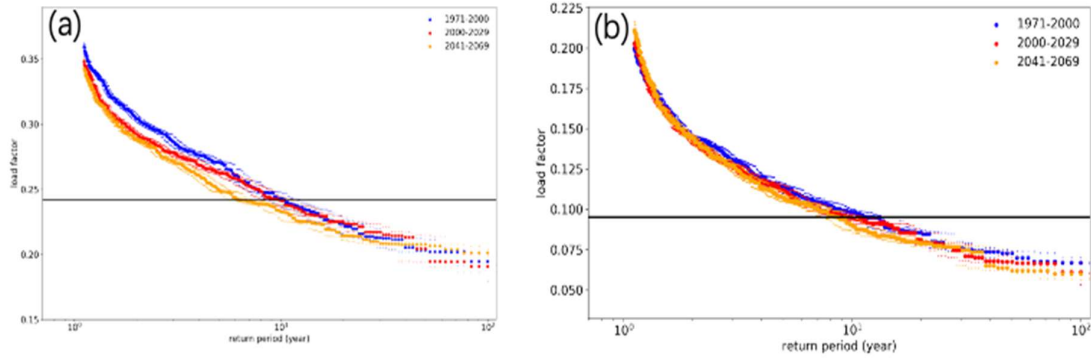


Fig.3.3.3 Changes in return values and return periods for model ensemble in (a) the whole Europe and (b) France. Dots represent median of consecutive sorted return period/values model values from 10000 bootstrap estimations, together with 5%-95% confidence intervals (dashed lines). The black horizontal line shows the return value corresponding to the 10-years return period during 2000 to 2029.

#### THE WIND ENERGY DROUGHT UNDER THE RCPs SCENARIOS

Global warming (Easterling et al., 2000; Sheffield and Wood, 2008) substantially increases the probability that multiple extremes such as heat waves and droughts. Thus, in this research, we explored the probability of a MLF below threshold under different global warming level of 1.5, 2, 3, 4 °C. Firstly, to determine the time periods when given global warming thresholds, we followed the methodology as described by Vautard et al. (2014). The reference period was 1971-2000 and the running window was selected as 31 years. Only RCP8.5 was used to project wind energy in the future.

Fig.3.3.4 shows that in the 1.5 °C warming world, the 10-year return period events occurred more frequently, the ratio value becomes 1.14 [0.98, 1.28], as the return period is about 8.8 years. In the 2°C and 3 °C warming world, the return years become 7.2 and 6.7 years, respectively. When global temperatures are increased by 4 °C, the probability of occurrence of the 10-years events increase to 20%, the risk ratio becomes 1.59 [1.47,1.92] and the return period is about 6.3 years. It means that the changes of low wind energy in Europe are particularly vulnerable to climate change, experiencing adverse effects of global warming in the whole of Europe. With global warming, low wind energy winters in Europe occur more frequently.

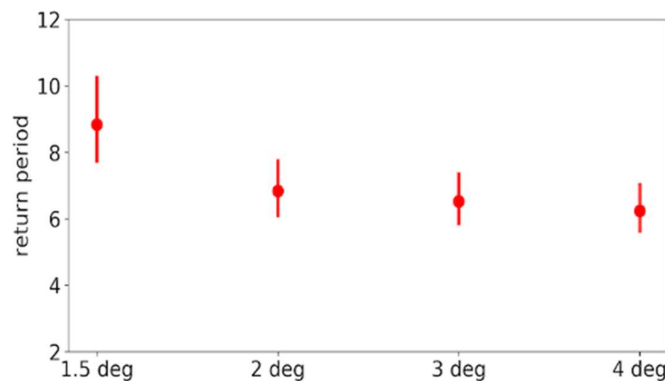


Fig.3.3.4 Return periods for model ensemble under 1.5, 2, 3 and 4 °C global warming scenarios. For boxplot, the red dot shows the median of all the grids in this region; the vertical bar shows the small uncertainty interval of the median. The 5% and 95% of the medians show the uncertainty interval.

### 3.3.4 Lessons learned

Low wind energy winters in Europe are expected to become more common in a warming world. In the whole of Europe, the return period of 10.3-years events in the past has been shortened to about 10 years at present and it would be shortened to about 6.6 years during 2041-2070 under RCP 8.5 scenarios. With global warming at 1.5, 2, 3, 4 °C level the 10-years events at present become more frequent, 8.2, 7.8, 6.7, 6.3 years respectively. That global warming could lead to a remarkable increase (about 20%) in the probability of wind drought winter until the middle of the century. These findings provide new insights into wind energy drought risk assessment and management for producers and grid managers.

## 3.4 Sandy beach erosion induced by sea level rise

### 3.4.1 Brief introduction to the case

Sea level rise (SLR) will cause shoreline retreat of sandy coasts in the absence of sand supply mechanisms (Nicholls and Cazenave, 2010). Almost 41% of the European population lives in coastal regions (Collet and Engelbert, 2013), while a substantial portion of the coastline is sandy (Luijendijk et al., 2018). Coastal erosion can diminish the touristic and recreational value of beaches and cause direct impacts to infrastructure and assets. Additionally, since sandy beaches act as the first buffer against storms, shoreline retreat can increase the vulnerability of the hinterland to coastal flooding. To this end, large scale assessments of shoreline retreat can aid in identifying hotspots and guide adaptation strategies (Figure 3.4.1). Here, shoreline retreat due to SLR at the European scale was assessed using probabilistic SLR projections from Jackson and Jevrejeva (2016), which were produced based on CMIP5 model members. Moreover, a new global spatially varying nearshore slope (SVNS) dataset was produced and a satellite derived sandy beach (SDSB) location dataset was used to identify the erodible part of the coastline. To quantify the effects of these input geophysical data, additional representations of sandy beach location and their nearshore slope were used to create different combinations. An uncertainty analysis was performed to compare the sources of uncertainties in the final land loss projections through the 21<sup>st</sup> century.

This case study was conducted in collaboration with the end-user Joint Research Centre (JRC) and it has been published and described in more detail in:

Athanasiou, P., van Dongeren, A., Giardino, A., Vousdoukas, M.I., Ranasinghe, R., Kwadijk, J., (2020). *Uncertainties in projections of sandy beach erosion due to sea level rise: an analysis at the European scale*, *Nature Scientific Reports*, 10, 11895. <https://doi.org/10.1038/s41598-020-68576-0>

Athanasiou, P., van Dongeren, A., Giardino, A., Vousdoukas, M., Gaytan-Aguilar, S., Ranasinghe, R., (2019). *Global distribution of nearshore slopes with implications for coastal retreat*. *Earth System Science Data*, 11, 1515–1529. <https://doi.org/10.5194/essd-11-1515-2019>

- The developed dataset has been used by JRC to extend the analysis to the global scale:

Vousdoukas, M.I., Ranasinghe, R., Mentaschi, L. et al. *Sandy coastlines under threat of erosion*. *Nat. Clim. Chang.* 10, 260–263 (2020). <https://doi.org/10.1038/s41558-020-0697-0>

Almar, R., Ranasinghe, R., Bergsma, E.W.J., Diaz, H., Melet, A., Papa, F., Vousdoukas, M., Athanasiou, P., Dada, O., Almeida, L.P., Kestenare, E., 2021. *A global analysis of extreme coastal water levels with implications for potential coastal overtopping*. *Nat. Commun.* 12, 1–9. <https://doi.org/10.1038/s41467-021-24008-9>

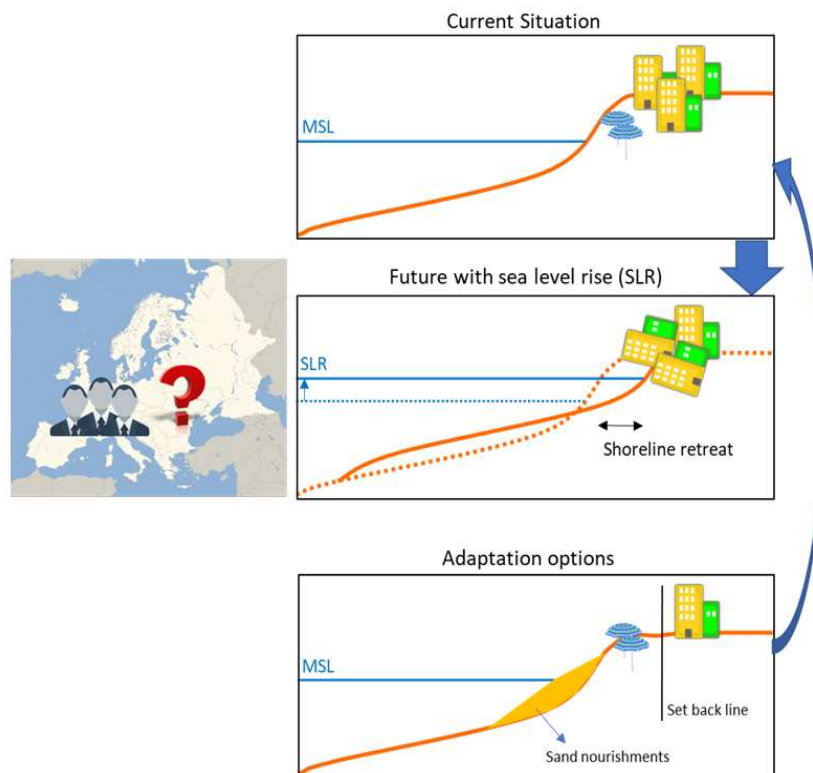


Figure 3.4.1: Schematic representation of the shoreline retreat impacts at sandy coastlines and adaptation strategies to be followed.

### 3.4.2 Methods

#### **SHORELINE RETREAT**

The Bruun rule (Bruun, 1962) was used to quantify the direct erosion of sandy beaches due to SLR. This approach is based on a simple two-dimensional mass conservation rule assuming that an equilibrium profile will be preserved in the future when SLR occurs. The Bruun Rule is expressed as:

$$R = \frac{SLR}{\tan(\beta)}$$

where R is the horizontal shoreline retreat, SLR is the sea level rise, and  $\tan(\beta)$  is the nearshore slope. It was assumed that if SLR is negative there will be no shoreline retreat. The European coastline was discretized with an alongshore spacing of 1 km using the Open Street Maps dataset of 2016 (OpenStreetMap contributors, 2015). Shoreline retreat was assessed at this 1 km grid and then aggregated to land loss at the regional, country, and European levels (Figure 3.4.3). The projections coverage included the coastal EU counties except Croatia, and Romania, Bulgaria and Cyprus which are partially covered by the used datasets. Since no information is available on the landward extents of sandy beach, all shoreline retreat and land loss projection presented herein are potential ones. Moreover, the projection presented here accounts only for the effects of SLR in the absence of any other ambient shoreline changes related to changes in sediment budget.

#### **SEA LEVEL RISE PROJECTIONS**

Sea level rise projections around Europe up to the end of the twenty-first century were obtained from the global probabilistic, process-based study of Jackson and Jevrejeva (2016). The SLR projections are available from 2010 to 2100, every 10 years, capturing the 5<sup>th</sup>, 17<sup>th</sup>, 50<sup>th</sup>, 83<sup>th</sup>, 95<sup>th</sup> and 99<sup>th</sup> percentiles of potential SLR under RCP 4.5 and a high-end RCP 8.5. The high-end RCP 8.5 scenario is based on IPCC AR5 (Church et al., 2013) but uses Antarctic and Greenland ice sheet contributions from Bamber and Aspinall (2013), resulting in higher median global SLR (i.e., 84 cm versus 74 cm of AR5) and larger and more asymmetric uncertainties (Vousdoukas et al., 2018). The high-end RCP 8.5 scenario will be referred simply as RCP 8.5 for the rest of the chapter. These projections were of regional SLR, thus taking into account the regional footprint of SLR, due to various contributions. On the other hand, local tectonics and subsidence are not included in the projections.

### **GEOPHYSICAL DATA**

Shoreline retreat as computed using the Bruun rule is linearly dependent on the local nearshore slope. For this case study a global dataset of nearshore slopes was produced at a 1 km alongshore resolution (called SVNS dataset herein, Figure 3.4.2), using global topo-bathymetric data (Athanasidou et al., 2019).

The spatial distribution of sandy beaches is a critical input for assessing shoreline retreat at large spatial scales. Here the Satellite Derived Sandy Beaches (SDSB) location dataset (Luijendijk et al., 2018) was used to represent the location of sandy beaches in Europe. This dataset has global coverage and was created using machine learning techniques on satellite images from the Sentinel-2 mission. Additionally, the geomorphological map of the European coasts available from the EUROSION project was used as an alternative to represent the sandy beach distribution along the European coastline.

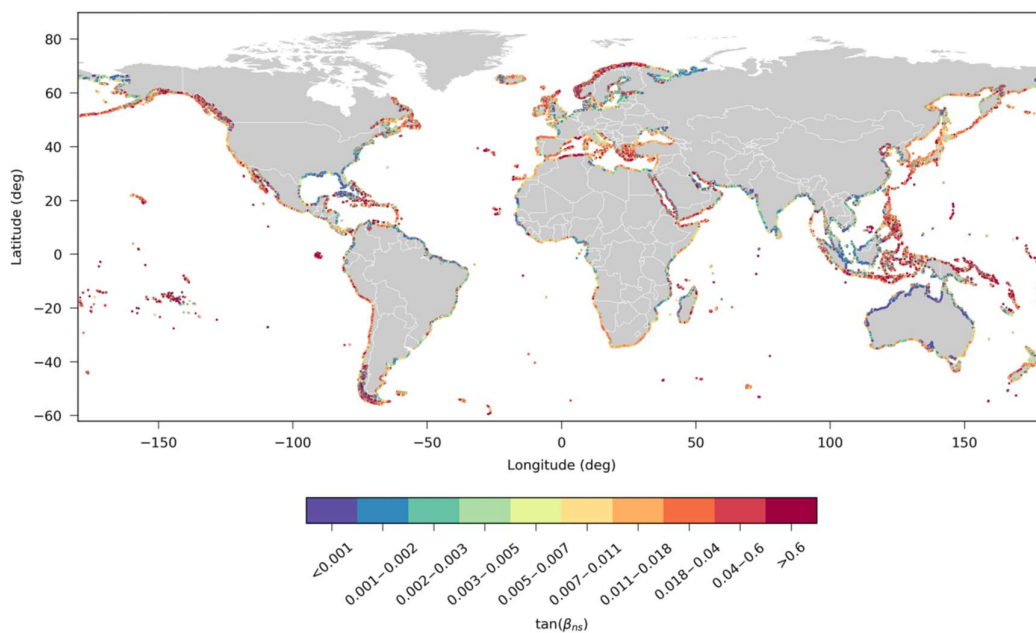


Figure 3.4.2: Global map of nearshore slopes. Red colours indicate steeper slopes while blue colours indicate milder slopes. Note that in the colour scale the slopes have been grouped in non-equidistant increments in order to highlight the spatial differences.

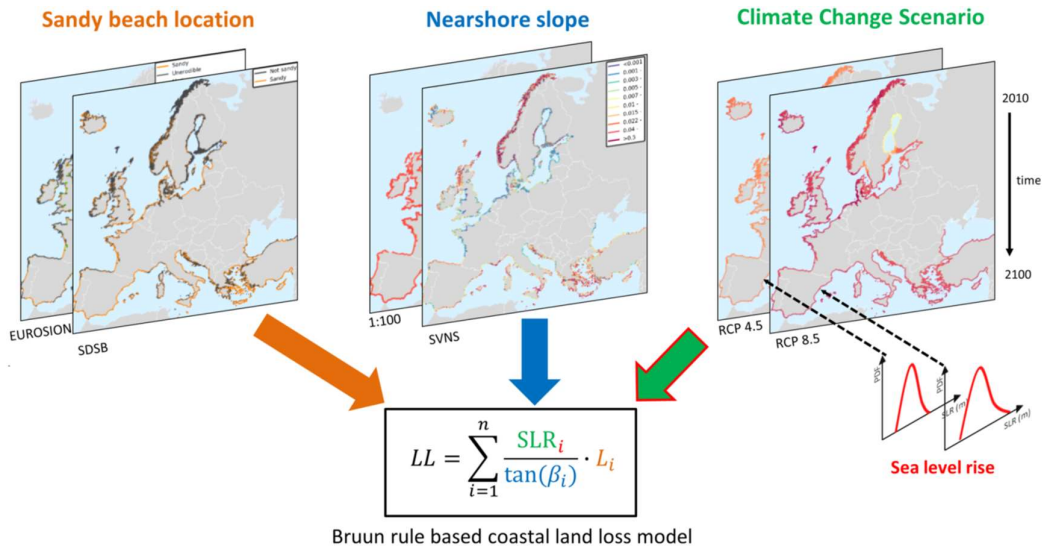


Figure 3.4.3: Schematization of the framework used herein to compute future European coastal land loss under the four different uncertain sources: (1) sandy beach location data, (2) nearshore slope data, (3) climate change scenario, and (4) sea level rise projections.

### 3.4.3 Results

#### PROJECTIONS OF SHORELINE RETREAT AND LAND LOSS

Using the SDSB and SVNS data, by 2050 a European average SLR driven potential shoreline retreat (in the absence of ambient shoreline changes) of between 18.1 and 53.9 m (5%-95% confidence interval) under RCP 8.5, relative to the baseline year 2010 (Figure 3.4.4). At the end of the century, these projections reach values between 51 and 241.5 m. The uncertainties are related to the contribution of steric SLR, ice sheets, glaciers and land–water storage. At the end of the century, the uncertainty related to the dynamic behavior of the Antarctic ice sheet dominates the total uncertainty of the SLR projections, which consequently introduces a large uncertainty to the end of century shoreline retreat and coastal land loss values. Only in the North Baltic Sea is the shoreline retreat significantly low due to glacial isostatic adjustment which reduces the regional relative SLR in the area.

For RCP 4.5, the potential shoreline retreat by 2050 is projected to be between 10.7 and 33.9 m (5%-95% confidence interval), i.e. almost 35% smaller than that for RCP 8.5. At the end of the century, mitigation could play an even more significant role with a reduction of almost 55% in average shoreline retreat under RCP 4.5 compared to that projected for RCP 8.5.

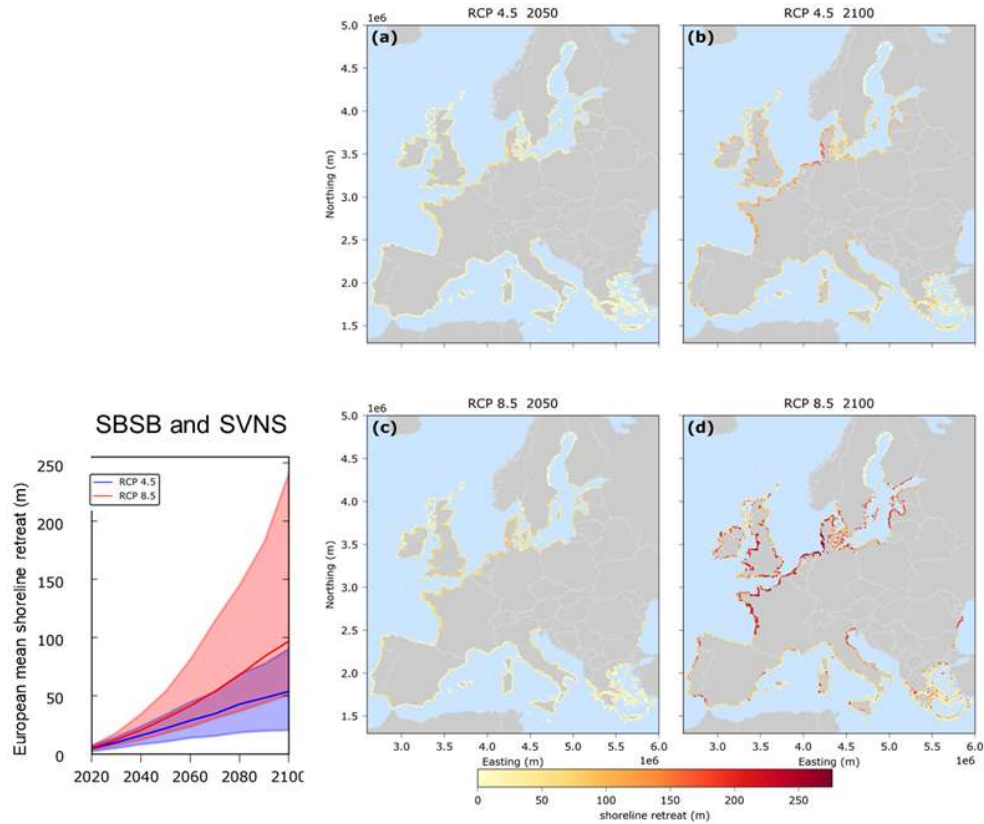


Figure 3.4.4: (Left) Projections of European average shoreline retreat relative to the baseline year 2010 for RCP 4.5 and RCP 8.5 using the SDSB and SVNS geophysical datasets. Thick lines indicated median and shaded area indicated the 5<sup>th</sup> and 95<sup>th</sup> percentiles. (Right) Maps of median shoreline retreat projections using the same geophysical datasets for 2050 and 2100.

With respect to the total coastal land loss, 473–1,410 km<sup>2</sup> (5-95% confidence interval) is projected to be lost across Europe under RCP 8.5 by 2050, using the SDSB and SVNS data. By 2100 this range is projected to be between 1,334 and 6,316 km<sup>2</sup>. Under RCP 4.5, these values are almost 35% and 55% smaller by 2050 and 2100, respectively.

The coastal retreat values calculated per location are aggregated to coastal land loss at the NUTS3 regional level, and then normalized according to the coastal length of each NUTS3 region. This results in maps that indicate vulnerable NUTS3 regions which could potentially lose large coastal areas with respect to their total coastal length.

**RCP 8.5 2100**

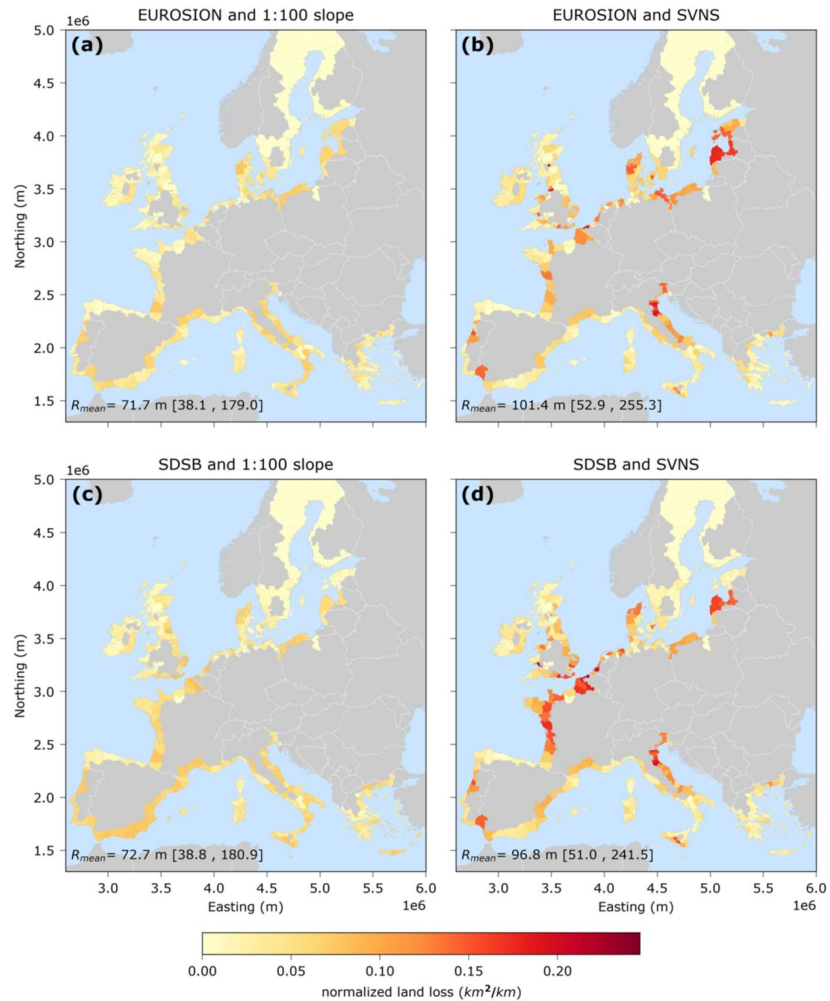


Figure 3.4.5: Normalized coastal land loss ( $\text{km}^2/\text{km}$ ) projections per NUTS 3 region for the median SLR at 2100 under RCP 8.5 (in the absence of ambient shoreline changes), relative to the baseline year 2010. The coastal land loss has been normalized per the coastline length of each NUTS3 region. Note that each region has a variable area and thus coastline length as defined by Eurostat. Each map represents an assessment with a specific combination of geophysical (sandy beach location and nearshore slope): (a) EUROSION and 1:100 slope, (b) EUROSION and SVNS, (c) SDSB and 1:100 slope and (d) SDSB and SVNS. The maps are projected in the ETRS89-LAEA system. The values at the bottom left of each map indicate the European average shoreline retreat (m) and are derived for median SLR projections, while in the brackets the average EU values are given for the of 5th to 95th percentiles of the SLR projections.

When using the SVNS data and irrespective of the sandy beach distributions dataset, highly vulnerable regions are identified on the Italian Adriatic coast, the French Atlantic coast, Belgium, The Netherlands, Denmark, Lithuania and Latvia (Figure 3.4.5).

### 3.4.4 Lessons learned

Using the presented analysis, maps of potential shoreline retreat and land loss were produced for all the European coastal zone, allowing us to identify areas where SLR will have the highest impacts on the sandy shores. These include regions at the Italian Adriatic coast, the French Atlantic coast, Belgium, The Netherlands, Denmark, Lithuania and Latvia. Still, the present study focused only on the effects of SLR in the absence of any other ambient changes due to sediment supply, changes in wave climate or human interventions. These extra processes can be critical for more informed decision

making when projections of the shoreline position need to be made. To this end, the landward extents of sandy beaches need to be known as well in order to produce more accurate estimates of land loss to coastal erosion. All these points are discussed in detail in Athanasiou et al. (2020).

The present work highlights the need for accurate geophysical data to represent the coastline in coastal erosion assessments. The uncertainties related to the representation of the geophysical coastal characteristics account for a high percentage of the uncertainties in the projections of SLR induced land loss in Europe, especially up to the middle of the 21<sup>st</sup> century. For the second half of the century uncertainties related to the SLR projections become more dominant.

Using the produced global dataset of nearshore slopes (Athanasiou et al., 2019) an important step in better representing the spatial variability of the coastline was made. This dataset has been used in a study led by JRC (end-user) to assess future shoreline changes on the global scale, including SLR induced retreat, ambient changes and storm erosion (Vousdoukas et al., 2020). In that study storm erosion was modelled using global wave and storm surge modelling, forced by a 6-member CMIP5 GCMs ensemble. Additionally, the global nearshore slope dataset was used in assessing uncertainties in global wave overtopping in a study led by the LEGOS joint research unit (Almar et al., 2021).

### 3.5 Efficient dune erosion prediction at the Dutch coast

#### 3.5.1 Brief introduction to the case

During extreme sea-storms the increased water levels induced by the combination of storm surge, tides and wave setup; and the high waves can lead to intense coastal erosion at sandy coasts (Figure 3.5.1). Coastal erosion at sandy coasts can have devastating impacts, by directly damaging assets in the eroded areas or by altering the coastal flooding susceptibility of the hinterland at low-lying areas (van Dongeren et al., 2018). These effects are expected to be exacerbated in the future due to climate change. The sandy dunes along the coast of the Netherlands act as one of the main protection mechanisms against coastal flooding. To this end, dune safety is a critical matter for coastal zone management, which is performed by Rijkswaterstaat (end-user), an agency of the Ministry of Infrastructure and Water Management of the Netherlands.

Process-based numerical models have shown good skill in predicting dune erosion during extreme events and have been applied for early warning systems and dune safety assessments (McCall et al., 2010). However, assessing dune safety at large spatial scales or with probabilistic methods (which involve a high number of simulations) with this kind of models can become challenging due to the high computational costs. To this end, here, a meta-model approach was developed to allow for quick estimation of dune erosion using a combination of process-based modelling and machine learning techniques. The developed meta-model based on Artificial Neural Networks (ANNs) allows for estimation of dune erosion volume in a matter of seconds only using a set of input parameters describing the storm conditions and the local morphology of the coast. This highlights its potential use for assessing impacts of climate change at large spatial scales (e.g., the whole Dutch coast).

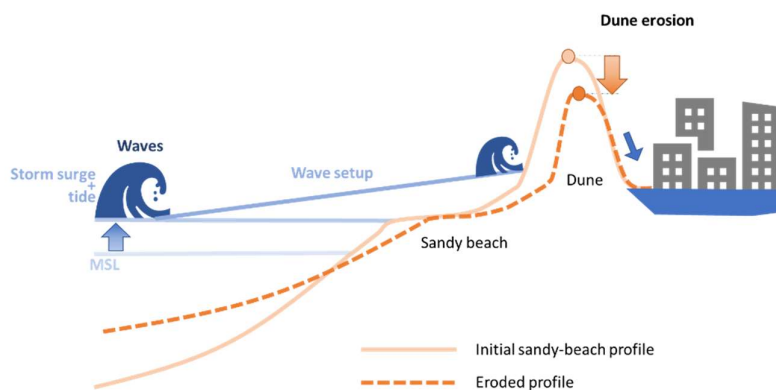


Figure 3.5.1: Schematic describing the processes of dune erosion during extreme sea storms.

#### 3.5.2 Methods

When using data driven techniques to predict physical impacts, care should be taken that the model has been trained with a representative set of cases, since data-driven methods are not good in extrapolating out of the range of their training space. Observations of pre-storm and post-storm elevations are not available at the Dutch coast for a large enough number of historic storms and alongshore locations to enable a good training of the data-driven model. To this end, we created a

synthetic but descriptive dataset using the dune impact model XBeach (Roelvink et al., 2009), which has been validated at the Dutch coast (Figure 3.5.2).

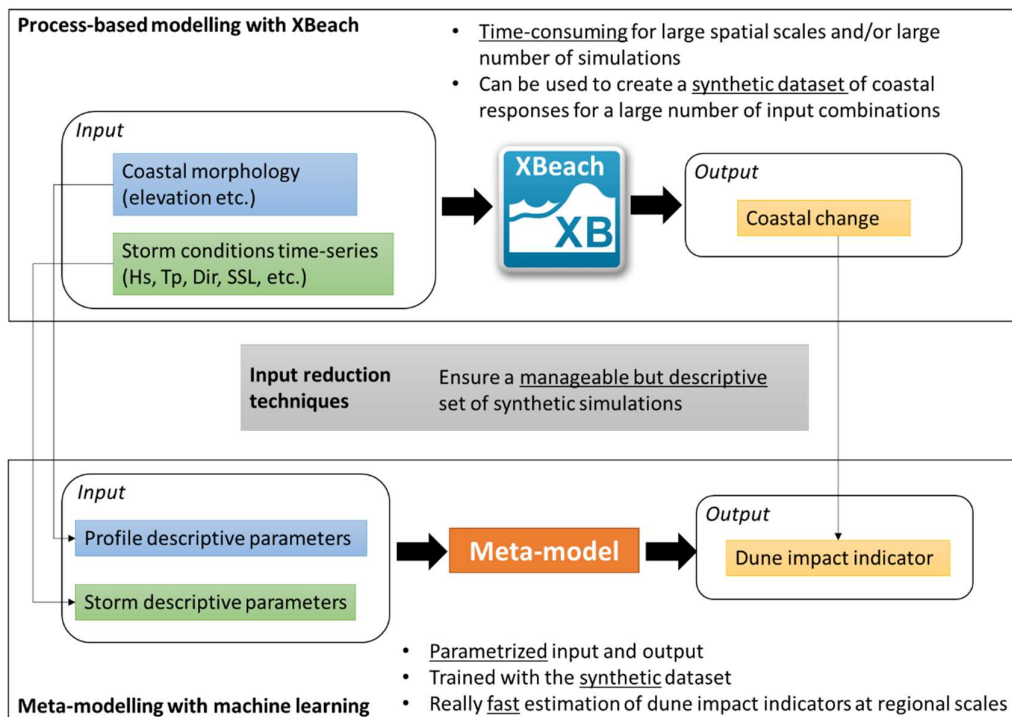


Figure 3.5.2: Flow diagram describing the basis of this study, on using a meta-model approach to efficiently estimate dune erosion.

### TRAINING DATA

There are elevation measurements available at ~1400 sandy beach and dune locations (profiles) along the Dutch coastline (Figure 3.5.3). Using this elevation transects together with offshore water level and wave observations, various local morphological and hydrodynamic characteristics of the coastline were extracted for each of the ~1400 profiles (Figure 3.5.4). An extensive study based on clustering techniques was undertaken, to use a selection of these parameters to choose a representative subset from these ~1400 profiles, that is descriptive of dune erosion processes for the whole Dutch coast. Using 10 morphological and hydrodynamic parameters, that were found to be the most important, along with information on simulated dune erosion, a subset of 100 profiles were chosen (93% input reduction), called typological coastal profiles (TCPs).

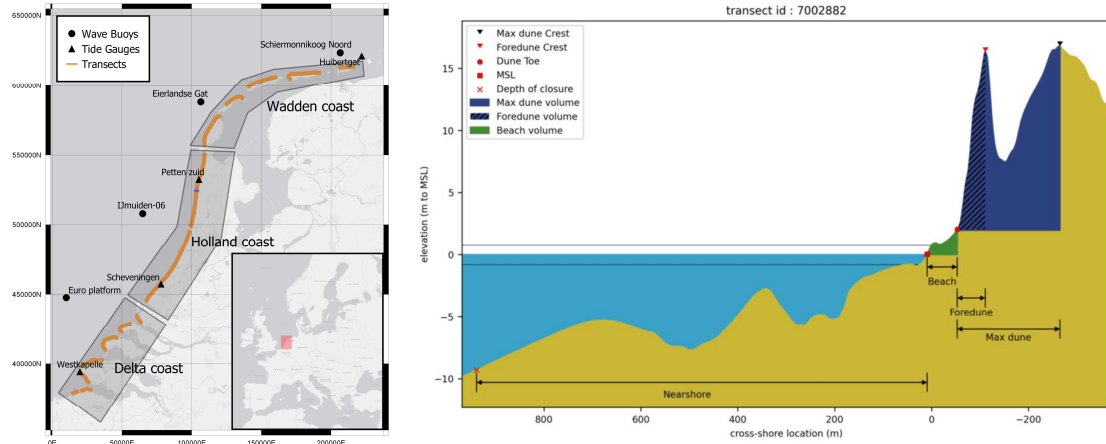


Figure 3.5.3: (Left) Map of the Dutch coast indicating the location of transects and measuring stations. (Right) An example of a cross-section of the elevation at one transects, indicating the various morphological parameters that were extracted

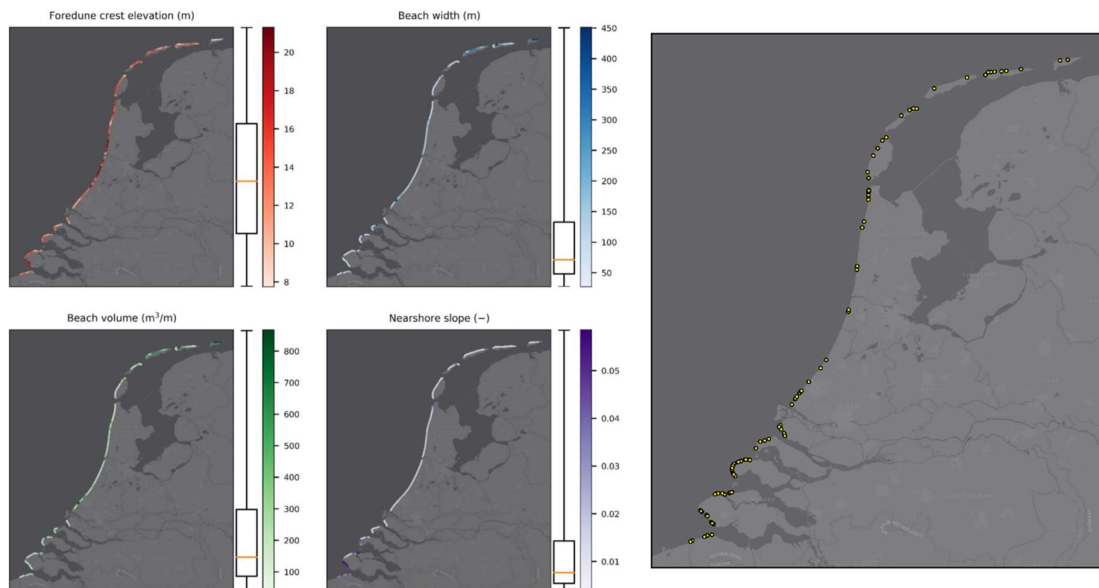


Figure 3.5.4: (Left) Maps of the spatial variability along the Dutch coast of four morphological parameters of the various parameters that were extracted at the Dutch coast. (Right) Map with the location of the 100 typological coastal profiles selected with the clustering technique.

An extended analysis on the clustering methodology that was used to extract these 100 is presented in the following publication:

Athanasίου, P., van Dongeren, A., Giardino, A., Vousdoukas, M., Antolinez, J.A.A.A., Ranasinghe, R., (2021), A Clustering Approach for Predicting Dune Morphodynamic Response to Storms Using Typological Coastal Profiles: A Case Study at the Dutch Coast. *Front. Mar. Sci.* 8, 1–20. <https://doi.org/10.3389/fmars.2021.747754>

For the development of the meta-model, a descriptive set of storm conditions should be assessed, to enable a good predictive skill for any storm event that could occur at the Dutch coast. To this end a multivariate extreme value analysis was followed, using historic extreme storms, from a record of wave conditions and water levels across four offshore wave stations (Figure 3.5.3). For each storm

event, the maximum significant wave height ( $H_s$ ), the concurrent peak wave period ( $T_p$ ), the storm surge level (SSL) and the duration of the storm ( $D$ ) were extracted. Then marginal distributions were fitted to each storm variable and a copula-based approach was used to simulate a synthetic set of 100,000 events, while preserving the interdependencies between the storm variables (Li et al., 2014). Then using a maximum dissimilarity algorithm, the 100 most dissimilar events were chosen to further use in the meta-modelling framework.

The combination of the 100 representative coastal profiles and the 100 representative offshore storm conditions, led to a total of 10,000 cases that were simulated with XBeach to assess dune erosion. For each simulation, the dune erosion volume (DEV) was extracted as an indicator of the intensity of the erosion impact. This metric describes the amount of sand that is lost from the dune after a storm event and is an important measure of dune safety. These 10,000 cases composed the training dataset for the meta-model, while an extra ~2,500 simulations were performed as a benchmark dataset to assess the predictive capacity of the meta-model and avoid overfitting.

**META-MODEL**

The meta-model developed herein is based on Artificial Neural Networks (ANNs), which are trained with the training dataset described in the previous sections. Artificial Neural Networks (ANNs) are computational networks that are a subset of machine learning and more specifically deep learning algorithms, inspired by the neuron structure of the human brain. The meta-model followed a 2-step approach with 1) a classification ANN, which predicted if there is going to be dune erosion or not, and 2) a regression ANN which gave an estimate of the actual dune erosion volume (DEV) in  $m^3/m$ . The input needed for a prediction included 14 parameters, with 10 parameters describing the local profile characteristics and 4 parameters describing the offshore storm conditions (Figure 3.5.5). A more comprehensive analysis of the development of the meta-model and the configuration of the ANNs and their results will be included in a publication which is under preparation:

*Athanasiou, P., van Dongeren, A., Giardino, A., Vousdoukas, M., Antolinez, J.A.A., Ranasinghe, R., Estimating dune erosion at the regional scale using a meta-model based on Neural Networks (2022, in preparation)*

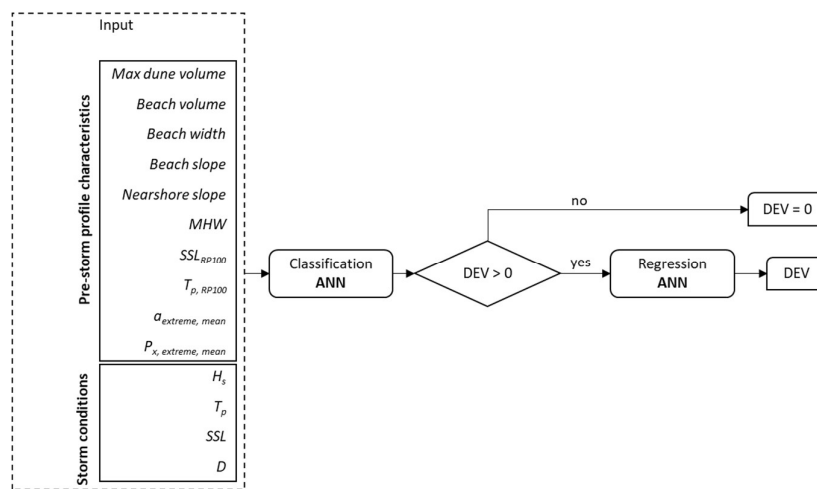


Figure 3.5.5: Meta-model configuration with input parameters, the classification ANN and then the regression ANN. For a description of the input parameters please see Athanasiou et al. (2021).

### 3.5.3 Results

The validation against the benchmark dataset showed that the meta-model had a high predictive skill. The classification ANN was able to predict if there is going to be dune erosion or not, with an average accuracy of 94% against the benchmark simulations. Moreover, the regression ANN had an average skill score of 0.82 with a RMSE of ~19 m<sup>3</sup>/m against the benchmark simulations. The meta-model was tested against available observations of dune erosion for 3 historic storms, showing good skill in capturing the observed dune erosion variability. Overall, the meta-model was able to produce a prediction for all the 1400 profiles of the Dutch coast in a matter of seconds for one incoming storm.

### 3.5.4 Future applications

While the presented meta-model is tailored for the Dutch coast, since the training dataset was representative to the conditions encountered at the Dutch coast only, the general framework is applicable for any sandy coast around the world. The meta-model offers a fast tool to efficiently assess climate change impacts on dune safety. Using projections of sea level pressure and wind fields from Global Climate Models (GCMs) or Regional Climate Models (RCMs) (connecting to the work of WP4 of EUCP), projections of storm surge level and wind conditions can be made. For example, Vousdoukas et al. (2018) used an ensemble of 6 CMIP5 model members to predict global storm surge levels and wind conditions under RCP 4.5 and RCP 8.5. These 6 members were chosen as the ones that described best the relevant ocean processes that can affect storm generation, surge and wave statistics. A study on the effects of climate change in dune safety at the Dutch coast could be made if these projections were used to force the developed meta-model with historic and future storms conditions, to compare dune erosion statistics. Due to the computational speed of the presented meta-model this could be feasible for assessing these effects for all of the Dutch coast (260 km length) with the ensemble surge and wave projections under both RCP4.5 and RCP8.5. Improvements in the current framework include the representation of the wave directionality during the dune impact simulations which currently is assumed conservatively as normal to the coast.

## 3.6 Multi-year forecast of drought and heat stress condition over global wheat harvesting region

### 3.6.1 Brief introduction to the case

Unfavorable and extreme climate events such as drought and heat stress affect wheat production and food security globally. Predicting such climate events in the next decade is of great interest for decision-makers, as this time horizon coincides with the strategic planning of many stakeholders in the wheat sector. To address this, we assess the forecast quality in predicting the evolution of drought and heat stress conditions using two proxy user-oriented drought and heat stress indicators: Standardised Potential Evapotranspiration Index (SPEI6) and Heat Magnitude Day Index (HMDI3) on a multi-annual timescale (forecast years 1 to 5). We present the probabilistic skill and reliability of decadal forecast to predict these indices for the months preceding wheat harvest on a global spatial scale. Following this, we demonstrate the potential applicability of these forecasts to enhance the adaptation and mitigation activities in the wheat sector by presenting the forecast of multi-year averaged SPEI6 and HMDI3 based on categorical events for the period 2020-2024.

The presented study for the wheat sector is developed in close collaboration with the Joint Research Center (JRC) of the European Commission. In recent years, JRC (science area: Agriculture and food security) has been actively involved in exploring the added value of decadal climate information for building a reliable climate service for agricultural needs on a multi-annual to decadal timescale. In addition, the study was further developed under the framework of the Copernicus Climate Change Services (contract number: C3S\_34c), where a prototype climate service product was developed for agriculture stakeholders in an effort to showcase the usability of the multi-year predictions for decision-making.

The methodology used in this study is published in the following article:

*Solaraju-Murali, B., Gonzalez-Reviriego, N., Caron, L.P., Ceglar, A., Toreti, A., Zampieri, M., Bretonnière, P.A., Samsó Cabré, M. and Doblas-Reyes, F.J. (2021). Multi-annual prediction of drought and heat stress to support decision making in the wheat sector. npj Climate and Atmospheric Science, 4(1), pp.1-9. <https://doi.org/10.1038/s41612-021-00189-4>*

### 3.6.2 Data and Methods

#### **DATA**

This study uses decadal forecasts from four different decadal prediction systems (42 members in total): 10 members from EC-Earth3 (Bilbao et al., 2021); 10 members from DePreSys4 (Sellar et al., 2020), 10 members from MPI-ESM1-2-HR (Müller et al., 2018) and 6 members from CMCC-CM2 (Cherchi et al. 2018). These are a set of 10-year long initialized forecasts that were simulated by explicitly prescribing the contemporaneous state of the climate system at the start of the simulation (November 1 of each year from 1960 to 2020), while also accounting for changes in radiative forcing (both natural and anthropogenic).

For this case study, we restrict our analysis to the first five forecast years over the global spatial domain where (and when) the winter wheat is harvested. Figure 3.6.1 presents the regions over which the wheat is grown along with the harvesting month. The information of the local wheat harvesting month is retrieved from the MIRCA2000 dataset (Portman et al., 2010).

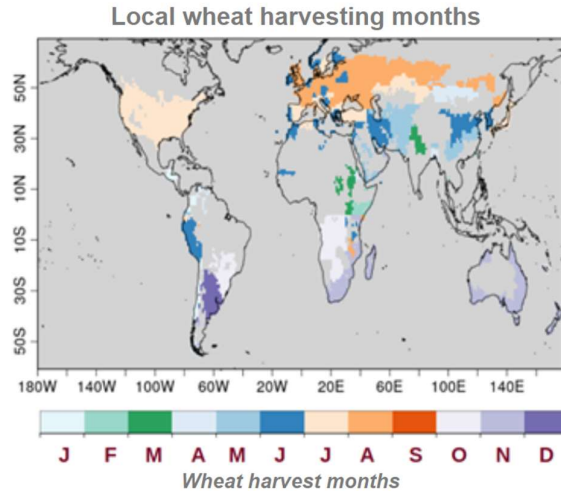


Figure 3.6.1: Wheat harvest month over global wheat-growing areas. For each grid box, the indices considered for this case study is estimated for the months preceding the harvest of wheat on a global spatial scale, and therefore, the presented results in this evaluation will correspond to different times of the year for different regions.

**METHODS**

We use JRA55 (Kobayashi et al., 2015) as a reference dataset to assess the quality of the decadal hindcasts in predicting the estimated indices on a multi-annual timescale. The choice of JRA-55 was motivated by the long continuous coverage of this product (1958—present) and by its high temporal coherency, with regards to daily maximum temperatures for computing HMDI3 index.

An overview of the steps involved in this assessment is presented in Figure 3.6.2 and described in detail in Solaraju-Murali et al. 2021.

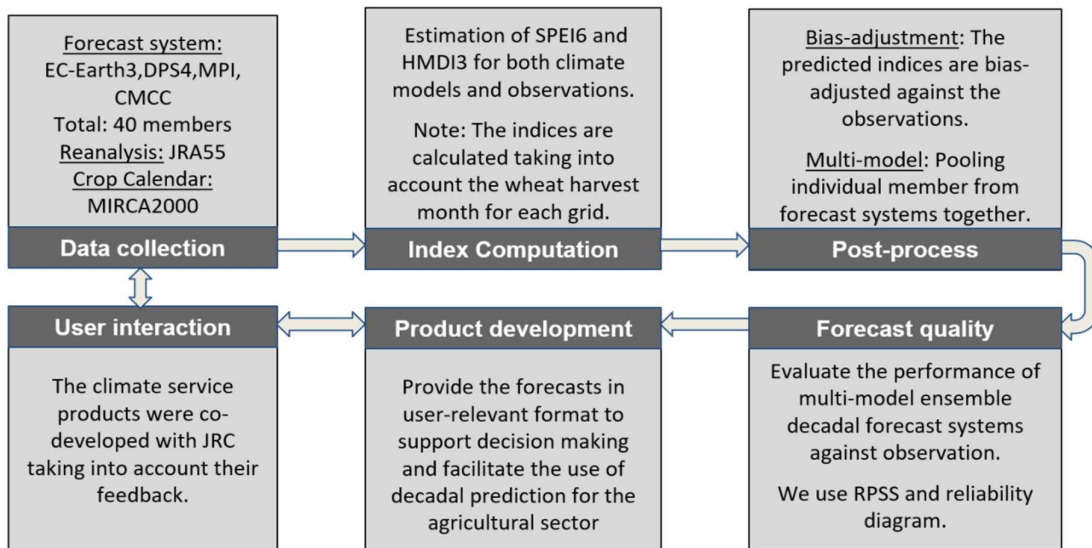


Figure 3.6.2: Main steps involved in the development of this study

### 3.6.3 Results

Figure 3.6.3 presents the predicted likelihood map (in %) of the most likely tercile (labelled as below-normal, normal and above-normal) of drought and heatwave occurrences using the indices corresponding to the wheat harvesting season (in Fig. 3.6.1). Darker shades of colours correspond to a higher probability of occurrence of the event falling into the lower, middle, and upper tercile category of proxy drought (SPEI6) and heat stress indicator (HMDI3).

Above-normal category (below-normal category) values of SPEI6 correspond to periods of wet (dry) conditions. On the contrary, the above-normal category (below-normal category) values present high-intensity (low-intensity) heatwave events. The decadal predictions for both indices show an increase in drought (below-normal category) and heatwave (above-normal category) events over most of the wheat-growing regions prior to the harvest months for the period 2020–2024.

Evaluating the quality of the predictions is considered a fundamental step in climate prediction because it assesses whether the prediction system can be trusted to forecast certain event categories (such as the ones presented in Fig. 3.6.3) and/or whether it offers an improvement with respect to the climatological forecast. The probabilistic skill and reliability in predicting the SPEI6 and HMDI3 over the wheat harvesting regions are presented in Figs. 3.6.4 and 3.6.5, respectively.

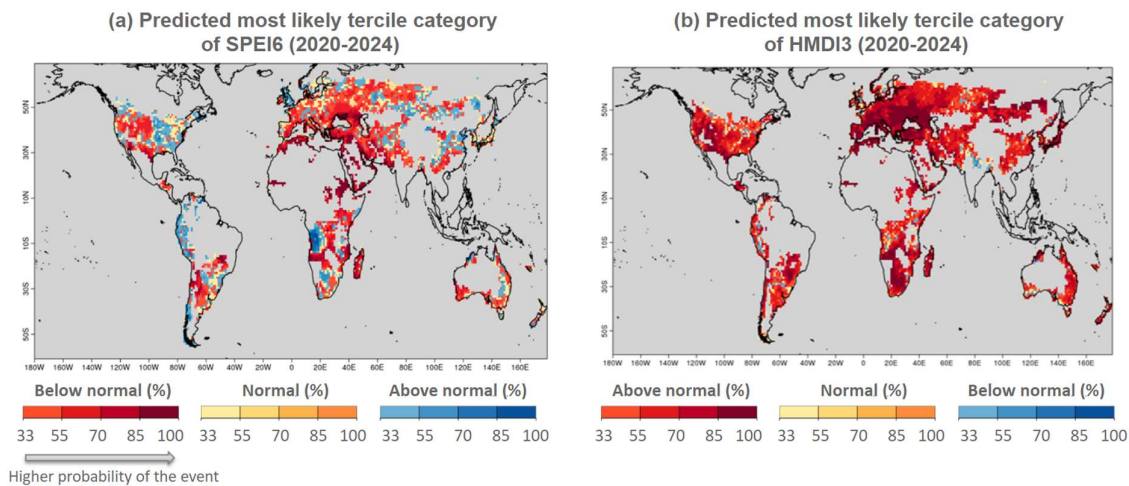


Figure 3.6.3: Most likely tercile category (below-normal, normal and above-normal) of SPEI6 (a) and HMDI3 (b) for the years 2020-2024 over the global wheat harvesting regions are displayed, in which the coloured grids show the category with the highest probability of occurrence.

RPSS provides a measure of the skill of decadal forecasts in predicting the probabilities of the categorical events (tercile in our case) of the estimated index. Positive RPSS values indicate that the decadal predictions are more skillful compared to a simple climatological multi-year approach in predicting terciles of the estimated indices distribution. A map of RPSS for SPEI6 is shown in Fig. 3.6.4a. A positive and significant value of RPSS is found over several regions, particularly over the Mediterranean, Middle East, and South Africa, whereas a negative skill is found over parts of the United States, South America, Russia and northern Australia. For HMDI3, the best scores are achieved over Europe, the Western United States and South Africa, and the negative scores are found over the Eastern United States, South America and Angola (Fig. 3.6.4b).

The reliability diagram (Fig. 3.6.5) presents the reliability of the predicted probabilities of tercile categories over the wheat harvesting regions globally. Reliability diagrams are particularly useful to identify whether a forecasting system under- or over-forecasts any particular category. For a forecast to be reliable, the average forecast probabilities should match the observed relative frequencies; thus, the colored lines in the graph should fall close to the diagonal. For SPEI6, the red (blue) line, corresponding to below-normal (above-normal) category, demonstrates the reliability in predicting the dryness (wetness) event by the forecast system. The multi-year prediction of SPEI6 is found to be reliable for the below-normal and above-normal categories (Fig. 3.6.4a).

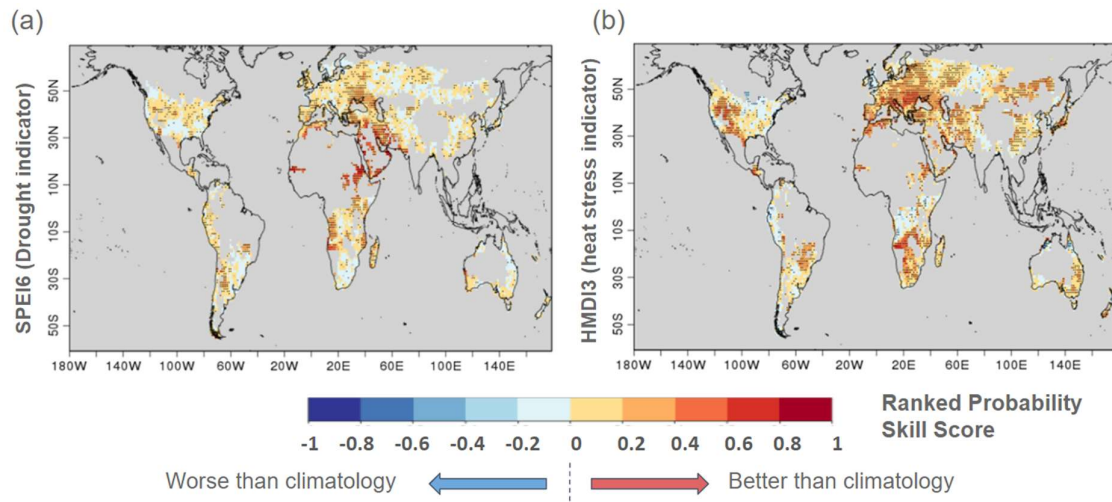


Figure 3.6.4: Ranked probability skill score (RPSS) for tercile events of predicted SPEI6 (a) and HMDI3 (b) averaged over forecast years 1–5, with respect to the JRA55 reference climatology during the winter wheat harvest months for the period 1961–2014. Dotted grid boxes represent values statistically significant at 95% confidence level.

On the other hand, the reliability diagram for HMDI3 over the global wheat-growing regions is presented in Fig. 3.6.4b. The below- and above-normal categories for both the domains are found to be reliable, whereas the normal category is under-confident when the forecast provides high probability estimates. Similarly, the normal category of SPEI6 is unreliable. This result is not entirely surprising since it has been shown that predicting the HMDI3 normal category tends to be more difficult as such events are known to have weak driving signals (Van Den Dool et al., 1991).

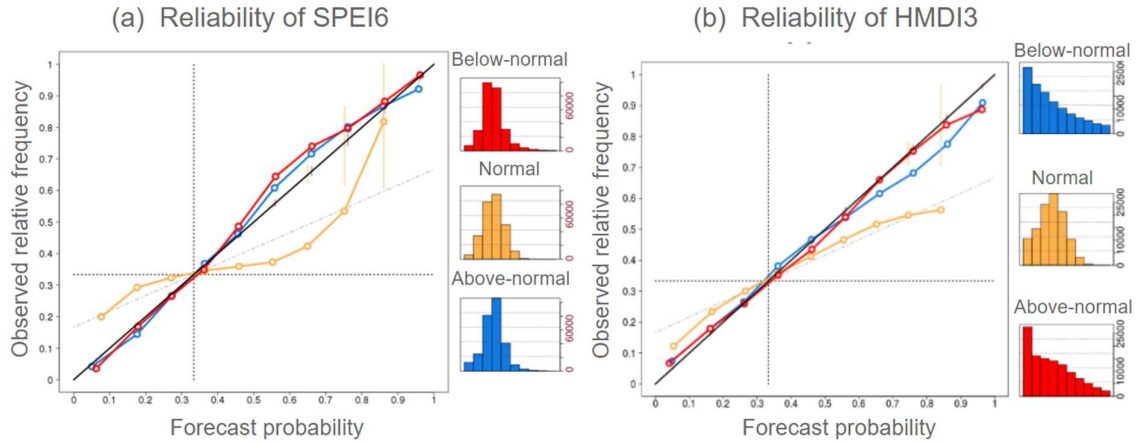


Figure 3.6.5: Reliability diagram of predicted SPEI6 (a) and HMDI3 (b) for the forecast years 1–5 during the winter wheat harvest months on a global spatial domain. A perfectly reliable system should result in a line that is as close as possible to the diagonal

### 3.6.4 Lessons learned

This work explored the ability of initialized decadal forecast at predicting drought and heat stress conditions over global wheat harvesting regions, an important first step in determining whether these products can provide useful, and ultimately actionable, information to stakeholders in the wheat sector, a sector that has been identified as one of the most vulnerable to climate-related risks (Zampieri et al., 2017; Bruno Soares et al., 2018).

The results reveal that decadal predictions hold promise in predicting SPEI6 and HMDI3 in multi-annual time scale, as these indices are found to be skillful (in comparison to the climatological forecast) and reliable over several wheat harvesting regions, particularly over Europe and the Middle East during the wheat harvest months. This implies that there exist opportunities to support wheat stakeholders in their decision-making processes, policies development, implementation, and evaluation on a multi-annual timescale. The proposed methodology can be easily adapted to different crops (such as rice and maize) or to other sectors where water management plays a fundamental role.

## 3.7 Multi-year forecast of surface wind

### 3.7.1 Brief introduction to the case

This case study aims at generating and evaluating different forecast products relevant to the wind energy sector at interannual to decadal time scales. The variability of surface wind speed affects wind energy production (Torralba et al., 2017; Lledó et al., 2019). Thus, it might be of high interest to stakeholders in both the wind energy sector to know such variations one or several years ahead. Wind energy producers could use this information to schedule maintenance tasks of wind farms when a period of long wind calms is expected to occur (which is also known as “wind droughts”). Besides, companies in the sector could benefit from knowing regions where the surface wind speed is foreseen to change so that they have extra information to anticipate renewable energy generation and demand (Soret et al., 2019).

Before providing any forecast product, the forecast quality assessment is an essential step for identifying windows of opportunity (e.g., forecast periods and regions) with skill to provide high-quality and reliable information that can be used for decision making by users (Merryfield et al., 2020). The Decadal Climate Prediction Project (DCPP; Boer et al., 2016) of the Coupled Model Intercomparison Project Phase 6 (CMIP6; Eyring et al., 2016) now provides the most comprehensive set of decadal predictions from multiple forecast systems. The increasing availability of these simulations leads to the question of how to best post-process the raw output from the forecast systems so that the most reliable information is provided to users. For example, using a multi-model ensemble for the forecast products generation may increase the quality of forecast products generated from individual forecast systems. Also, all forecast systems have systematic errors due to approximation in the mathematical methods and lack of complete knowledge about the climate system. To partially correct this issue, calibration techniques could be applied to the raw simulations to make their statistical properties more consistent with the observed ones (Doblas-Reyes et al., 2005). In addition, using predictors such as the Atlantic Multidecadal Variability (AMV; Trenberth and Shea, 2006) or the North Atlantic Oscillation (NAO; Smith et al., 2020) instead of the surface wind output from the systems may improve the forecast quality (given that the surface wind is a variable which shows a generally low skill and not all the systems provide the necessary sub-daily surface wind data, while all of them provide monthly sea surface temperature and sea level pressure data needed for AMV and NAO calculation, respectively).

### 3.7.2 Data

The currently available CMIP6/DCPP multi-model ensemble consists of 169 members from 13 forecast systems. Some of these decadal predictions have been generated within the EUCP WP1. However, only a few forecast systems provide sub-daily surface wind data, which is needed for this study. Besides, most systems only provide hindcasts (i.e., retrospective forecast), restricting the ensemble size for forecast product generation in near-real time. In addition, the same forecast systems provide historical forcing simulations (i.e., retrospective climate projections). These historical simulations use prescribed forcings (natural and anthropogenic) to simulate the climate system. In contrast, decadal predictions use, in addition to external forcings, initial conditions (which are generated from observational-based data) to try to capture the internal variability of the climate system (i.e., the slow

oscillations that provide predictability at interannual to decadal time scales). The comparison between decadal predictions and historical simulations provides an estimation of the impact of system initialization. Information about the forecast systems and their simulations is shown in Table 3.7.1.

*Table 3.7.1: Forecast systems contributing to the CMIP6/DCPP and their specifications (available simulations at the time of the study). It is specified which forecast systems provide sub-daily surface wind data, and which ones provide near-real time data. All the forecast systems provide monthly sea surface temperature and sea level pressure data.*

Forecast system	n° of DCP members	n° of HIST members	Sub-daily surface wind data	Near-real time data	Month of initialisation	Reference
BCC-CSM2-MR	8	3	No	No	January	Wu et al. (2019)
CanESM5	20	40	No	Yes	January	Swart et al. (2019)
CESM1-1-CAM5-CMIP5	40	40	No	No	November	Yeager et al. (2018)
CMCC-CM2-SR5	10	1	No	Yes	November	Cherchi et al. (2018)
EC-Earth3-i1	10	10	Yes	Yes	November	Bilbao et al. (2021)
EC-Earth3-i2	5	-	Yes	No	November	Tian et al. (2021)
HadGEM3-GC3.1-MM	10	4	No	Yes	November	Sellar et al. (2020)
IPSL-CM6A-LR	10	32	Yes	No	January	Boucher et al. (2020)
MIROC6	10	10	No	No	November	Tatebe et al. (2019)
MPI-ESM1.2-HR	10	10	Yes	No	November	Müller et al. (2018)
MPI-ESM1.2-LR	16	10	No	No	November	Mauritsen et al. (2019)
MRI-ESM2-0	10	5	No	No	November	Yukimoto et al. (2019)
NorCPM1	10	30	No	No	October	Bethke et al. (2021)

For the evaluation, two different reference datasets have been used to account for the observational uncertainty when estimating the quality of the surface wind predictions: ERA5 (Hersbach et al., 2020) and JRA-55 (Kobayashi et al., 2015), both at hourly frequency. Monthly sea surface temperature data from the GISTEMPv4 dataset (Lenssen et al., 2019) has been used to compute the observed AMV index. For the observed NAO index, monthly sea level data from the ERA5 reanalysis has been used.

All the data has been masked over regions not relevant to the wind energy sector, keeping land regions (except Antarctica) and offshore regions.

### 3.7.3 Methods

#### ***EVALUATION, FORECAST AND REFERENCE PERIODS***

The decadal predictions for the average of the forecast years 1 to 5 have been evaluated over the 1961-2018 period (start dates 1960-2013). For the examples of forecast products, the forecast systems that provide near-real predictions, and start dates until 2020 (predictions for the 2021-2015 period) have been used. Annual, winter (December-January-February; DJF) and summer (June-July-August; JJA) means have been considered to assess both multi-annual and multi-seasonal wind predictions. The predictions from the forecast systems initialized in January (see Table 3.7.1) have not been considered for the first forecast winter since they do not have data for the first December.

Before evaluating the decadal predictions, anomalies have been computed relative to the 1981-2010 climatology. This is a necessary step to remove the model drift (Boer et al., 2016) and for correcting the differences between the observed and simulated climatologies. The same reference period has been used to compute the climatology of the reference datasets and historical simulations. Also, the thresholds between the equiprobable categories for the probabilistic products have been estimated using the same period.

#### ***DYNAMICAL MULTI-MODEL***

The dynamical multi-model has been built by pooling all members from the forecast systems that provide sub-daily surface wind data. Besides, another multi-model approach, which consists of averaging the ensemble means (probabilities) from the different forecast systems to create the deterministic (probabilistic) products, has been tested. Also, the calibration technique described in Doblas-Reyes et al. (2005) has been used to estimate the impact of calibration on the quality of the multi-model forecasts.

For the sub-daily surface wind speed data, there are a total of 35 decadal predictions members and 52 historical simulations members (see Table 3.7.1). Such multi-model ensembles have been compared to assess the impact of the forecast system initialisation. Due to the different spatial resolution of the forecast systems, all the data has been interpolated to a 2.5° grid resolution before building the multi-model ensemble.

#### ***LINEAR REGRESSION MULTI-MODELS***

A perfect prognosis approach has been applied to generate the linear regression multi-models' forecasts. This methodology uses past observations to calculate the regression coefficients, while it uses the model outputs to create the forecasts (Ramon et al., 2021). It uses a "predictor" (e.g., an index such as the AMV or NAO indices) to forecast a "predictand" (e.g., the surface wind speed). The AMV and NAO indices' definitions used in this study can be found in Doblas-Reyes et al. (2013) and Smith et al. (2020), respectively. The steps of the perfect prognosis approach are the following:

- Train the model with the observed predictor and the observed predictand, obtaining the coefficients of the linear regression model. In this step, it is essential to perform the training in cross-validation mode. This means that, to get the coefficients in each time step, the observations that would not be available are not considered, as would be the case for real-

time forecasting. In the case of this study, as the forecast years 1-5 are used, the cross-validation removes nine time-steps. For example, when obtaining the coefficients for the prediction of 2001-2005, time steps 1998-2001, ..., 2005-2009 are not considered. The skill drastically decreases when performing the training in cross-validation mode, but it is crucial to not overestimate the actual skill of real-time predictions. Some tests have been carried out only leaving one time step out (leave-one-out mode, which is usually used), finding a much higher skill. However, it could not be done in near-real time, so the results presented here are performed with leave-nine-out cross-validation to be as more robust as possible.

- Use the predicted predictor (e.g., the predicted NAO) to predict the predictand (e.g., to predict the surface wind speed).

Four different regression multi-models have been created:

- Short regression multi-model: linear regression model using the perfect prognosis approach built with the ensemble members from those systems that provide dynamical predictions of surface wind speed (see Table 3.7.1). It is used for comparison with the dynamical multi-model as they use the same ensemble members.
- Large regression multi-model: same as the short regression multi-model but using the ensemble members from all the forecast systems (see Table 3.7.1). It is used to estimate the impact of the ensemble size, and to estimate the potential skill of the regression multi-model if all the forecast systems provide timely predictions.
- Near-real time regression multi-model: same as the short regression multi-model but only using the ensemble members from those forecast systems that provide near-real time predictions (see Table 3.7.1). It is used to estimate how much skill is lost because of not having all the predictions available in near-real time.
- Perfect regression model: same as the short regression multi-model but using the observed predictor as if it was the predicted predictor. It is used to estimate the potential skill that would be achieved if the predictor was perfectly predicted.

The linear regression multi-models (except the near-real time one) have been obtained in a 2.5° grid for comparison with the dynamical multi-model. The near-real time regression multi-model has been obtained in the original reference dataset's grid to get the predictions on the finest possible grid (which is one of the advantages of the perfect prognosis approach). For example, if using ERA5 for the training, the forecasts are obtained in a 0.25° grid. Then, the spatial resolution is increased by a factor of 10 when compared to the dynamical multi-model forecasts.

#### ***METRICS AND STATISTICAL SIGNIFICANCE***

To evaluate the deterministic products, the Anomaly Correlation Coefficient (ACC; Wilks, 2011) and the Root Mean Squared Error Skill Score (RMSSS; Wilks, 2011) have been used. For the probabilistic products based on tercile and quintile categories, the Ranked Probability Skill Score (RPSS; Wilks, 2011) and the Relative Operating Characteristic Skill Score (ROCSS; Kharin and Zwiers, 2003) have been used. A two-sided t-test has been applied to estimate the ACC significance at the 95% confidence level accounting for the time series' autocorrelation (Von Storch and Zwiers, 2001). The Random Walk test (DeSole and Tippett, 2016) has been used to assess the significance of the skill scores at the 95% confidence level. Besides, other metrics like the FairRPSS (Ferro, 2014), Spread-over-Error ratio (Fortin

et al., 2014), the Signal-to-Noise ratio (Scaife and Smith, 2018), and the Ratio of Predictable Components (RPC; Eade et al., 2014) have also been considered in the study.

The forecast quality assessment has been performed following the recommendations developed in the C3S\_34c contract (Prototype Service for Decadal Climate Predictions; <https://climate.copernicus.eu/c3s34c-prototype-service-decadal-climate-predictions>).

### 3.7.4 Results

Given the substantial number of results, only some examples of figures are shown here. The complete catalogue can be accessed through an R Shiny App specifically created for this case study (<https://earth.bsc.es/shiny/EUCP-wind-case-study/>).

Figure 3.7.1 shows the observed trend of the surface wind and quality estimates (ACC for deterministic forecast products, and RPSS and ROCSS for tercile categories for probabilistic forecast products) of the dynamical DCP multi-model for surface wind speed predictions for the averaged winters of the forecast years 1-5. The observed trend is found to be significant over large regions of all the continents. For example, there is a significant increase in the surface wind speed over Africa and a significant decrease over large regions of Europe and Asia. The dynamical multi-model shows skill over Central Europe, India and some limited regions of America and Africa. The ROCSS for the below and above normal categories shows a pattern similar to the ACC. The ROCSS for the below normal category is particularly important in this study as it is the skill in predicting wind droughts.

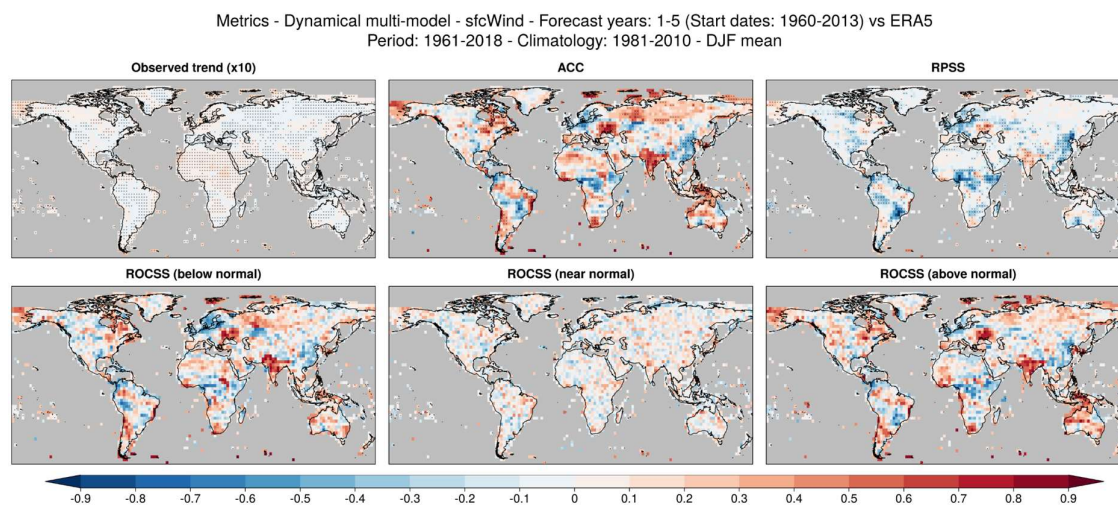


Figure 3.7.1: Observed trend of the surface with speed, ACC, RPSS, and ROCSS for tercile categories of the dynamical DCP multi-model ensemble in predicting the surface wind speed for the averaged winters of the forecast years 1-5. The evaluation period is 1961-2018 (start dates 1960-2013). The reference period for computing the climatology and thresholds is 1981-2010. ERA5 has been used as the reference dataset. Crosses indicate statistical significance of the trend, ACC and RPSS at the 95% confidence level.

The short and large regression multi-models (built using the NAO index as the predictor) show low skill in predicting the surface wind speed. This is partially due to the low skill in predicting the NAO index (see R Shiny App). In order to estimate the potential skill that would be reached if the NAO index is perfectly predicted, the forecast quality of the perfect regression model is shown in Figure 3.7.2. In the same figure, the observed teleconnections between the NAO index and the surface wind speed

are also shown, which are especially strong over Europe and North Africa (in addition to other regions over America and East Asia). The forecasts of the perfect regression model show high skill when measured with the ACC and ROCSS for below and above normal categories over large regions of Northern Europe and Northern Africa (where the leave-nine-out cross-validation has been applied as for the rest of regression models). Northern Europe is of particular importance for the wind energy sector as there are offshore wind farms over the North Sea. However, the NAO index has to be skillfully predicted to reach this forecast quality.

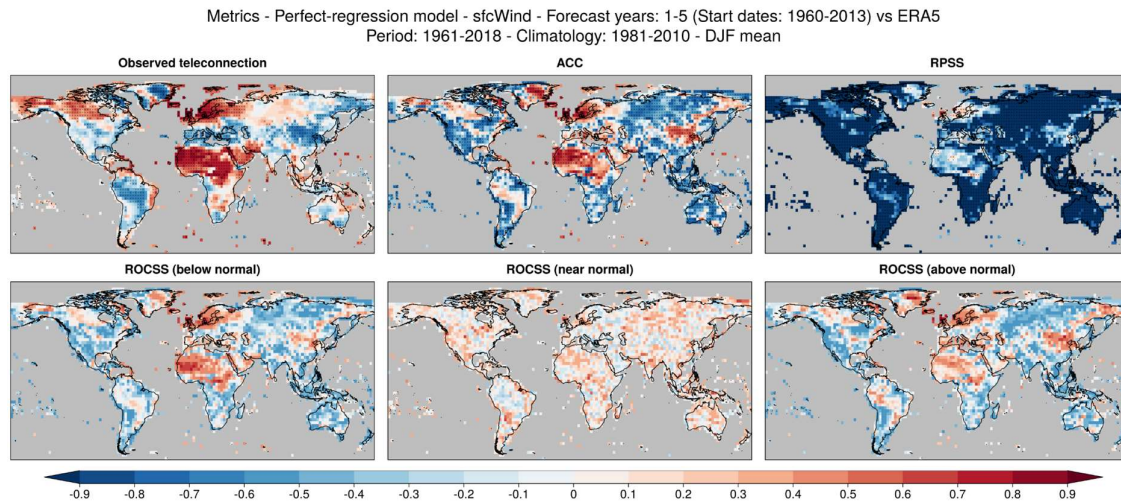


Figure 3.7.2. Observed teleconnection between the NAO index and the surface with speed, ACC, RPSS, and ROCSS for tercile categories of the perfect regression multi-model using the NAO as the predictor (i.e., potential skill if the NAO index was perfectly predicted) in predicting the surface wind speed for the averaged winters of the forecast years 1-5. The skill scores have been computed using climatology as the reference forecast. The evaluation period is 1961-2018 (start dates 1960-2013). The reference period for computing the climatology and thresholds between categories is 1981-2010. ERA5 has been used as the reference dataset. Crosses indicate statistical significance of the observed teleconnection, ACC and RPSS at the 95% confidence level.

Figure 3.7.3 shows an example of a probabilistic forecast product (based on tercile categories) for predictions of the surface wind speed over Barcelona for the forthcoming five winters. The forecasts have been generated with the near-real time regression model using the NAO as the predictor. The ROCSS is also shown for each tercile category, being negative for all of them (which means that the forecast is less skillful than the climatological forecast). If the skill in predicting the NAO is increased, potential climate services could be provided to inform users in the sector about future variations in the surface wind speed.

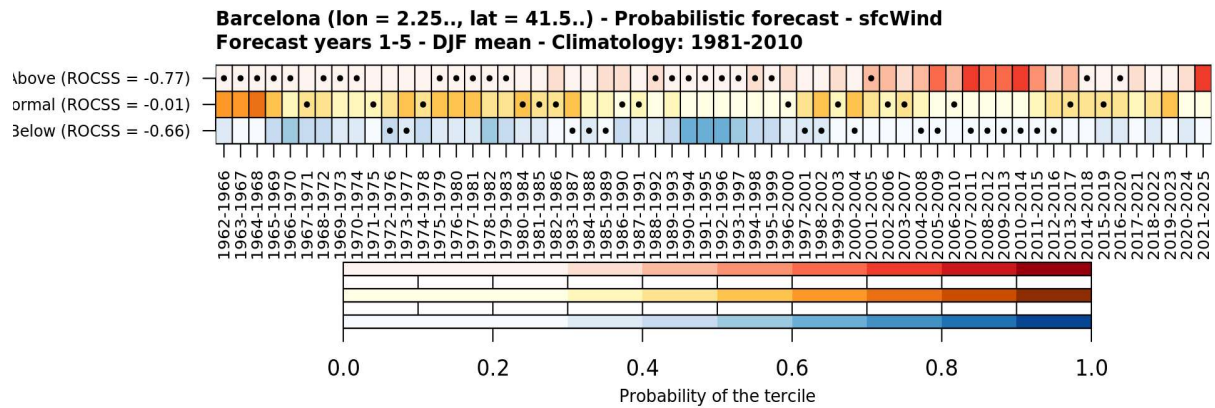


Figure 3.7.3. Example of probabilistic forecast product (tercile categories) for the surface wind speed in Barcelona during the averaged winters of the forecast years 1-5. The forecasts have been created with the near-real time regression model using the NAO as the predictor. Dots correspond to the observed tercile. Colours correspond to the forecasted probabilities for each tercile. The skill in predicting each category is shown with the ROCSS using climatology as the reference forecast. The evaluation period is 1961-2018 (start dates 1960-2013). The reference period for computing the climatology and thresholds is 1981-2010. ERA5 has been used as the reference dataset.

### 3.7.5 Lessons learned

- The dynamical multi-model ensemble shows limited areas with skill in predicting the surface wind speed. Significant skill has been found over Central Europe, India, and some regions of Asia, Africa, and America.
- A properly cross-validation applied (in the case of this study, leave-nine-years out since forecast years 1-5 have been assessed) when creating the linear regression model drastically decreases the forecast quality compared to the same methodology but applying leave-one-out cross-validation. However, it must be properly applied to avoid overestimating the actual skill.
- The AMV index is well predicted. However, due to the limited length of its timeseries, it cannot be considered as a good predictor.
- The NAO index has been found to be a good predictor for the surface wind speed over large regions of Europe and Africa, especially during the winter season. However, the skill of the forecast systems in predicting the NAO index is low, meaning that it is not a good input for forecasting until it is skillfully predicted.
- More work is needed to improve the quality of the predictions, and methodologies like the NAO-matching proposed by Smith et al. (2020) and the search for better predictors as in Borchert et al. (2021) are being considered.
- More forecasting centers should consider providing sub-daily surface wind predictions from their forecast systems. It is a huge amount of data, but it could benefit many users for preparation if a period of higher/lower wind speed is expected.

Further work will be carried out with the aim of increasing the skill of surface wind speed predictions at interannual to decadal time scales. Also, these results are expected to be used for the preparation of a scientific publication.

## 3.8 Projected streamflow changes for Europe from an ensemble of climate and hydrological models

In this case-study an ensemble of hydrological models from EUCP partners and end-user JRC were forced with EURO-CORDEX climate simulations. Performance-based weighting methods from WP2 partners were used to derive a more robust climate signal of European streamflow changes.

### 3.8.1 Brief introduction to the case

The impact of climate change on future streamflow changes is uncertain. One way to address this uncertainty is the use of an ensemble of climate and hydrological models. In collaboration with EUCP partners ETH Zurich and IIASA and end-user JRC a multi-model assessment was conducted where we tried to obtain a more robust result. Three hydrological models were used to account for the hydrological model uncertainty and to assess the consistency: wflow\_sbm (Deltares), CWatM (IIASA) and LISFLOOD (JRC). An ensemble of climate datasets from the EURO-CORDEX archive was used to represent climate model uncertainty. Two performance-based ensemble weighing methods were applied to obtain a more robust signal: the reliability ensemble averaging method (ICTP) and the Climate model Weighting by Independence and Performance method (ETH Zurich) that is implemented in ESMValTool (docs.esmvaltool.org; eScienceCenter). This resulted in discharge projections for high, low and mean river flows for 9 river basins spread over Europe.

The case study has been published and described in more detail in:

*Sperna Weiland F.C., Visser R.D., Greve P., Bisselink B., Brunner L., Weerts A.H., 2021. Estimating Regionalized Hydrological Impacts of Climate Change Over Europe by Performance-Based Weighting of CORDEX Projections, Frontiers, <https://doi.org/10.3389/frwa.2021.713537>*

### 3.8.2 Methods

#### **CASE-STUDY AREA**

Nine European catchments were chosen based on their size, climate conditions and geographical position (Figure 3.8.1).

#### **HYDROLOGIC MODELS**

Three distributed hydrological models have been used:

- The wflow\_sbm developed at Deltares (Imhoff et al., 2020; Eilander et al., 2021)
- The community water model CWatM developed by IIASA (Burek et al., 2020)
- LISFLOOD developed by JRC (Knijff et al., 2010)

All three models are distributed rain-full runoff channel routing hydrological models. They follow similar concepts but differ in their schematization. CWatM and LISFLOOD have been configured at the continental and global scale. wflow\_sbm is configured on a basin scale, but largely builds upon global datasets. Both CwatM and LISFLOOD have been calibrated, the parameterization of wflow\_sbm relies upon on physical datasets and pseudo-transfer functions.

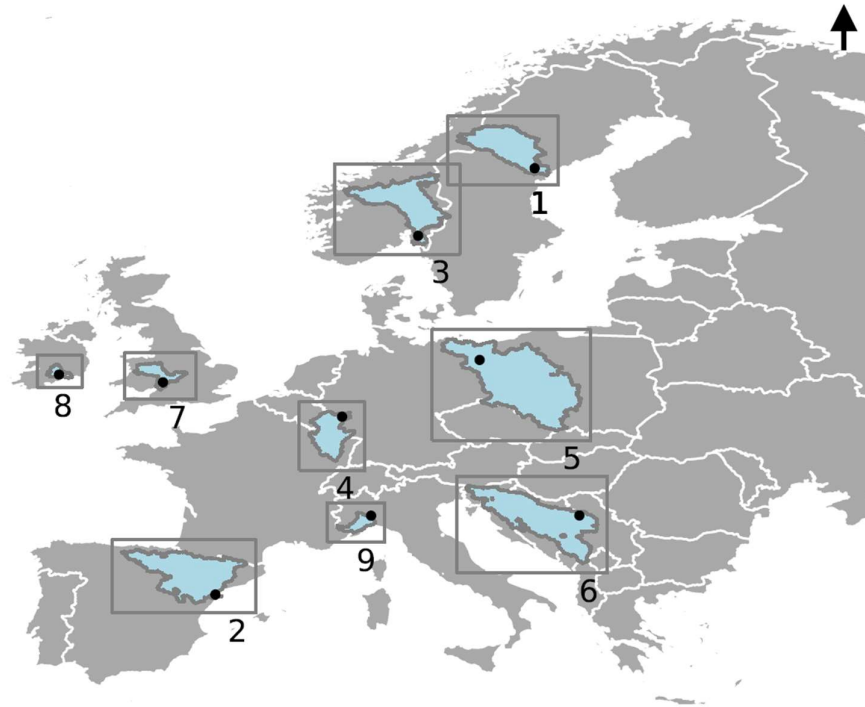


Figure 3.8.1: Geographical position of the catchments in Europe. Numbers indicate the river basins; the Ångermanälven (1), Ebro (2), Glomma (3), Moselle (4), Oder (5), Sava (6), Severn (7), Suir (8), and Tanaro (9). Dots indicate the gauge locations used in this study.

#### **EURO-CORDEX**

Daily output from a 23-member ensemble of EURO-CORDEX regional climate simulations (Jacob et al., 2020) covering the period from 1970 to 2060 at a spatial resolution of 0.11° degrees was used to force the hydrological models. The regional climate models are forced by a set of global climate models from the Coupled Model Inter-comparison Project 5 (CMIP5, see Table 3.8.1). For the future climate the Representative Concentration Pathway 8.5 (RCP8p5) was chosen to obtain a pronounced signal. The experiment relied upon readily available hydrological simulations and contains therefore some slight inconsistency. For the LISFLOOD simulations the CORDEX data sets were bias-corrected (Piani et al., 2010; Dosio and Paruolo, 2011) using E-OBS precipitation and temperature (Cornes et al., 2018).

#### **WEIGHTING METHODS APPLIED**

The first method applied is the Climate model Weighting by Independence and Performance (**ClimWIP**) method (Brunner et al., 2019). This method accounts for the historical GCM performance of meteorological variables considered relevant for the correct representation of regional hydrology. In addition, it considers the independence of the individual GCMs, effectively down-weighting models which are identified as closely related to one another.

The second method is the Reliability Ensemble Averaging (**REA**) method (Giorgi and Mearns, 2002). This method considers the model bias for the current climate and the GCM reliability in terms of the convergence of the GCM specific future discharge change with the weighted ensemble mean future change to calculate the overall GCM reliability factor.

Table 3.8.1: Overview of CORDEX simulations available for the three hydrological models, the X indicates that the hydrological model was run with this CORDEX GCM-RCM combination.

Nr	GCM	RCM	Wflow_sbm	CWatM	LISFLOOD
1	CNRM-CERFACS-CNRM-CM5	CLMcom-CCLM4-8-17	X	X	X
2	CNRM-CERFACS-CNRM-CM5	SMHI-RCA4	X	X	X
3	ICHEC-EC-EARTH	DMI-HIRHAM5	X	X	X
4	ICHEC-EC-EARTH	KNMI-RACMO22E	X	X	X
5	ICHEC-EC-EARTH	SMHI-RCA4	X	X	X
6	IPSL-IPSL-CM5A-MR	SMHI-RCA4	X	X	X
7	MOHC-HadGEM2-ES	SMHI-RCA4	X	X	X
8	MPI-M-MPI-ESM-LR	CLMcom-CCLM4-8-17	X	X	X
9	MPI-M-MPI-ESM-LR	DMI-HIRHAM5	X	X	
10	MPI-M-MPI-ESM-LR	KNMI-RACMO22E	X	X	
11	NCC-NorESM1-M	IPSL-WRF381P	X	X	
12	NCC-NorESM1-M	KNMI-RACMO22E	X	X	
13	NCC-NorESM1-M	SMHI-RCA4	X	X	
14	IPSL-IPSL-CM5A-MR	IPSL-WRF381P	X	X	
15	IPSL-IPSL-CM5A-MR	KNMI-RACMO22E	X	X	
16	MOHC-HadGEM2-ES	CLMcom-CCLM4-8-17	X	X	
17	MOHC-HadGEM2-ES	CNRM-ALADIN63	X	X	
18	MOHC-HadGEM2-ES	IPSL-WRF381P	X	X	
19	MPI-M-MPI-ESM-LR	CLMcom-ETH-COSMO-crCLIM-v1-1	X		
20	NCC-NorESM1-M	CLMcom-ETH-COSMO-crCLIM-v1-1	x		
21	ICHEC-EC-EARTH	CLMcom-CCLM4-8-17			X
22	INERIS	IPSL-WRF331F			X
23	MPI-M-MPI-ESM-LR	SMHI-RCA4			X

### 3.8.3 Results

The graphs in figure 3.8.2 display the historical discharge regime for the period 1981-2010 as simulated by the three hydrological models (from left to right: wflow\_sbm, CWatM, LISFLOOD) using the CORDEX datasets. As a reference the observed regime was plotted in black. For the wflow\_sbm model the simulation of the historical meteorological data (E-OBS) was also added to the graph to get an impression of hydrological model versus climate data bias. In general, there is large variation between the hydrological simulations driven with the different CORDEX datasets. The discharge regimes obtained with LISFLOOD show highest resemblance with the observed regime as this model has been calibrated and the CORDEX precipitation and temperature have been bias-corrected. This clearly reduces the spread between the discharges obtained from the different CORDEX datasets.

Table 3.8.2 and 3.8.3 present the projected changes for the period 2031-2060 for RCP8p5 for long-term average 7-day minimum (3.1) and annual mean flow (3.2). Decreases in low flows are projected for the rivers in Southern Europe; the Tanaro and Ebro. Decreases in summer precipitation and increases in evaporation caused by rising temperatures decrease the low flow. For the Glomma and Ångermanälven in Scandinavia all model combinations project increases of the base flow. Increasing temperatures will lead to earlier snow melt, snow accumulation and melt processes currently highly influences the annual hydrological cycle. Precipitation amounts will increase for Northern Europe leading to higher base flows. For the other rivers the signal is less pronounced. The changes projected for mean discharge are still relatively consistent between the models, yet smaller than the changes projected for low flows. For the Ångermanälven, Glomma and Oder average flow is projected to increase. For the Ebro and Tanaro decreases in mean discharge are most likely. For the other rivers the change signal is small and less consistent.

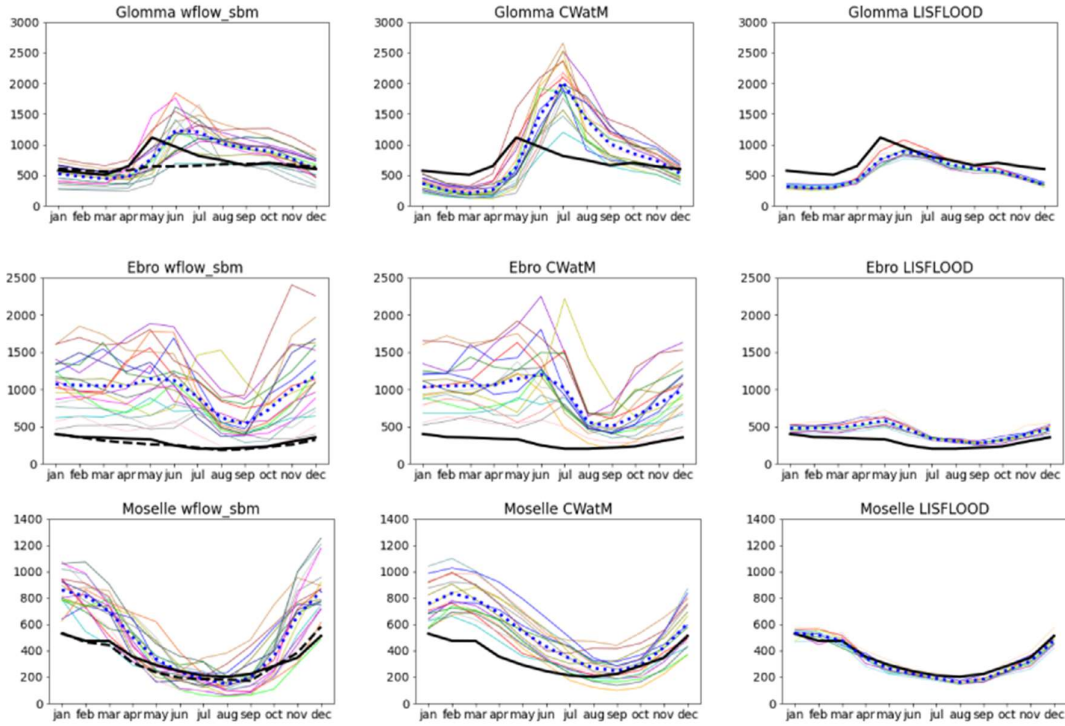


Figure 3.8.2: Historical discharge regimes ( $m^3 s^{-1}$ ) calculated over the period 1981-2010 from the CORDEX simulations (colored lines), the ensemble mean (blue dotted line) with from left to right (wflow\_sbm, CWatM and LISFLOOD), observed discharge (black) and reference wflow\_sbm run based on EObs (dashed black). To refer to the CORDEX realizations the same color coding is used in all graphs.

Table 3.8.2: Projected change in long-term average 7-day minimum low flow between the periods 1981-2010 and 2031-2060.

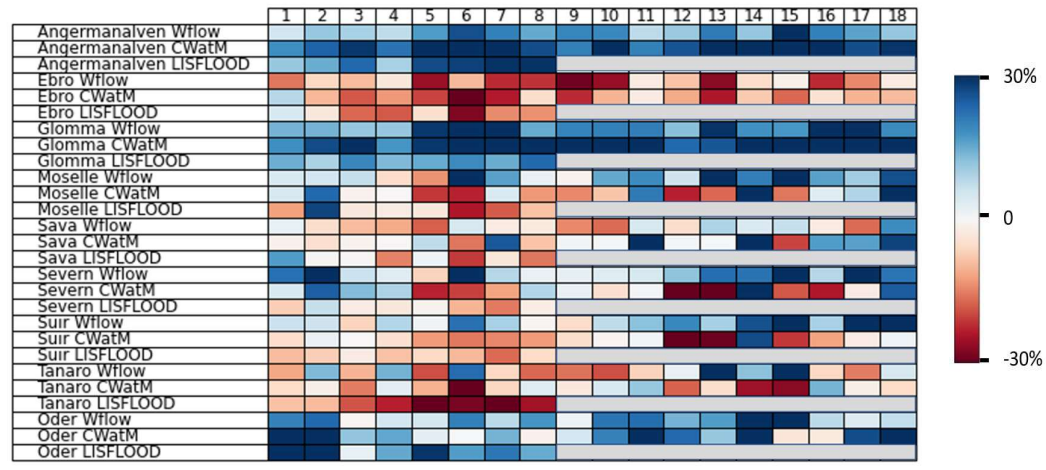


Table 3.8.3: Projected change in long-term average annual mean flow between the periods 1981-2010 and 2031-2060.

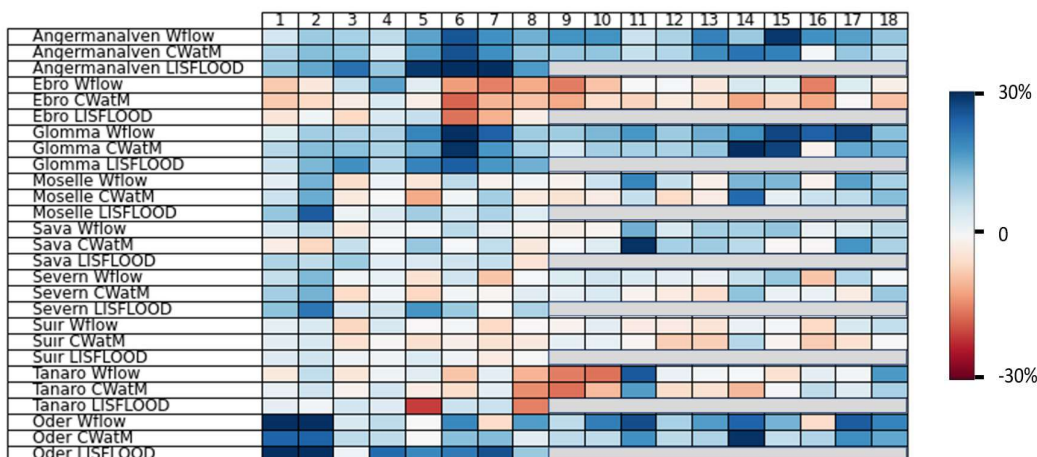


Figure 3.8.3 presents the resulting weighted changes in 7-day minimum, mean and annual maximum discharge together with the overall ensemble mean changes and the ensemble mean change from all wflow\_sbm and CWatM realizations. For most rivers the changes projected by (1) the full non-weighted ensemble, (2) the ClimWIP weighted ensemble are of the same order of magnitude. The REA method results in deviating changes. The main cause for this is the large climate model bias for the historical period. All realizations are biased, and REA assigns high weights to the least biased historical realizations. The results of the ClimWIP method are more promising.

The difference between the unweighted ensemble change and the change projected with the ClimWIP weighting method do not differ that much. While with the ClimWIP method 2 out of 6 models are assigned only a weight of ~5% and one model clearly dominates the rest (ICHEC-ECEARTH). This indicates that this model, that performs best compared to the other 5 GCMs when evaluated on large scale climate variables, also provides basin scale discharge projections that are in line with the projections obtained when the full ensemble is considered.

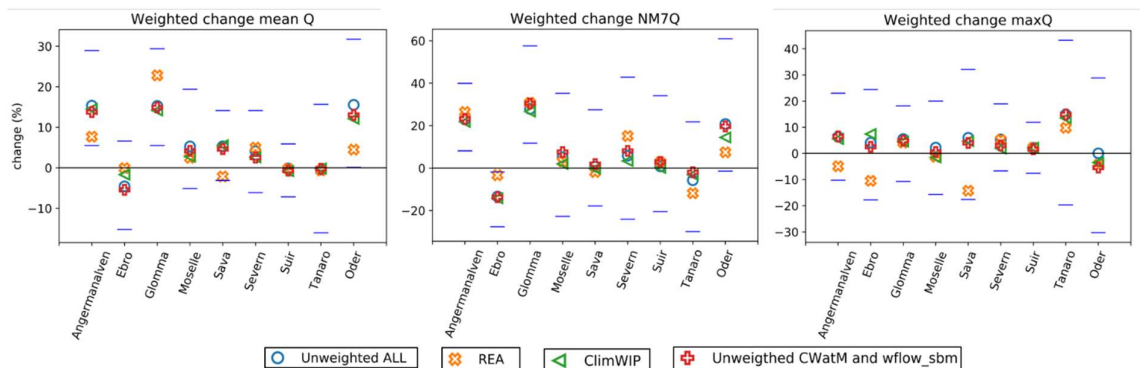


Figure 3.8.3: Projected future changes in annual mean discharge based on the full set of realizations - Unweighted ALL (blue), the Reliability Ensemble Averaging method – REA (orange), the realizations available for CWatM and LISFLOOD – Unweighted CWatM, wflow\_sbm (green) and ClimWIP (red) for the nine selected river basins. Together with the 5 and 95% uncertainty bounds of the full ensemble (blue dash).

### 3.8.4 Lessons learned

In line with existing work, the future projections indicate likely discharge decreases for the rivers in Southern Europe whereas increases are more likely for basins in Northern Europe. The large set of hydrological CORDEX based simulations we had available for three different hydrological models allowed to draw additional conclusions. The influence of the hydrological model, its calibration and the application of bias-correction on projected discharge changes showed to be limited in basins with a strong climate change signal. Yet, in central Europe where the changes are more variable the different model chains result in variable projections.

The consistency in the projected 7-day minimum flow statistic is highest in Southern basins. Projected changes in maximum flow are highly variable. There is clearly an uncertainty in projected maximum flow, caused by the large uncertainties in climate model precipitation. In addition, the 30-year time periods are too short to provide a representative set of annual maxima. Finally, estimates of peak flows are model dependent and rather sensitive to different hydrological routing and model parameterizations.

From the comparison between weighting methods it can be concluded that weighting climate models based on large scale climate patterns is more reliable than weighting on basin specific discharges. The REA method resulted in this study in very mixed and sometimes deviating change projections. However, both the REA and ClimWIP method favored simulations with ICHEC-EC-EARTH for at least part of the basins. The fact that a consistent change signal is obtained when either the full non-weighted ensemble or a weighted change where a single model dominates the change signal is used, increases confidence in the projections.

Finally, some uncertainties and biases in the change signal cannot be resolved by applying bias correction or post-processing weighting techniques. There remains a need for both improved historical meteorological data for bias-correction and climate model parameterization.

## 3.9 Ensemble hydrological impact simulations and projections under different forcing

### 3.9.1 Brief introduction to the case

The distribution of surface water and the availability of groundwater resources is not just determined by climatic and hydrological processes, but also heavily impacted by human water use and interventions. Considering an ever-growing population, leading to increasing food, energy and production demands relying on sufficient water resources, results in widespread impacts on the supply of water. By additionally considering potential water shortages (or excess) arising from recent and anticipated climate change, a reliable water supply is largely at risk in regions with large water demand as well as regions likely to experience drying climatic conditions. Under these conditions, water demand is often met through water extractions at the expense of environmental flows and water-dependent ecosystems or through increasing abstraction of non-renewable groundwater resources. The nexus of water-climate-human interactions calls for more holistic approaches considering both climatic and socio-economic pressures to assess their distinct as well as combined impact on the availability and accessibility of water resources, and on the occurrence and intensity of hydrological extremes, such as floods and droughts.

Within EUCP, IIASA developed a new large-scale hydrological rainfall-runoff and channel routing model that can be used to assess large-scale changes in hydrological conditions in a changing world, while considering the impact of human interventions: the Community Water Model (CwatM, Burek et al., 2020). CwatM is the newest model in the slowly growing range of global hydrological models. In comparison to more traditional, catchment-scale hydrological models, these models are designed at grid cell level and can be used to assess large-scale historic and projected changes in hydrological characteristics and water resources forced by either observations-based (such as, e.g., reanalysis data) as well as projected climate model data. Within EUCP, CWatM was utilized on a 5' (ca. 9x9km) spatial and daily temporal resolution across Europe. Using data provided by EUCP partner KNMI and in collaboration with Deltares, CWatM was forced by two sets of high-resolution regional climate model datasets widely used and partly generated within EUCP: (i) an ensemble of 20 regional historical and future climate simulations based on different regional climate models subject to a set of global climate models determining the associated boundary conditions, as well as (ii) pseudo-global warming (PGW) experiments using a regional climate model in a European domain subject to reanalysis-based boundary conditions under (a) reference and (b) 2K-global warming conditions. The set of experiments enabled the assessment of impacts of historical and projected water demand on hydrological extremes compared to natural conditions, as well as the potential impact of historical water use under conditions of 2deg global warming. Please refer to the EUCP deliverable 4.2 for more information

Based on the ensemble approach and the unique application of PGW simulations in hydrological impact simulations, the focus of IIASA's collaborative work within EUCP was to find new means in how to represent uncertainty quantitatively in a way that is both scientifically correct and meaningful to the diverse users, such that it can be implemented into participatory assessments of water-related climate risks and adaptation strategies. As projected increases in mean water scarcity pose significant challenges to societies, economies, and ecosystems within Europe and globally, IIASA further led a study highlighting that required adaptation and water management actions need to be implemented under conditions of large uncertainties and structural and governmental challenges, calling for a widespread and immediate transition and/or transformation towards a sustainable use of available water resources (Greve et al., 2018).

### 3.9.2 Methods

The hydrological model CWatM has been used to provide historical simulations and projections of streamflow across a European domain (see Fig. 3.9.1) covering most of European major rivers. However, some of the major eastern European river basins (e.g., the Volga river) are not entirely covered by the domain of the applied forcing data and are exempt from this analysis (see Fig. 3.9.1). Next to analyses at the grid cell level, we further focus on a set of medium-size river basins from the European HydroBASINS dataset (Lehner et al., 2013) to investigate impacts at the basin scale. We selected 134 independent basins ranging between 5.000km<sup>2</sup> and 30.000km<sup>2</sup>. Hydrological extremes are here assessed in terms of annual peak daily discharge and annual peak (lowest) daily low flow. We further assess low and high flows defined as the 5<sup>th</sup> and 95<sup>th</sup> percentile of the daily discharge distribution of all years (Fig. 3.9.4). However, as a sufficient supply of water is often most critical under low flow conditions, we particularly focus on the lower tail of the distribution of daily discharge and additionally include estimates at the 1<sup>st</sup> percentile when assessing the PGW experiments.

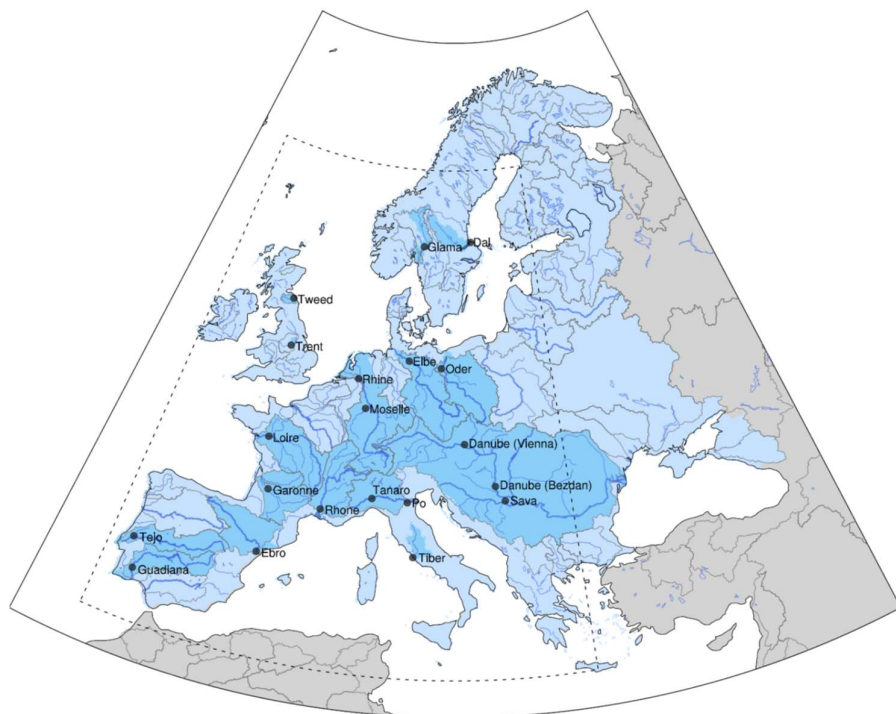


Figure 3.9.1: Major basins (light blue) within the EU-Cordex domain. Please note that major eastern Europe basins are not fully within the domain of the EU-Cordex forcing data and are excluded from the modelling setup. The domain indicated by dashed lines correspond to a smaller domain used for the PGW experiments. A set of 20 gauging stations (position as indicated by grey dots) within medium to large basins (dark blue) across Europe is chosen to illustrate impacts at catchment level in more detail.

#### MODEL

CWatM is a hydrological rainfall-runoff and channel routing model developed at IIASA (Burek et al., 2020). It is process-based and used to quantify water availability, human water use and the effects of water infrastructure, including reservoirs, groundwater, and irrigation. CWatM is designed at grid level, with two native versions for 0.5° and 5' resolutions at global scales (with sub-grid resolution taking topography and land cover into account). However, given different input data, the model can be set up at any resolution ranging from kilometer-scales up to coarse climate-model specific

resolutions. As forcing data, the model requires daily estimates of precipitation, as well as surface air temperature, wind speed, relative humidity, incoming long- and shortwave radiation, and surface air pressure as inputs to calculate potential evaporation. These variables are among the standard output of state-of-the-art Earth system and climate models, as well as observation-based forcing and reanalysis datasets. In comparison to the substantial number of highly specialized and parameterized catchment-based models, gridded, large-scale hydrological models such as CWatM still remain a niche within the hydrological community. Promoting the use of these models and increasing their accessibility has been the main motivation for the development of CWatM, as the model aims to overcome this barrier by implementing an open-source, modular modeling approach covering regional to global scales. The source code is available at Zenodo and Github (<https://github.com/CWatM>). All simulations are generated here using a calibrated version of CWatM. The model has been calibrated against 363 discharge time series from gauging stations across Europe. In comparison to observed discharge, CWatM shows slight biases within the range of +/- 20% in mean discharge, as well as in the 5<sup>th</sup> and 95<sup>th</sup> percentile (low and high flows) in the majority of basins

#### **FORCING DATA**

A 20-member multi-model ensemble of EURO-CORDEX regional climate simulations covering the period from 1961 to 2100 at 0.11° spatial resolution has been used. We use daily output of the required forcing variables within this period to force CWatM. The European-Coordinated Downscaling Experiment (EURO-CORDEX, Jacob et al., 2020), as part of the World Climate Research Program (WCRP) CORDEX initiative, coordinates the regional climate modelling activities of various research groups and institutes. The regional climate models are itself forced by a set of global climate models from the Coupled Model Intercomparison Project 5 (CMIP5, see Table 3.9.1). The period from 1961 to 2005 thus corresponds to the historical period of the associated CMIP5 data. From 2006 to 2100, CMIP5 simulations are based on the high climate change scenario under the Representative Concentration Pathway 8.5 (RCP8.5).

Further, a set of pseudo-global warming experiments (Prein et al., 2017; Brogli et al., 2019) covering the period from 1979-2010 provided by the EUCP partner KNMI and generated and used within WP2 have been used. These simulations are based on the RACMO regional climate model (that is also part of the EURO-CORDEX ensemble) at 0.11° spatial resolution covering a smaller subdomain of the EURO-CORDEX domain (see Fig. 3.9.1). In the reference experiment (i) RACMO is forced by unperturbed ERA5 reanalysis data, while in the pseudo-global warming experiment (ii) the forcing data consist of perturbed reanalysis data. Perturbations added to ERA5 correspond to climate change patterns retrieved from a 16-member ensemble of EC-EARTH (a CMIP5 climate model) global climate simulations under conditions of 2K global warming. By construction the two forcing data sets are primarily different in their thermodynamics consistent with 2K global warming (higher temperatures in the perturbed forcing data; enhanced stratification of mean temperature vertical profiles; larger atmospheric vapour contents corresponding to the higher temperatures, but generally slightly lower relative humidity), while they are quite similar in their day-to-day large-scale circulation as enforced by ERA5.

**EXPERIMENTAL DESIGN**

To enable a thorough impact assessment concerning water use and associated uncertainties, CWatM is used (i) under pristine, natural conditions with no representation of water demand, and (ii) under conditions considering water demand from the agricultural, industrial, and household sector, and considering (a) historical conditions, and (b) projected climate changed conditions. Thus, for both the EURO-CORDEX ensemble and the KNMI-PGW data, a set of four experiments is generated (see Table 3.9.1). Additionally, when using the PGW forcing, we perform simulations by adjusting historical water withdrawals to different relative levels under PGW conditions (ranging between +/- 50% of historic water withdrawals), thereby providing an ad hoc representation of multiple, potential future water management scenarios. That enables us to directly identify the sensitivity of projected changes in average discharge conditions against relative changes in water withdrawals (in terms of historical water withdrawals). Assessing average and low flow sensitivities further provides insights into adaptation and mitigation potentials under water scarcity and drought conditions, guiding the design of efficient, sustainable, and robust water management interventions.

Experiment	Climate change	Water demand
nat-ref	-	-
dem-ref	-	+
nat-fut	+	-
dem-fut	+	+

**3.9.3 Results**

**EURO-CORDEX FORCING**

Based on the full EURO-CORDEX ensemble provided as forcing to CWatM, mean daily discharge tops well above 1000m<sup>3</sup>/s in most of the major European river basins, with highest discharge values reached in the Danube basin. Average annual daily peak low flows and low flows (5<sup>th</sup> percentile) are considerably smaller, with few southern European basins at risk to run completely dry under conditions of prolonged drought. Nonetheless, peak discharge in all major basins across Europe reaches values well above 1000m<sup>3</sup>/s.

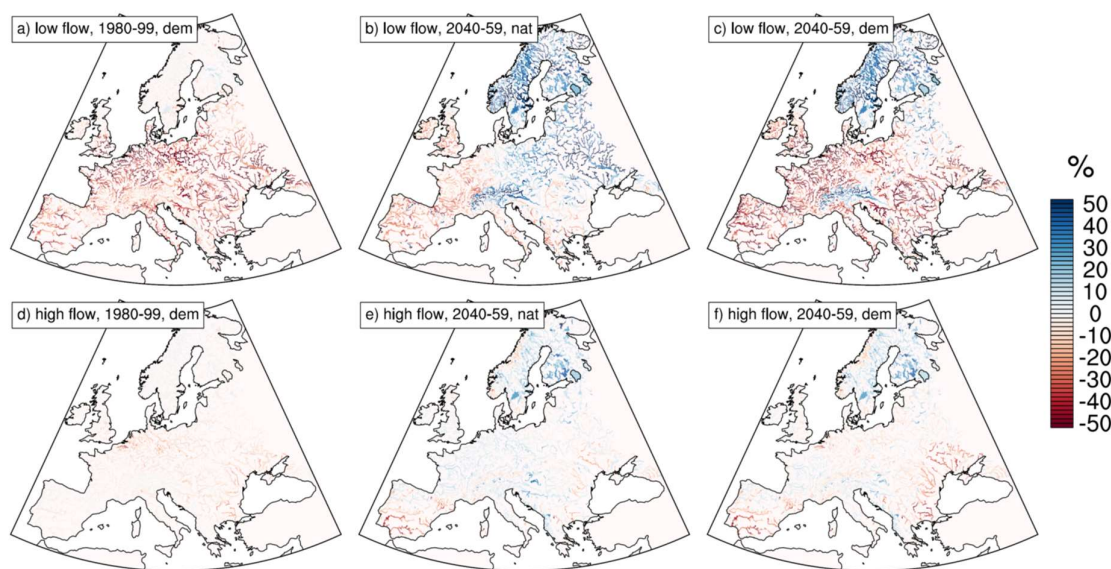


Figure 3.9.2: Relative difference (in percent) in ensemble-average annual low flows (upper row) and high flows (bottom row) between nat-ref and (a,d) dem-ref in the historic period (1980-99), (b,e) nat-fut in the future period (2040-59), and (c,f) dem-fut in the future period (2040-59). The left column (a,d) illustrates the impact from human water use on low/high flows, whereas the middle column (b,e) illustrates the climate change impact. The combined impact is shown in the right column.

Comparing low and high flows under pristine, natural conditions (nat-ref) to the other experiments, reveals several important insights on the impact of human water use and climate change on hydrological extremes across Europe (see Fig. 3.9.2). Under dem-ref, i.e., by adding human water use, considerable decreases in low flows are found across southern and central Europe, with largest decreases in most of the heavily managed central European basins. For low flows under nat-fut, i.e., by adding a climate change response, the common pattern of decreases in southern Europe vs. increases in northern Europe is evident. The combined response in low flows (dem-fut) shows an amplified drying in most parts of southern and central Europe (due to decreases in dem-ref plus drying in nat-fut). Increasing low flows in the combined response are only found in Scandinavia and the Alps. High flows under dem-ref only shows no to small negative changes. The relative climate response in high flows (nat-fut) is also weaker in comparison to the response in low flows (even though absolute values might still be considerable).

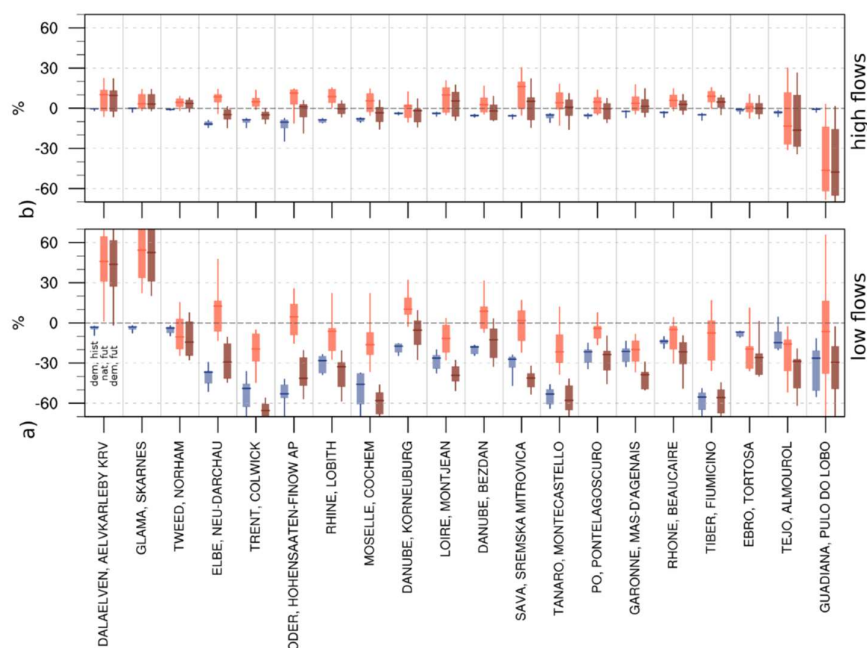


Figure 3.9.3: Relative difference (in percent) in average annual a) low flows, and b) high flows for the full set of EU-Cordex forcing models in the selected basins. Differences relative to nat-ref are estimated for nat-dem in the historic period (blue, 1980-99), nat-fut in the future period (light red, 2040-59), and dem-fut in the future period (dark red, 2040-59). The boxes (horizontal lines) indicate the interquartile (full) range of relative differences from the set EU-Cordex forcing models. The center line in each box denotes the median response.

Considering the selected basins (see Fig. 3.9.1) enables a more detailed assessment of differences between the experiments and a closer look at the associated uncertainties. Fig. 3.9.3 highlights the uncertainty originating from the 20-member EURO-CORDEX ensemble. Regarding low flows, the (near-natural) Scandinavian catchments (Dalaelven, Glama) show significant increases due to climate change, while human water use only results in small decreases by an order of magnitude less. For most central European basins, the water use impact is substantially larger and dominates the combined response. These basins are subject to substantial water withdrawals and water consumption (Fig. 3.9.3), especially resulting in widespread impacts during the driest period of the year. Since central Europe is located in between wetting signals in Scandinavia and drying signals in the Mediterranean, the climate change response is relatively weak. The impact on high flows is, again, considerably smaller, only ranging between +/- 10% for most European basins.

**PGW FORCING**

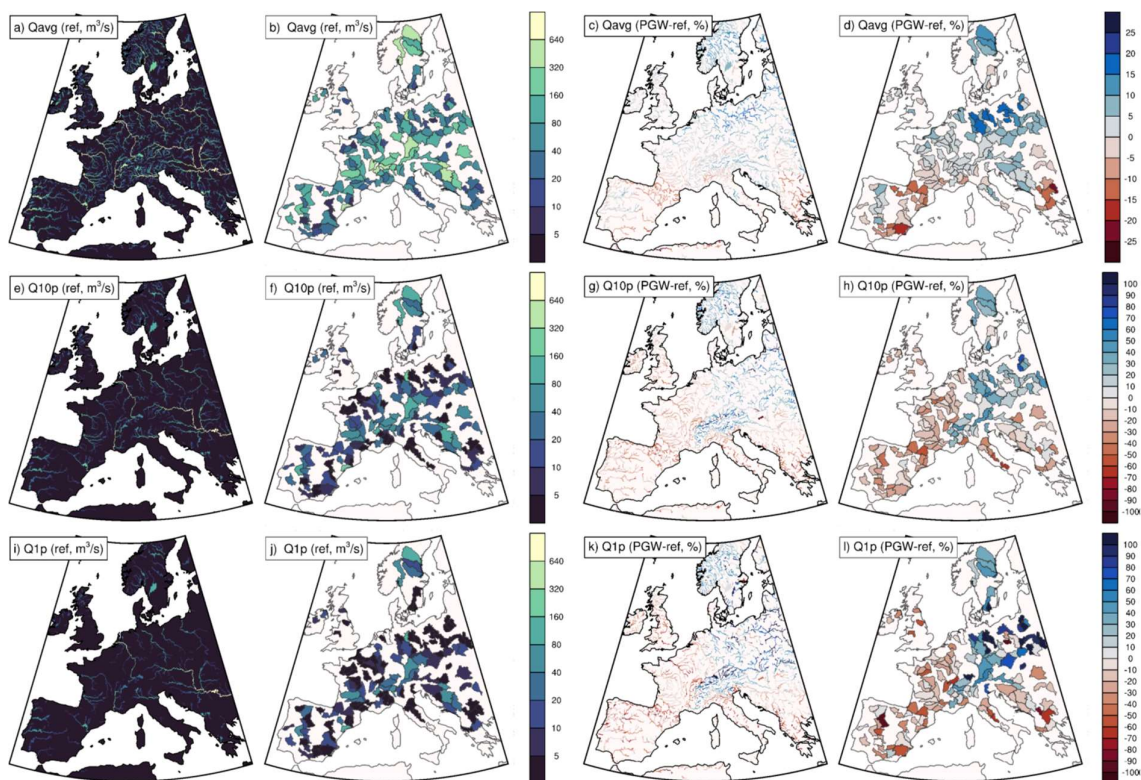


Figure 3.9.4: Mean discharge and low flows under reference conditions at grid scale (1st column) and at basin scale (2nd column). Relative differences in mean discharge and low flows between PGW and reference conditions at grid scale (3rd column) and at basin scale (4th column). Please note the difference in scaling between average discharge (top row) and low flows (2nd, 3rd row). Grid cells and basins with average discharge < 10 m<sup>3</sup>/s are not shown in columns 2, 3, and 4.

Simulated differences between reference and PGW conditions resemble the well-known pattern of southern European drying and northern European wetting (see Fig. 3.9.4). That signal is evident in both average and low flow statistics. However, the high-resolution modeling approach used here reveals significant regional differences. For example, while declines in average discharge are found in most regions and basins surrounding the Mediterranean Sea, some southern European regions do not show distinct decreases under conditions of 2K global warming. These are primarily regions in mountainous northwestern Spain, as well as basins surrounding the northern Adriatic Sea. Increases in average discharge are primarily found within the northeastern parts of the study domain and, to a lesser extent, in mountainous regions across Europe (e.g., the Alps). Most western and central European regions only show small relative differences in mean discharge (+/-10%). In contrast to mean discharge, the total extent of regions and basins showing declines in low flow conditions is considerably larger, extending into various parts of western and southeastern Europe. Decreases in Q10p and Q1p are particularly large in basins surrounding the Mediterranean Sea but are also apparent in France, Benelux, and the British Isles. Increasing low flows are located in Alpine regions and the northeastern parts of the study domain.

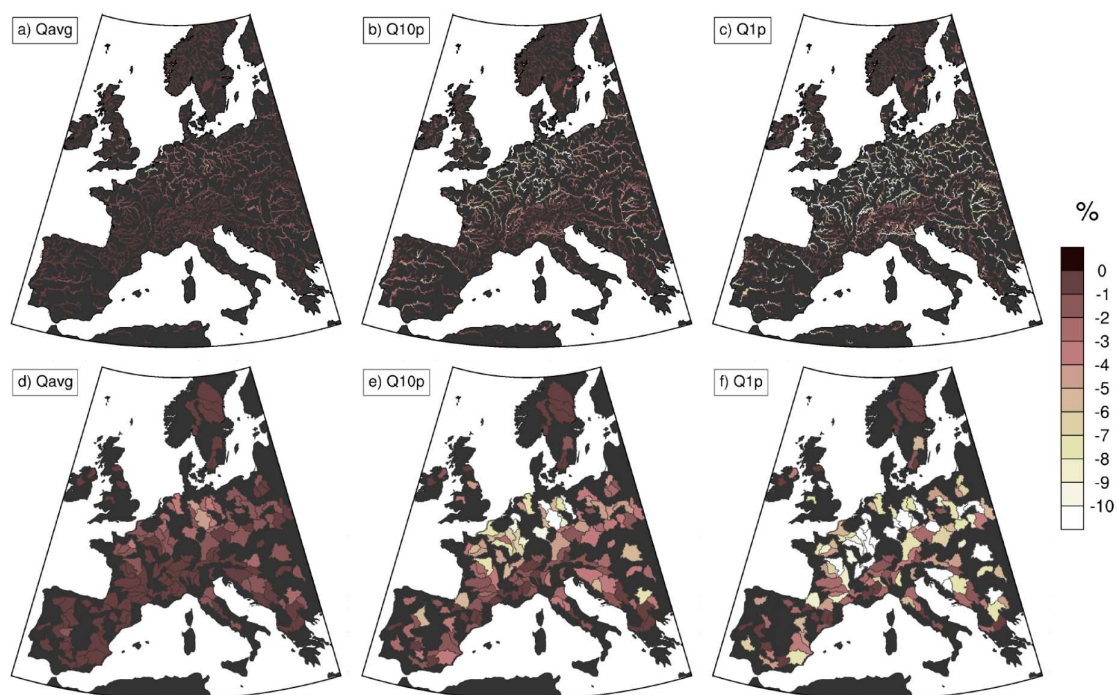


Figure 3.9.5: Sensitivity of mean discharge and low flows under PGW conditions to relative changes in water withdrawals at grid scale (1st row) and at basin scale (2nd row). The scale shows relative declines in (left column) average discharge (middle) Q10p, and (right) Q1p corresponding to a 10% increase in water withdrawals. Grid cells and basins with average discharge < 10 m<sup>3</sup>/s are not shown (dark gray).

The storyline-based experimental adjustment of historic water withdrawals under PGW conditions enables an assessment of the sensitivity of average discharge and low flows to changing water withdrawals. We have here performed 11 hydrological simulations ad-hoc adjusting water withdrawals between 50% and 150% of historic water withdrawals. That range represents differences that can occur when applying different scenarios of future water withdrawals across developed regions, such as Europe. In fact, across Southern Europe, even increases in water withdrawals beyond 150% can occur under more pessimistic scenarios, while decreases in water withdrawals might occur across Central Europe under more optimistic scenarios. Relative adjustments in domestic and industrial water withdrawals are realized by applying the percentage difference. Irrigation demand depends on available soil water and is potentially different under PGW conditions. However, to enable a direct comparison to adjusted domestic and industrial withdrawals, we also apply the percentage difference in relation to irrigation withdrawals under reference conditions.

The relative sensitivity to increasing water withdrawals is regionally different (see Fig. 3.9.5), and, to a large extent, depends on the amount of upstream water withdrawals. Low flow sensitivities are thus highest in regions with large (upstream) water withdrawals (e.g., Central Europe) and can reach up to parity resulting in decreases of 10% in low flows per 10% increase in water withdrawals. Such high sensitivities are primarily located in upstream areas of Central European rivers (e.g., Rhine, Meuse, Seine) in France, Benelux, and Germany. Relative sensitivities in average discharge are, however, relatively small in comparison to low flow sensitivities. The response to varying levels of water withdrawals (within the range of +/- 50% of historic water withdrawals) further exceeds the climate change response of 2K global warming in average and low flows across many parts of Central and Western Europe. Hence, assuming increases in water withdrawals of 50% or less can regionally double the climate-only response. If differences of this magnitude also exist between water use scenarios,

identified changes in low flow conditions can either be neutralized or amplified, thereby increasing uncertainties and hindering robust water management assessments. On a second note, high sensitivities to water withdrawals also provide the potential to manage climate-driven decreases in low flows. Within the identified regions across Central and Western Europe, reduced future water withdrawals of up to 50% can potentially preserve current low flow conditions also under conditions or reduced flows due to 2K global warming.

### 3.9.4 Lessons learned

Within EUCP, IIASA developed a large-scale hydrological and water resources model that can be used in climate change impact assessment at regional to global scales. By using high-resolution climate forcing data, impacts on hydrological extremes under water use and climate change conditions have been assessed.

Based on different modelling experiments, climate and water demand impacts on low/high flows have been singled out and assessed across Europe. In comparison to previous research excluding water demand estimates, the research presented in this report illustrates the significant impact of human water use particularly on low flows. It has been argued before (van Loon et al., 2016), that hydrological droughts are in parts driven by human influences on rivers and streams. The findings presented here largely support this statement and urge for a more comprehensive assessment of current and future risks and losses due to hydrological extremes by accounting for both climate and socio-economic change.

The presented results further highlight the Mediterranean region as a hotspot of climate change. It is likely that future climatic conditions will decrease flows in both the driest and wettest periods of the year. Low flows in dry periods will decrease substantially, thereby not just threatening domestic, agricultural and industrial water supplies, but also environmental flows and water-dependent ecosystems. While the impact of changing water withdrawals on relative changes in projected mean discharge is limited, the results also show that projected low flows are sensitive to differing water withdrawals under conditions of 2K global warming. However, while several studies solely investigated the climate change impact on low flows, our results provide a coupled analysis of conditions under 2K global warming and their sensitivity to different, idealized water use scenarios. We show that even minor changes in water withdrawals can lead to differences in projected low flows that exceed the climate change response throughout Central and Western Europe - mainly due to large sensitivities and a relatively small climate change response. That particularly highlights that quantitative assessments of low flows under future warming are impacted by changing future water withdrawals across highly populated and industrialized regions. Therefore, including water withdrawals in hydrological impact assessments is of utmost importance to communicate the associated broad range of uncertainties. Assessments of climate change impacts in near-natural catchments provide only part of the anticipated response and do not necessarily reflect changes experienced within heavily managed river basins, where climate change assessments for adaptation are needed most. Our storyline-based results also highlight new ways to communicate how to manage climate change impacts on river flow, especially within the most critical periods of the year. Regions of substantial low flow sensitivity to water withdrawals will benefit most from coordinated efforts to reduce water withdrawals at regional, national and transnational scales.

## 3.10 Pluvial flood hazard and risk, and risk reduction measures – city of Milan

### 3.10.1 Brief introduction to case

Flood risk is accountable for the largest economic losses in Europe and in Italy, and is responsible for damage exceeding 158 and 38 billion Euros respectively over the period 1980-2020 (Mysiak et al., 2022). Whereas floods caused by high river stages and storm surges have been addressed via the hazard mapping and assessment mandated by the Floods Directive (2007/60/EC), the hazard arising from spontaneous overland runoff from extreme precipitation events in urban context received lower attention. Pluvial floods occur when rainwater is not absorbed by ground or urban drainage systems. Intense and spatially concentrated precipitation events in densely developed urban areas can result in excessive water flow which can cause sizeable damage to tangible assets. The projected climate change in Europe is expected to increase the intensity and frequency of extreme rainfalls, which in combination with the continuing land conversion and urban expansion will lead to higher pluvial flood risks and expected damage and loss. It is important therefore to design adequate financial protection and risk mitigation strategies such as sustainable urban drainage (SUDS).

Here we explore pluvial hazard risk and risk-mitigation measures over the city of Milan in northern Italy. The metropolitan area of Milan is the second largest in Italy, home to 3.3 million residents. The Milan City Council declared a climate and environmental emergency in May 2019, a year before the national government did. Milan is member of the Covenant of Mayors for Climate and Energy, C40 Cities Climate Leadership Group, the Resilient Cities Network. The city's Resilient Cities office is a part of the Green Transition Department. This department coordinates the Air and Climate Plan (ACP) and the Climate Risk Assessment. The latter identified heat and flood risks as the city's main climate-related perils. The ACP is integrated within the City Masterplan and the Resilience strategy. The city's climate risk assessment was conducted at the census scale and identified areas at risk, based on social (high density in housing, vulnerable population, presence of unemployed population groups, etc.), economic and environmental conditions.

Hydraulic modelling in complex urban environments characterised by high degree of impermeable soil and presence of drainage/sewage network are associated with high costs. Here we use a simplified and computationally efficient raster-based model based on a hierarchical filling and spilling algorithm. The same model has been used for the Copernicus Sectoral Information System (C3S) for pluvial flood risk assessment in 20 European cities, forced by dynamically downscaled climate reanalysis (Essenfelder et al., 2021). Building upon that work, we extended the analysis using the convection-permitting climate simulations produced in EUCP (WP3) and simulated the effects of the nature-based solutions, reducing the pluvial hazards and risk. Green Infrastructure (GI) (EEA, 2017) are defined as a strategically planned network of green and natural elements supporting a wide range of services and benefits to people (EC, 2013a). In urban environments, GI can be open green spaces, as parks and gardens, green roofs, green alleys, permeable pavements and vegetated buffers. These elements contribute to flood regulation increasing the soil capacity to retain and infiltrate water controlling the storm-water runoff and peak flow (EC, 2013b). To increase and maximise the flood regulation capacity of GI, they should be strategically distributed and connected across the city. Connectivity is considered a key pillar to maintain healthy and well-functioning ecosystems that can support ecological functions and delivery of services (Mitchell et al., 2013, 2015)

This methodology and results are further explained in **Staccione et al** (in preparation for submission) 'Connected urban green spaces for flood risk reduction in the Metropolitan area of Milan'.

### 3.10.2 Methods

**Climate forcing:** We used high resolution, convection-permitting climate simulations produced in WP3 over the ALP-3 domain. The simulations were forced EC-Earth model. We used RCP8.5 and performed the analysis for two future periods: from 2041 to 2050 and from 2090 to 2099. Probabilistic extreme hourly rainfall rates were estimated through statistical analysis of the annual maximum hourly precipitation rates. The Generalised Extreme Value (GEV) distribution was used to estimate maximum rainfall rates for probabilities ranging from 0.5 (return period RP 2 years) to 0.001 (RP 1000 years).

**Hazard model.** Pluvial flood hazard maps were generated for each rainfall probability using a simplified raster-based model based on a hierarchical filling and spilling algorithm (Samela et al., 2020). This fast-processing, hydrostatic model identifies inundated areas on the basis of high-resolution digital elevation model and is suitable for application over large urban areas. It accounts for spatially distributed rainfall input and infiltration, building upon pixel-based Green-Ampt model (Green and Ampt, 1911).

**Economic impact.** Direct tangible damages to urban buildings were estimated using stage-damage models (Huizinga et al., 2017) and reconstruction costs. Building footprints were retrieved from OpenStreetMaps (OSM, 2021) and classified as residential, commercial or industrial. Where the OSM did not indicate the specific use of the building, we used the classification from the Corine Land Cover 2018 dataset (CLC, 2018). Build-up areas not classified as residential, commercial, or industrial were not accounted for in this analysis (e.g. infrastructure or agriculture). Reconstruction costs per square metre are extracted from country-specific cadastral records. Direct tangible damage was estimated for every hazard probability and aggregated into Expected Annual Damages (EAD).

**Green infrastructure.** The existing green infrastructure (GI) network were extracted from the European Settlement Map of 2017, reclassified to 100m grid (Ferri et al., 2017). The cells with more than 25% green cover were included in the network. We performed morphological spatial pattern analysis (Soille and Vogt, 2009; Vogt et al., 2009) to identify core areas and connectors. We estimated landscape connectivity index (Integrate Index of Connectivity, IIC) (Pascual-Hortal and Saura, 2006). IIC is used to rank the core areas based on their contribution to the overall connectivity of the network. As next, we identified areas that simultaneously contribute to improving the connectivity of the GI network as well help to reduce the pluvial flood hazard. For this end, we used walking distance (5 to 10 mins) from existing green areas. This respond to the goal of the Milan city administration to improve accessibility to green spaces (EEA, 2020). The identified areas were further assessed in terms of flood risk reduction and land use conversion potential. As next, we built 3 scenarios of green infrastructure's improvement: greening of buildings (GB), which consider the establishment of green roofs; greening spaces (GS), which include the conversion of open space to green spaces, and greening the city (GC), which include both green buildings and spaces. For each scenario, we investigated different degrees of green conversion: 25%, 50%, 75%, 100% of all suitable areas. We applied the following criteria to prioritise areas of interventions: cumulative water damage to buildings (Essenfelder et al., 2021), share of the existing open green space (Ferri et al., 2017), share of suitable areas for and potential impact of green roofs (Comune di Milano, 2016). The latter is defined as a function of sealed areas in the surrounding areas. We run pluvial hazard model for each scenario for a rain event of 54.68 mm in 1 hour, in accordance with the estimated depth-frequency values of extreme precipitation events in Essenfelder et al., 2021.

### 3.10.3 Results

Figure 3.10.1 shows the results of the statistical analysis performed to estimate the extreme hourly rainfall rates over the city of Milan under the different climate periods.

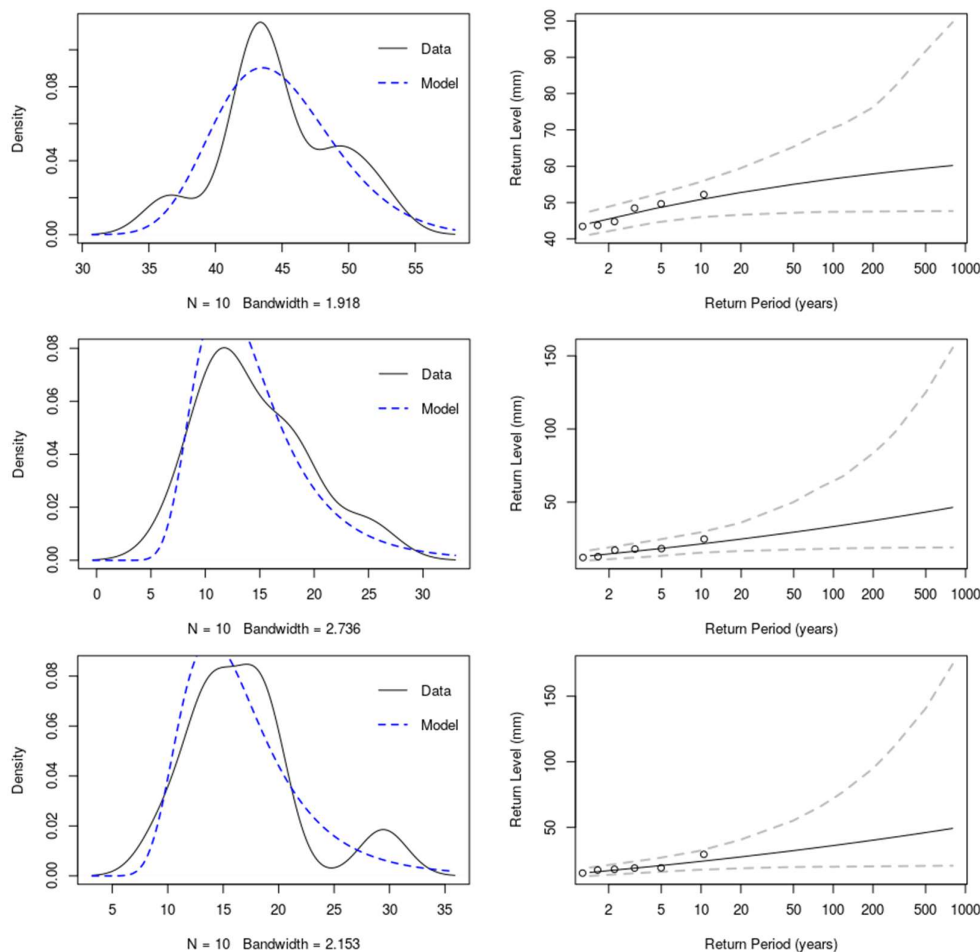


Figure 3.10.1: Statistical data analysis and fitting of a GEV distribution function for estimating extreme hourly rainfall rates (in mm/hour). On the left, the density plots of observations (black line) and modelled (blue line) data. On the right, the return period and estimated extreme hourly rainfall rates (in mm/hour). On the top row, the historical period. On the middle row, the RCP8.5 2041-2050 period. On the bottom row, the RCP8.5 2090-2099 period.

The fitting of a GEV distribution function to the annual hourly maxima rainfall rates allows for the computation of the return levels associated with a certain probability. The estimated resulting return levels for the extreme hourly rainfall rates (in mm/hour) are shown in Table 3.10.1.

Table 3.10.1: Extreme hourly rainfall rates (in mm/hour) for different return periods (RPs) estimated as a result of the extreme value analysis using a GEV distribution function.

RP (years)	2	5	10	20	50	75	100	200	250	500	1000
Historical - 1996-2005	44.3	48.4	50.7	52.7	55.0	55.9	56.5	57.9	58.3	59.5	60.5
RCP8.5 - 2041-2050	41.6	49.5	55.7	62.5	72.6	77.6	81.4	91.3	94.7	106.4	119.5
RCP8.5 - 2090-2099	39.4	55.3	71.2	92.3	132.0	155.3	174.6	232.4	255.1	342.0	460.1

We observe an increase in the intensity of extreme hourly rainfall rates throughout the 21st century. Accordingly, a 1-in-5 years event is expected to increase by 2.2% and 14.2% by the mid-century and late-century, respectively, while a 1-in-100 years event is expected to increase in intensity by 44.0% and 209.1%, respectively. The estimated EAD under the historical climate period for Milan is 744

million EUR, with the historical city centre (including train station area) being one of the most affected areas. As shown in Figure 3.10.3, the EAD from direct tangible damages are expected to increase by 1.36% (10.1 million EUR) and 9.49% (70.6 million EUR) by mid- and late-century, respectively.

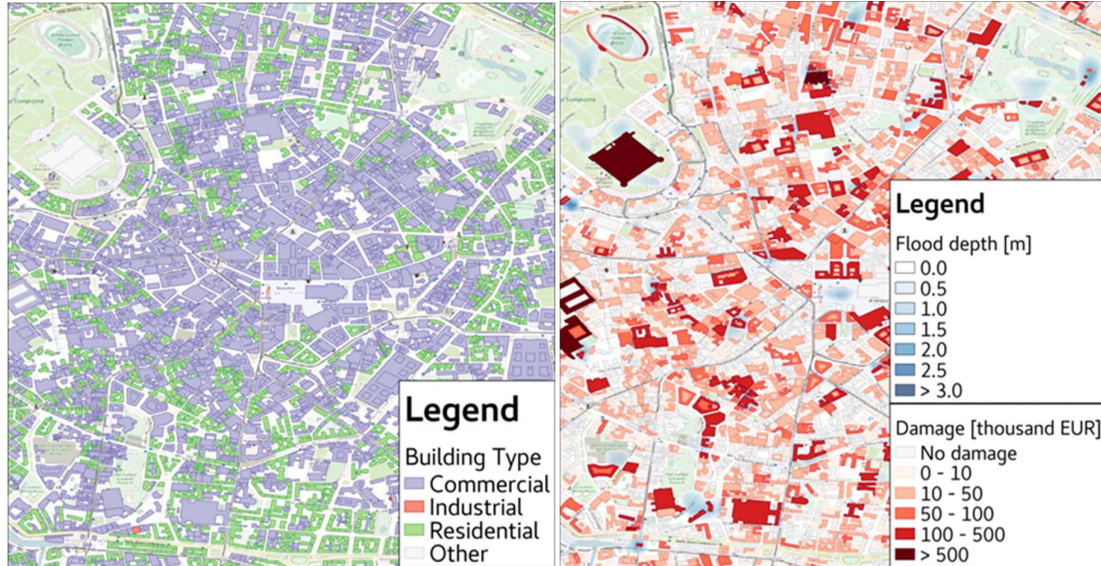


Figure 3.10.2: Pluvial flood damage analysis for the city of Milan (Italy). On the left, the building reclassification around the city centre. On the right, the estimated direct tangible damages per thousand EUR for an extreme rainfall event of RP of 1-100 years under the historical climate period.

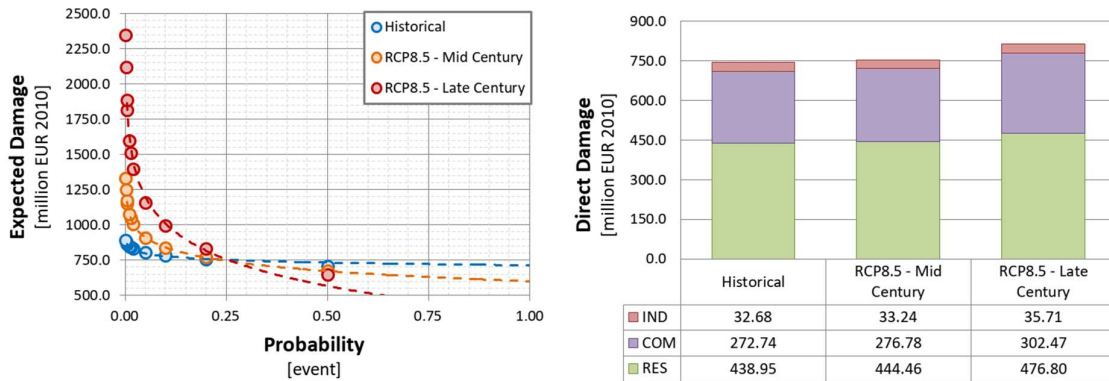


Figure 3.10.3: Expected direct tangible damages due to pluvial flooding in Milan under the historical, RCP 8.5 mid-century, and RCP 8.5 late-century climate scenarios. On the left, the expected damage – probability curve. On the right, the expected annual damage (EAD) for each climate scenario.

The existing GI network is shown in Figure 3.10.4. The many green areas of the city are concentrated in the peripheral zones of the city. Here, the network is well developed and connected. The inner part of the city, on the other hand, has few or no core green spaces (connectivity index IIC = 0.1).

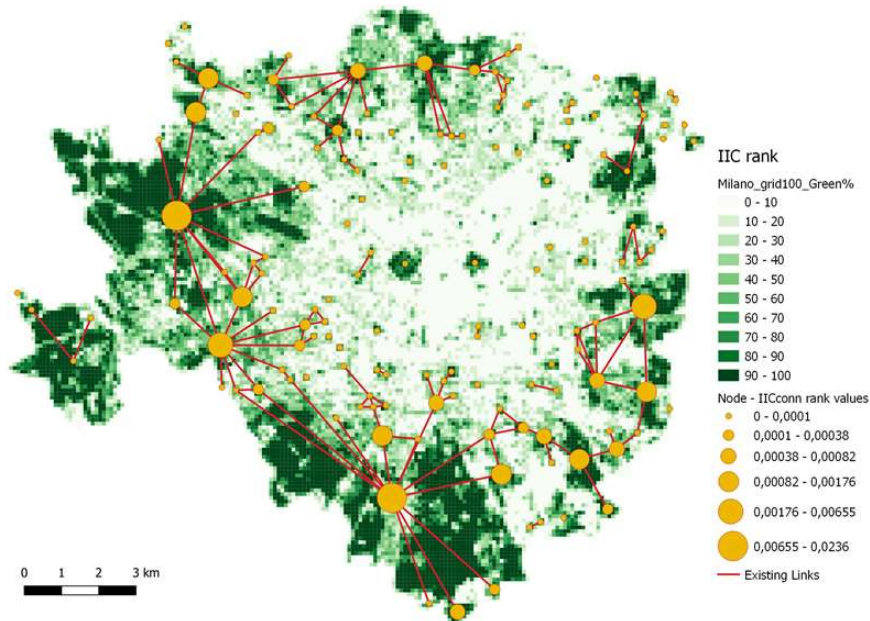


Figure 3.10.4: Existing GI Network in the City of Milan. The green grid represents the percentage cover of green areas per cell. The lines (connections) and dots (core areas) are the graphical representation of the network. The size of dots indicates the importance of the area to the overall connectivity of the network.

We identified around 6350 suitable cells with accessibility up to 5-10 minutes of walk. These are mainly located in the inner part of the city and respond to differently evaluation criteria (Figure 3.10.5). The cell contributing more to reducing flood damages are concentrated in the central and western part of the city. On the contrary, open space and roofs that are convertible to green areas are predominately located in the more peripheral areas. Green roofs are more suitable in central part of the city.

Figure 3.10.6 show the prioritisation of potential green areas for the scenario 'Green City (GC)' according to the percentage of green conversion. In the top 25% potential green areas, we can already notice a more connected distribution of green spaces throughout the centre of the city, creating green corridors among central and peripheral green areas. We can observe a reduction of expected damage to buildings in this scenario (of almost 6% for total buildings), which is increasing up to 10% with a complete conversion to green (Figure 3.10.7).

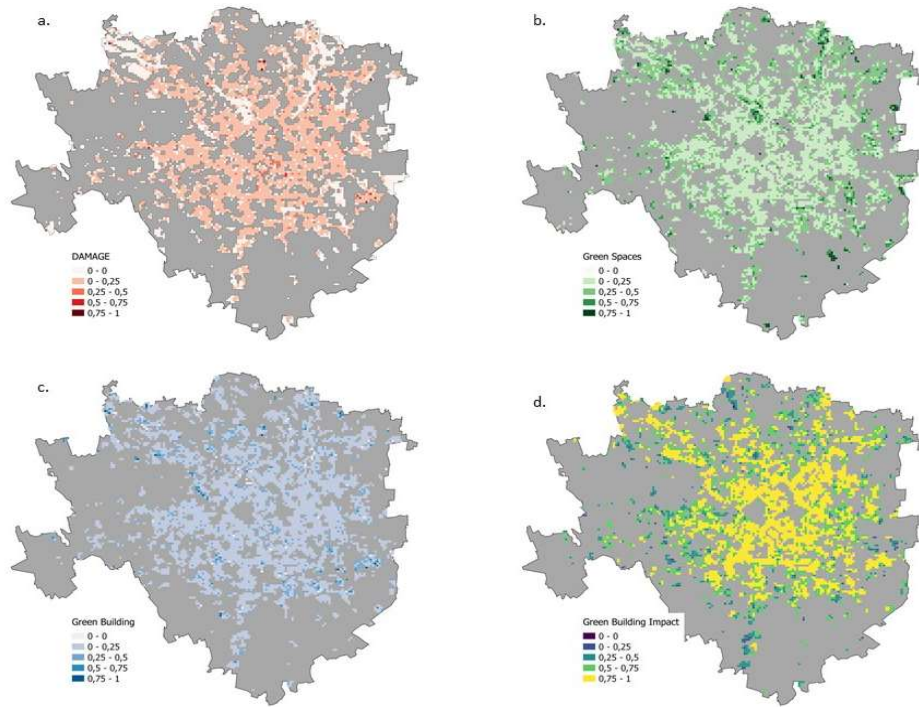


Figure 3.10.5: Cells representing the suitable areas to be converted to green areas. The different maps show the characterisation of each cell in terms of (a) cumulative damage to buildings, (b) percentage areas of open spaces that could be converted to green, (c) percentage area of potential green roofs, (d) impacts of potential green roofs.

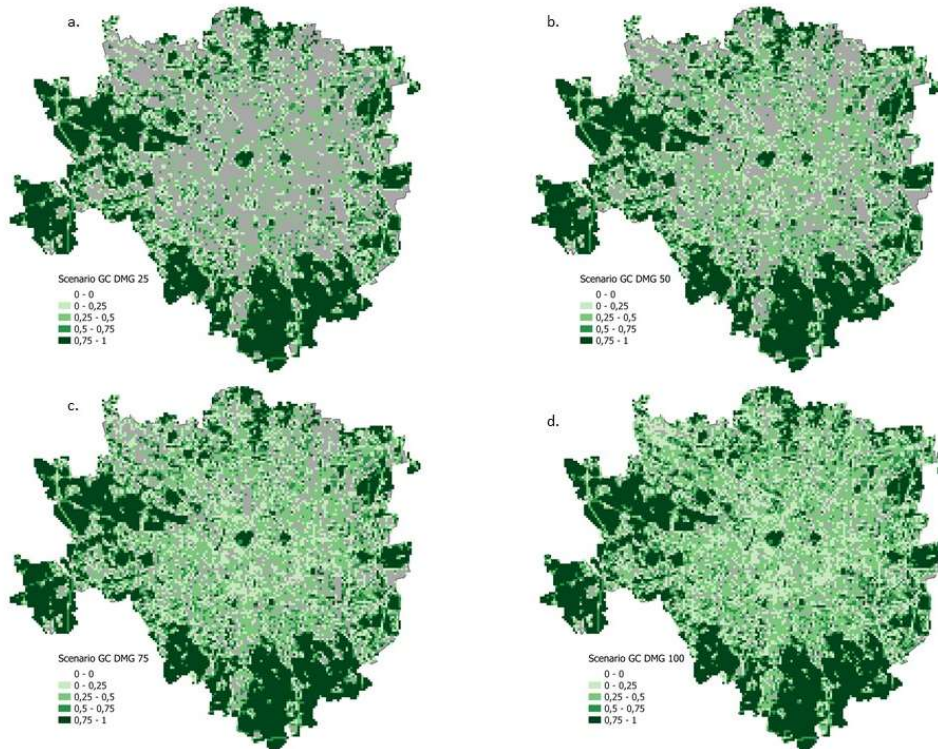


Figure 3.10.6: Green City scenarios. Each map shows the prioritised areas to be converted to green according to different percentage area of suitable areas (a-25%, b-50%, c-75%, d-100%). The shades of green represent the new permeability values attributed to the converted cells.

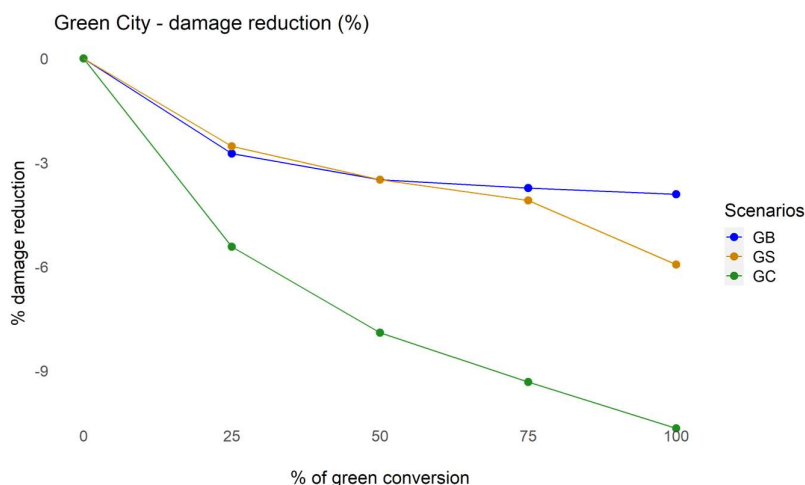


Figure 3.10.7: Percentage reduction of direct damage estimated for all buildings in the three scenarios (Green Buildings -GB, Green Spaces -GS and Green City -GC), compared to the current situation (zero value of conversion).

### 3.10.4 Lessons learned

Nature-based solutions can play an important role, or a part thereof, in disaster risk reduction, climate adaptation and biodiversity protection, urban and rural sustainable agendas, health & sustainable livelihood, and other policy areas. NbS can provide means to mitigating climate risks - in this case through water flow regulation. Compared to engineered, built or fossil-based solutions, NbS approaches may be cost-effective and have many ecological, social and economic benefits. NbS face sizeable challenges and barriers to adoption, which - depending on the contexts - may include poor adaptation to given socio-cultural situations, possible ecosystem disservices (von Döhren and Haase, 2015), absence of supportive governance and financial instruments to stimulate implementation, low social acceptance, limited business model innovation, and failure to account for the true social value of the generated benefits (Venkataraman et al., 2020).

For many stakeholders, the performance of NbS under extreme hazard conditions and their integrity in the face of climate change remains unclear. The unequal coverage and analytical depth of existing performance assessments resulted in relatively low investment in NbS by the private sector. A recent global study of NbS performance (Sudmeier-Rieux et al., 2021) evaluate methods, metrics, and data in terms of their strengths, weaknesses, and barriers to adoption for assessing risk reduction and co-benefits by NbS. The study found significant knowledge gaps in terms of economic benefits generated by NbS and their distribution.

In this work, we have demonstrated the usefulness of the EUCP convection-permitting climate simulations for the urban climate risk assessment and adaptation planning. This work builds upon and extends the C3S [Pluvial Flood Risk Assessment in Urban Areas](#) developed by CMCC and other partners. By using the EUCP climate simulation, we improved the existing pluvial hazard and risk assessment and demonstrated how NbS can mitigate the risk, while producing additional benefits in terms of temperature regulation, air quality improvement (by removal particle pollution), and protect soil and biodiversity. This study serves as a pilot for other cities across the ALP-3 EUCP domain. The open source/access modelling tools will be further exploited in a recent H2020 project REACHOUT<sup>2</sup> in which Milan city serves as a hub for other surrounding cities.

<sup>2</sup> [REACHOUT](#) - Resilience in Europe through activating city hubs reaching out to users with triple-a adaptation tools

## 3.11 Projected impacts of extreme sea level and benefit-cost assessment of adaptation measures along Upper Adriatic Sea coasts

### 3.11.1 Brief introduction to case

More than 700 million people all over the world live in low-lying coastal areas (McGranahan et al., 2007), and almost 100 million are exposed to a 100-year return period flood event (Muis et al., 2016). Coastal flood risk increases in many places around the globe due to development (Bouwer, 2011; Brenden Jongman et al., 2012) and land subsidence (Nicholls and Cazenave, 2010; Syvitski et al., 2009). The climate change induced sea level rise (SLR) has contributed to this trend and is likely to become the main driver of coastal inundation risk (Hallegatte et al., 2013; Hinkel et al., 2014).

With over 9,000 kilometres, Italy's coast hosts many historically and economically valuable cities and heritage sites. Coastal hazards such as erosion, storm tide inundation and permanent flooding, can have strong adverse impacts on coastal regions, with loss of sandy shores, damage to settlements, infrastructure and ecosystems. Climate change can exacerbate these impacts due to rising sea levels and increasing impacts of waves and storms. Coastal erosion and temporary inundation due to storms are common, in particular in low lying areas of the Po river delta (in Emilia Romagna and Veneto regions).

Coastal areas along the Upper Adriatic Sea (Italy) are highly exposed and vulnerable to coastal floods and the flood risk is projected to further increase as a result of sea level rise (SLR) and local subsidence. We focus on two coastal cities - Rimini (~ 150,000 residents) and Cesenatico (~ 27,000 residents) in Emilia Romagna, both among the most important destinations of summer tourism. For both areas, we assess the coastal flood risk under current and future scenarios and analyse the performance of implemented or planned/hypothetical coastal defence measures. The scenarios of extreme sea level account for the combined effect of sea level rise and subsidence rates. We use a high-resolution hydrodynamic model to identify areas prone to coastal floods under the baseline (undefended) and the structural coastal protection (defended) scenario. The defended scenarios accounts for the effect of a coastal barriers based on the design of *Parco del Mare*, an urban renovation project under construction in Rimini. The same defence structure is modelled along the coastal perimeter of Cesenatico. On the base of probabilistic hazard assessment, we estimated the expected annual damage (EAD) using a locally-calibrated damage model. Well informed coastal risk mitigation and adaptation actions require accurate and detailed information about the characterisation of coastal flood hazard and the performance of coastal defence options. Cost-benefit analysis (CBA) is widely used to evaluate the economic desirability of a disaster risk reduction (DRR) project (Jonkman et al., 2004; Mechler, 2016; Price, 2018), helping decision-makers in evaluating the efficacy of different adaptation options (Bos and Zwaneveld, 2017; Kind, 2014).

The results of the analysis has been published and described in more detail in Amadio, M., Essenfelder, A.H., Bagli, S., Marzi, S., Mazzoli, P., Mysiak, J., Roberts, S., 2022. Cost-benefit analysis of coastal flood defence measures in the North Adriatic Sea. *Nat. Hazards Earth Syst. Sci.* 22, 265–286. <https://doi.org/10.5194/nhess-22-265-2022> (Amadio et al., 2022).

### 3.11.2 Methods

We model coastal inundation as a combined result of high tide, storm surge and action of waves. The latter combines wave setup (defined as an increase of mean sea level at the shore that is caused by the loss of wave momentum in the surf zone) with wave periodicity of incoming breaking waves (which defines wave swash, i.e. the amplitude of the time varying elevation due to breaking waves along the shore). Estimates of storm surge and tides and waves are obtained for the North Adriatic up to year 2100 by combining reference hazard scenarios derived from the analysis of historical records (Armaroli

et al., 2012; Armaroli and Duo, 2018; Perini et al., 2017, 2016, 2011) with regionalised projections of SLR (Vousdoukas et al., 2017) and local vertical land movements (VLM) rates (Carbognin et al., 2009; Perini et al., 2017). We consider four scenarios of extreme sea level (ESL), ranging from low intensity-high frequency to high intensity-low frequency, under current and future (2050 and 2100) conditions.

We use hydrodynamic flood modelling approach which accounts for the effects of wind, waves, tide, current, and river run-off can be used (Barnard et al., 2019). Simplified hydrodynamic flood models focused on nearshore processes can reduce computational cost while taking into consideration water mass conservation (Breilh et al., 2013), aspects of flooding hydrodynamics (Dottori et al., 2018) and the presence of obstacles (Perini et al., 2016). We apply the ANUGA model (Roberts et al., 2015). Land morphology and exposure of coastal settlements are described by high-resolution DTM (LiDAR) and bathymetry, in combination with land use and buildings footprints. The DTM is supplemented with geometries of existing coastal protection elements such as jetties, groins and breakwaters obtained from the digital Regional Technical Map.

In Rimini, the *Parco del Mare* is an urban renovation project which aims to improve the seafront promenade: the existing road and parking lots are converted into an urban green infrastructure consisting of a concrete barrier covered by vegetated sandy dunes with walking paths. This project also acts as a coastal defence system during extreme sea level events. The barrier rises 2.8 meters along the southern section of the town, south of the marina; no barrier is planned on the northern coastal perimeter. The *Parco del Mare* project was completed by 2021 and has been taken in account in the evaluation of the “defended” scenarios by adding the barrier elevation to the digital terrain model (DTM). In Cesenatico, the existing defence structures include a moving barrier system (*Porte Vinciane*) located on the port channel, coupled with a dewatering pump which discharge the meteoric waters in the sea. The barriers close automatically if the TWL surpasses 1 meter over the mean sea level, preventing floods in the historical centre up to 2.2 meters of TWL. Additional defence structures include the winter dunes, which consist of a 2.2 meter-tall intermittent, non-reinforced sand barrier. In the defended scenario, we envisage a coastal defence structure similar to Rimini’s *Parco del Mare* project, spanning both North and South of the port channel with a total length of 7.8 km.



Figure 1: Prototype design of Parco del Mare project in Rimini. Adapted from JDS Architects (Amadio et al., 2022).

The effect of hazard mitigation structures (both designed and under construction) are explicitly accounted by the model in the “defended” scenario, in contrast to the baseline scenario, where only existing defence structures (groins, jetties, breakwaters and sand dunes) are considered.

Direct damage to physical assets is estimated using stage-damage models validated on empirical records (Amadio et al., 2019). The model was adapted to coastal flooding assuming that the dynamic of impact from long-setting floods depends on the same factors, namely: 1) hazard magnitude, and 2) type, size and value of exposed asset. Hazard magnitude can be defined by a range of variables, but the most important predictors of damage are water depth and the extension of the flood event (Jan Huizinga et al., 2017; B Jongman et al., 2012). The characterization of exposed asset is built from a variety of sources, starting from land use and buildings footprints obtained from the Regional

Environmental Agencies geodatabases and the Open Street Map database (Open Street Map, 2019). Additional indicators about buildings characteristics are obtained from the database of the 2011 Italian Census (ISTAT, 2011), while mean construction and restoration costs per building types are obtained from cadastral estimates (CRESME, 2019).

### 3.11.3 Results

The output of the hydrodynamic model consists of a set of inundation simulations that include several hazard intensity variables in relation to flood extent: water depth, flow velocity, and duration of submersion. ESL scenarios are then summarized into inundation maps, each one representing the maximum value reached by hazard intensity variables during the simulated event at about 1 meter resolution. Figure 2 shows the flood extents corresponding to each RP scenario for Cesenatico study area.

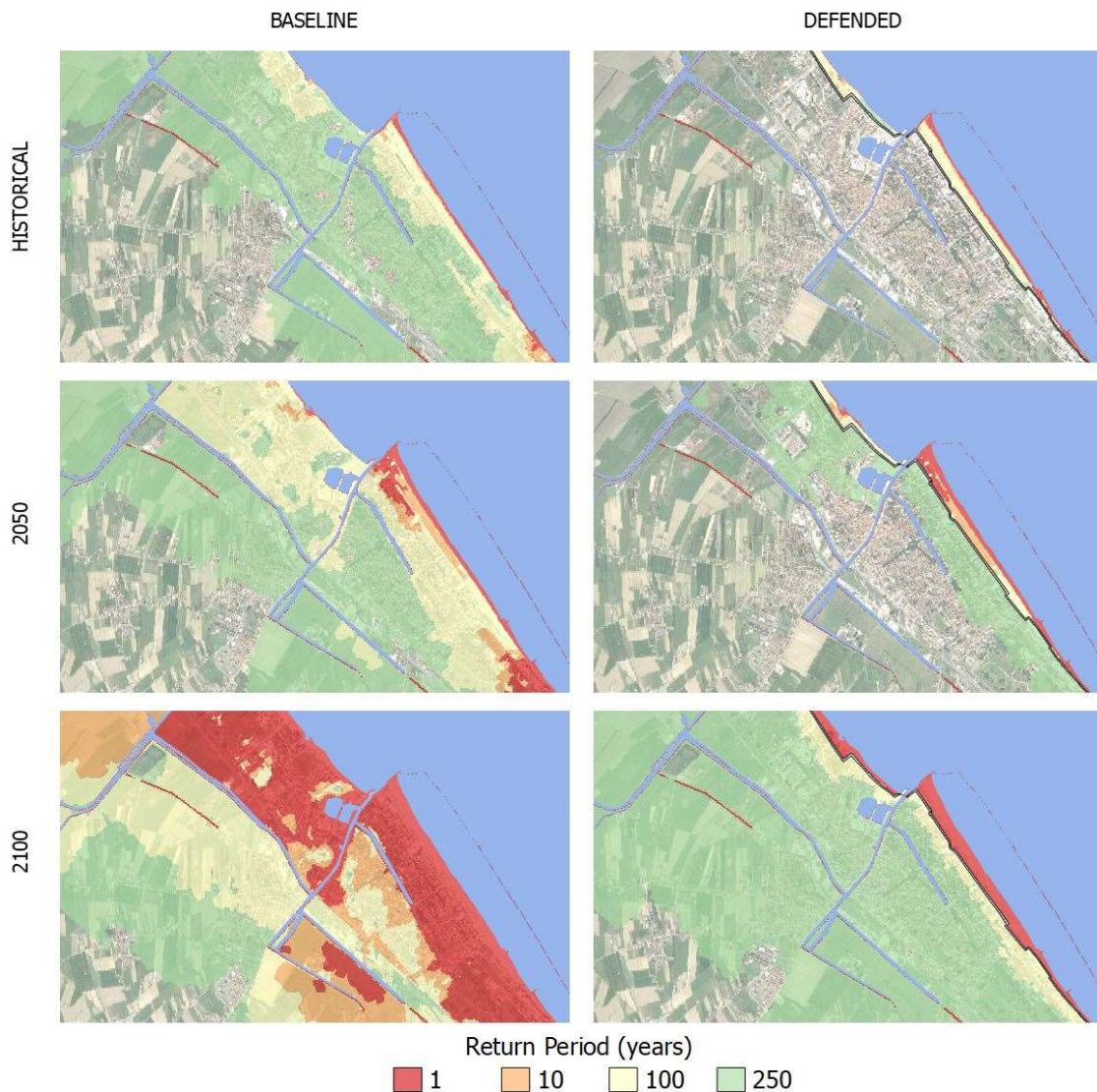


Figure 2: Cesenatico, extent of land affected by flood according to frequency of occurrence of ESL event up to 2100 for the baseline [left] and the defended scenario [right].

The Expected Annual Damage is calculated as a function of maximum exposed value and water depth. In Rimini, the EAD grows from around 650 thousand Eur under historical conditions to 2.8 million Eur

in 2050 and more than 32.3 million Eur in 2100. Under more extreme ESL scenarios, the benefits of the *Parco del Mare* project protecting the southern part of Rimini become more evident, avoiding about 65% of the expected damages in the defended scenarios compared to the undefended ones. In Cesenatico, the average EAD for the undefended scenario grows from around 270 thousand Eur under historical conditions, to 1.7 million Eur in 2050 and almost 26 million Eur in 2100. In our simulations, the designed defence structure (a static barrier with height of 2.8 m along 7.8 km of coast) is able to avoid most of the damage inflicted to residential buildings. The measure becomes less efficient for the most extreme scenarios in 2050 and 2100, when the increase in TWL causes the surmounting of the barrier (Figure 3).

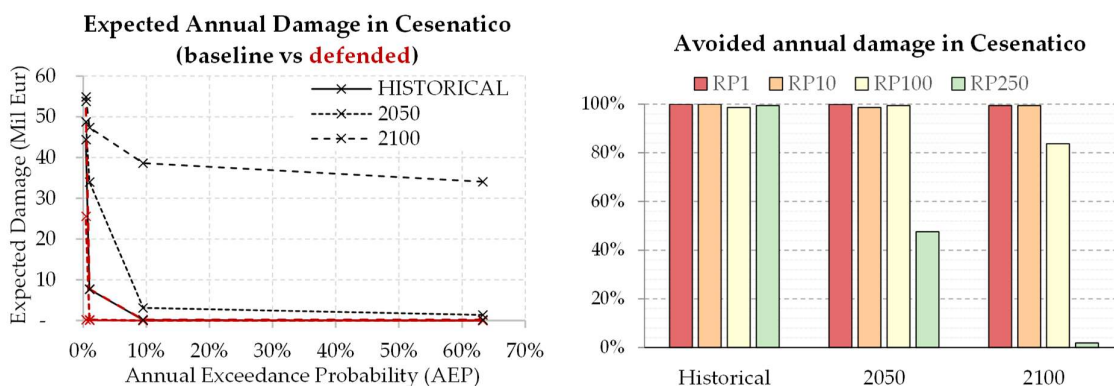


Figure 3: Cesenatico: Expected Annual Damage (EAD) according to undefended scenario up to 2100 [left]; EAD reduction thanks to hazard mitigation offered by the coastal barrier [right].

The estimates of avoided direct flood impacts are accounted in a DRR-oriented CBA to evaluate the feasibility of mitigation measures in terms of NPV, benefit-cost ration (BCR) and payback period for the two time-horizons (2021-2050: 30 years; and 2021-2100: 80 years). The Expected Annual Benefits (EAB) brought by defence measures grow at faster rate approaching 2100 in both sites, because of the larger expected damages from increasing floods severity. The cost of defence implementation is repaid by avoided damage after about 40 years in Cesenatico and after 90 years in Rimini. At 2100, the BCR is 0.9 for Rimini and 1.8 for Cesenatico.

### 3.11.4 Lessons learned

Probabilistic catastrophe models estimate the loss potential by combining properties or assets at risk with modelled hazards and damage/vulnerability models. High performance computing and advances in numerical computing algorithms have made it possible to develop a new generation of hazard and risk models and high-resolution exposure mapping. The EU Adaptation Strategy is supporting the key objectives of the European Green Deal (EC, 2019) and the EU Climate Law (EC, 2021). In February 2021, the European Commission adopted the new and more ambitious EU [Climate Adaptation Strategy](#). The Strategy complements the European Climate Law and sets to foster adaptive capacity and socially-just transformations to climate-resilient society, fully adapted to the unavoidable impacts of climate change. The Strategy lays down policy directions on how to make adaptation smarter, faster and more systemic.

Better understanding of climate related risks and the performance of risk reduction measures is fundamental for smart and accelerated climate adaptation efforts. Here, we estimate cost-benefit ratio of coastal defence measures, including through nature-based (or ecosystem services-related) solutions. We estimated an increase in expected damage for both urban areas from 2021 to 2100: in Cesenatico the EAD grows by a factor 96, in Rimini by a factor 49. Our results show that profitability of the coastal defence projects grow over time in both locations. The EAD under the baseline

hypothesis is expected to increase by 3.5-fold in 2050, up to 10-fold in 2100. The benefits brought by the coastal defence project become much larger in the second half of the century: the EAB grows 6.1-fold in Rimini, 6.5-fold in Cesenatico, from 2050 to 2100. Avoided losses are expected to match the project implementation costs after about 40 years in Cesenatico and 90 years in Rimini. Benefits are found to increase proportionally to costs; the payback period in Cesenatico is the same considering either an investment on the protection of the whole town or only part of it.

## 4 Lessons learned and links established

For part of the use-cases the interaction with the end-users was successfully established and indicators and products were derived that were at a level where they could easily be interpreted and used in follow-up work by the end-users themselves. The storyboards developed by eScienceCenter: [EUCP Storyboards \(eucp-project.github.io\)](https://eucp-project.github.io) provide a low-level summary for many of the use-cases. These storyboards have been shared at the multi-user forum (MUF) meeting to demonstrate what can be done with EUCP dataset and which sectoral assessments can be performed (see for more information deliverable 4.5).

An example of strong stakeholder interaction is the collaboration with super-user JRC. Collaboration was established on the topics (i) future coastal erosion, (ii) decadal predictions for agricultural droughts and (iii) European streamflow projections. It must be said that this collaboration was partly through the scientific staff that were actively contributing to the scientific analysis themselves. But also for the Dutch Coast, the results of the future coastal erosion assessment are actively being shared with the Dutch Water Authority Rijkswaterstaat.

The advantage within the above case-studies was the experience that some of the WP4 partners already had in using the decadal projections, the EU-CORDEX RCM data and global climate projections. As a result, the analysis could be started straight at the beginning of the project.

For other case-studies the plans were ambitious. For example, the application of CP-RCM data from WP3 for flash flooding. These CP-RCM datasets were relatively new and posed quite some challenges in processing and derivation of meaningful indicators. The amount of data, especially for the still to be completed study with the ensemble of CP-RCMs was enormous and although the JupyterLab environment set-up by eScienceCenter enabled the data processing there were quite some hurdles on the way. Still many of the datasets were only available within the project team for the case-studies within the project. In the future it would be valuable when the CP-RCM datasets can, similar to the CORDEX and other CMIP datasets, be accessible through ESGF nodes in a CMOR compliant format. This would highly stimulate the uptake and use in the sectoral impact work by scientist as well as consultants / SMEs. This was also one of the comments received at the Multi-User Forum meeting. Others are keen to start using the data. Although, processing capacity will remain an issue.

Another major challenge was the limited length of the CP-RCM time-series which hamper local statistical analysis. It took more time the first half of the project than anticipated during the proposal phase to tackle all these problems, some of the future CP-RCM datasets only became available after the first years of the project. In the first years of the project end-user contacts had been established for the urban flooding use-case. However, it took three years to generate the first valuable results. In addition, extreme value analysis for the localized urban projections were hampered by the limited length of the CP-RCM time-series and for the Deltares work a switch was made to regional Alpine flash flooding. In the end the end-user interaction was not achieved for this use case. Overall we conclude that the analysis of changes in extreme events could benefit from extended CP-RCM simulations of multiple decades to feed extreme value analysis.

This end-user interaction has been established for the coastal flooding assessment for Rimini as well as for the city of Milan where rainfall extremes were derived from the CP-RCM datasets. This will be discussed in detail in deliverable 4.5. The Rimini and Milan case benefitted from experience gained in other past and ongoing projects.

We do foresee that for the flooding topic and also for the wind drought and wind speed analysis further links can be established with the insurance sector, the energy sector and JRC in the future.

Also, for other use-cases such as the wind drought analysis the climate model variables could not directly be used. Windspeed is available at 10 metres, but for the analysis for wind farms windspeed

at 100 metres is required. This required extra post processing here applied through a machine learning approach.

When evaluating the collaboration within the EUCP project team we see that WP4 successfully employed datasets from WP1, WP2 and WP3. There was strong interaction with the modellers from WP1 for the work done by BSC. There was strong interaction between the modelling groups from WP3 and Deltares. Ensemble interpretation and ensemble weighting techniques from WP2 partners were applied to reduce and interpret the uncertainty in the derived indicators of WP4. Some of the case-studies build upon climate model datasets that were already developed outside the EUCP project.

## References

- Amadio, M., Essenfelder, A.H., Bagli, S., Marzi, S., Mazzoli, P., Mysiak, J., Roberts, S., 2022. Cost-benefit analysis of coastal flood defence measures in the North Adriatic Sea. *Nat. Hazards Earth Syst. Sci.* 22, 265–286. <https://doi.org/10.5194/nhess-22-265-2022>
- Amadio, M., Scorzini, A.R., Carisi, F., Essenfelder, A.H., Domeneghetti, A., Mysiak, J., Castellarin, A., 2019. Testing empirical and synthetic flood damage models: the case of Italy. *Nat. Hazards Earth Syst. Sci.* 19, 661–678. <https://doi.org/10.5194/nhess-19-661-2019>
- Alfieri, L., Burek, P., Feyen, L., Forzieri, G., 2015. Global warming increases the frequency of river floods in Europe. *Hydrology and Earth System Sciences* 19, 2247–2260. doi:10.5194/hess-19-2247-2015.
- Almar, R., Ranasinghe, R., Bergsma, E.W.J., Diaz, H., Melet, A., Papa, F., Vousdoukas, M., Athanasiou, P., Dada, O., Almeida, L.P., Kestenare, E., 2021. A global analysis of extreme coastal water levels with implications for potential coastal overtopping. *Nat. Commun.* 12, 1–9. <https://doi.org/10.1038/s41467-021-24008-9>
- Amponsah, W., Ayril, P.A., Boudevillain, B., Bouvier, C., Braud, I., Brunet, P., Delrieu, G., Didon-Lescot, J.F., Gaume, E., Lebouc, L. et al., 2018. Integrated high-resolution dataset of high-intensity European and Mediterranean flash floods. *Earth System Science Data* 10, 1783–1794, doi:10.5194/essd-10-1783-2018.
- Armaroli, C., Ciavola, P., Perini, L., Calabrese, L., Lorito, S., Valentini, A., Masina, M., 2012. Critical storm thresholds for significant morphological changes and damage along the Emilia-Romagna coastline, Italy. *Geomorphology* 143–144, 34–51. <https://doi.org/10.1016/j.geomorph.2011.09.006>
- Armaroli, C., Duo, E., 2018. Validation of the coastal storm risk assessment framework along the Emilia-Romagna coast. *Coast. Eng.* 134, 159–167. <https://doi.org/10.1016/j.coastaleng.2017.08.014>
- Athanasiou, P., van Dongeren, A., Giardino, A., Vousdoukas, M., Gaytan-Aguilar, S., Ranasinghe, R., 2019. Global distribution of nearshore slopes with implications for coastal retreat. *Earth Syst. Sci. Data* 11, 1515–1529. <https://doi.org/10.5194/essd-11-1515-2019>
- Athanasiou, P., van Dongeren, A., Giardino, A., Vousdoukas, M.I., Ranasinghe, R., Kwadijk, J., 2020. Uncertainties in projections of sandy beach erosion due to sea level rise: an analysis at the European scale. *Sci. Rep.* 10, 11895. <https://doi.org/10.1038/s41598-020-68576-0>
- Athanasiou, P., van Dongeren, A., Giardino, A., Vousdoukas, M., Antolinez, J.A.A., Ranasinghe, R., 2021. A Clustering Approach for Predicting Dune Morphodynamic Response to Storms Using Typological Coastal Profiles: A Case Study at the Dutch Coast. *Front. Mar. Sci.* 8, 1–20. <https://doi.org/10.3389/fmars.2021.747754>
- Bamber, J.L., Aspinall, W.P., 2013. An expert judgement assessment of future sea level rise from the ice sheets. *Nat. Clim. Chang.* 3, 424–427. <https://doi.org/10.1038/nclimate1778>
- Ban, N. et al., 2021. The first multi-model ensemble of regional climate simulations at 413 km resolution, part I: evaluation of precipitation. *Climate Dynamics*, 414, 1–28, doi:10.1007/s00382-021-05708-w

Barnard, P.L., Erikson, L.H., Foxgrover, A.C., Hart, J.A.F., Limber, P., O'Neill, A.C., van Ormondt, M., Vitousek, S., Wood, N., Hayden, M.K., Jones, J.M., 2019. Dynamic flood modeling essential to assess the coastal impacts of climate change. *Sci. Rep.* 9, 1–13. <https://doi.org/10.1038/s41598-019-40742-z>

Berthou, S., Kendon, E.J., Chan, S.C., Ban, N., Leutwyler, D., Schär, C., Fosser, G., 2018. Pan-European climate at convection-permitting scale: a model intercomparison study. *Climate Dynamics*, 1–25, doi:10.1007/s00382-018-4114-6.

Bethke, I., Wang, Y., Counillon, F., Keenlyside, N., Kimmritz, M., Fransner, F., et al. (2021). NorCPM1 and its contribution to CMIP6 DCP. *Geoscientific Model Development*, 14, 7073–7116, <https://doi.org/10.5194/GMD-14-7073-2021>

Bilbao, R., Wild, S., Ortega, P., Acosta-Navarro, J., Arsouze, T., Bretonnière, P. A., et al (2021). Assessment of a full-field initialised decadal climate prediction system with the CMIP6 version of EC-Earth. *Earth System Dynamics*. <https://doi.org/10.5194/esd-12-173-2021>

Boer, G. J., Smith, D. M., Cassou, C., Doblas-Reyes, F., Danabasoglu, G., Kirtman, B., et al. (2016). The Decadal Climate Prediction Project (DCPP) contribution to CMIP6, *Geoscientific Model Development*. <https://doi.org/10.5194/gmd-9-3751-2016>

Borchert, L. F., Menary, M. B., Swingedouw, D., Sgubin, G., Hermanson, L., and Mignot, J. (2021). Improved decadal predictions of North Atlantic subpolar gyre SST in CMIP6. *Geophysical Research Letters*. <https://doi.org/10.1029/2020GL091307>

Bos, F., Zwaneveld, P., 2017. Cost-Benefit Analysis for Flood Risk Management and Water Governance in the Netherlands: An Overview of One Century. *SSRN Electron. J.* <https://doi.org/10.2139/ssrn.3023983>

Boucher, O., Servonnat, J., Albright, A. L., Aumont, O., Balkanski, Y., Bastrikov, V., et al (2020). Presentation and Evaluation of the IPSL-CM6A-LR Climate Model. *Journal of Advances in Modeling Earth Systems*. <https://doi.org/10.1029/2019MS002010>

Bouwer, L.M., 2011. Have disaster losses increased due to anthropogenic climate change? *Bull. Am. Meteorol. Soc.* <https://doi.org/10.1175/2010BAMS3092.1>

Breiman, L. (2001). Random forests. *Machine learning*, 45(1), 5-32.

Breilh, J.F., Chaumillon, E., Bertin, X., Gravelle, M., 2013. Assessment of static flood modeling techniques: Application to contrasting marshes flooded during Xynthia (western France). *Nat. Hazards Earth Syst. Sci.* 13, 1595–1612. <https://doi.org/10.5194/nhess-13-1595-2013>

Brunner, L., Lorenz, R., Zumwald, M., Knutti, R. (2019). Quantifying uncertainty in european climate projections using combined performance-independence weighting. *Env. Res. Lett.*, 14 (12), 124010.

Bruun, P., 1962. Sea-Level Rise as a Cause of Shore Erosion. *J. Waterw. Harb. Div.* 88, 117–130. <https://doi.org/10.1061/JWHEAU.0000252>

Burek, P., Satoh, Y., Kahil, T., Tang, T., Greve, P., Smilovic, M., Guillaumot, L., Zhao, F., and Wada, Y. (2020). Development of the Community Water Model (CWatM v1.04) – a high-resolution hydrological model for global and regional assessment of integrated water resources management, *Geosci. Model Dev.*, 13, 3267–3298, <https://doi.org/10.5194/gmd-13-3267-2020>

Burek, P., Y. Satoh, T. Kahil, T. Tang, P. Greve, M. Smilovic, L. Guillaumot, and Y. Wada. 2019. “Development of the Community Water Model (CWatM v1.04) A High-Resolution Hydrological Model for Global and Regional Assessment of Integrated Water Resources Management.” *Geoscientific Model Development*, August, 1–49. <https://doi.org/10.5194/gmd-2019-214>.

Carbognin, L., Teatini, P., Tosi, L., 2009. The impact of relative sea level rise on the Northern Adriatic Sea coast, Italy, in: *WIT Transactions on Ecology and the Environment*. pp. 137–148. <https://doi.org/10.2495/RAV090121>

Cherchi, A., Fogli, P. G., Lovato, T., Peano, D., Iovino, D., Gualdi, S., et al. (2018). Global Mean Climate and Main Patterns of Variability in the CMCC-CM2 Coupled Model. *Journal of Advances in Modeling Earth Systems*. <https://doi.org/10.1029/2018MS001369>

Church, J.A., Clark, P.U., Cazenave, A., Gregory, J.M., Jevrejeva, S., Levermann, A., Merrifield, M.A., Milne, G.A., Nerem, R.S., Nunn, P.D., Payne, A.J., Pfeffer, W.T., Stammer, D., Unnikrishnan, A.S., 2013. *Sea level change*, PM Cambridge University Press.

CLC: Corine Land Cover 2018. European Union. Copernicus Land Monitoring Service. European Environment Agency (EEA), 2018.

Collet, I., Engelbert, A., 2013. Coastal regions: people living along the coastline, integration of NUTS 2010 and latest population grid, *Statistics in focus*. Eurostat.

Comune di Milano: Tetti Verdi potenziali, 2016.

Cornes, R., van der Schrier, G., van den Besselaar, E.J.M. and Jones, P.D. (2018): An Ensemble Version of the E-OBS Temperature and Precipitation Datasets, *J. Geophys. Res. Atmos.*, 123. doi:10.1029/2017JD028200

CRESME, 2019. I costi di costruzione in edilizia residenziale, industriale per uffici ed alberghiera.

Doblas-Reyes, F. J., Andreu-Burillo, I., Chikamoto, Y., García-Serrano, J., Guemas, V., Kimoto, M., et al. (2013). Initialized near-term regional climate change prediction. *Nature Communications*. <https://doi.org/10.1038/ncomms2704>

Doblas-Reyes, F. J., Hagedorn, R., and Palmer, T. N. (2005). The rationale behind the success of multi-model ensembles in seasonal forecasting - II. Calibration and combination. *Tellus A: Dynamic Meteorology and Oceanography*. <https://doi.org/10.3402/tellusa.v57i3.14658>

von Döhren, P. and Haase, D.: Ecosystem disservices research: A review of the state of the art with a focus on cities, *Ecol. Indic.*, 52, 490–497, doi:<http://dx.doi.org/10.1016/j.ecolind.2014.12.027>, 2015.

Dosio, A., and Paruolo, P. (2011). Bias correction of the ENSEMBLES high-resolution climate change projections for use by impact models: Evaluation on the present climate. *J. Geophys. Res. – Atmos.* 116(16), DOI: 10.1029/2011JD015934.

Dottori, F., Martina, M.L.V., Figueiredo, R., 2018. A methodology for flood susceptibility and vulnerability analysis in complex flood scenarios. *J. Flood Risk Manag.* 11, S632–S645. <https://doi.org/10.1111/jfr3.12234>

Eade, R., Smith, D., Scaife, A., Wallace, E., Dunstone, N., Hermanson, L., and Robinson, N. (2014). Do seasonal-to-decadal climate predictions underestimate the predictability of the real world? *Geophysical Research Letters*. <https://doi.org/10.1002/2014GL061146>

Easterling, D. R., G. A. Meehl, C. Parmesan, S. A. Changnon, T. R. Karl, and L. O. Mearns (2000), Climate extremes: Observations, modeling, and impacts, *Science*, 289, 2068–2074.

EC: Green Infrastructure (GI) — Enhancing Europe’s Natural Capital., 2013a.

EC: Synthesis document n ° 1 - Introducing Natural Water Retention Measures: what are NWRM?, 2013b.

EC, 2021. Regulation (EU) 2021/1119 of the European Parliament and of the Council of 30 June 2021 establishing the framework for achieving climate neutrality and amending Regulations (EC) No 401/2009 and (EU) 2018/1999 ('European Climate Law'). *Off. J. Eur. Communities* 243, 1–17.

EC, 2019. Communication from the Commission to the European Parliament, the European Council, the Council, the European Economic and Social Committee and the Committee of the Regions - the European Green Deal COM/2019/640 final.

EEA: Green Infrastructure and Flood Management: Promoting cost-efficient flood risk reduction via green infrastructure solutions., 2017.

EEA: Healthy environment, healthy lives: how the environment influences health and well-being in Europe., 2020.

Efron, B., & Tibshirani, R. J. (1994). *An introduction to the bootstrap*. CRC press.

Eilander, D., van Verseveld, W., Yamazaki, D., Weerts, A., Winsemius, H. C., and Ward, P. J.: A hydrography upscaling method for scale-invariant parametrization of distributed hydrological models, *Hydrol. Earth Syst. Sci.*, 25, 5287–5313, <https://doi.org/10.5194/hess-25-5287-2021>, 2021.

Essenfelder, A. H., Bagli, S., Mysiak, J., Pal, J. S., Mercogliano, P., Reder, A., Rianna, G., Mazzoli, P., Broccoli, D. and Luzzi, V.: Probabilistic Assessment of Pluvial Flood Risk across 20 European Cities: A Demonstrator of the Copernicus Disaster Risk Reduction Service for Pluvial Flood Risk in Urban Areas, *Water Econ. Policy*, 2021 (under review).

Eyring, V., Bony, S., Meehl, G. A., Senior, C. A., Stevens, B., Stouffer, R. J., and Taylor, K. E. (2016). Overview of the Coupled Model Intercomparison Project Phase 6 (CMIP6) experimental design and organization, *Geoscientific Model Development*. <https://doi.org/10.5194/gmd-9-1937-2016>

Felder, G., Gómez-Navarro, J.J., Zischg, A.P., Raible, C.C., Rötthlisberger, V., Bozhinova, D., Martius, O., Weingartner, R., 2018. From global circulation to local flood loss: Coupling models across the scales. *Science of The Total Environment* 635, 1225 – 1239. doi: 10.1016/j.scitotenv.2018.04.170.

Ferri, S., Siragusa, A., Sabo, F., Pafi, M. and Halkia, M.: The European Settlement Map 2017 Release., 2017.

Fonti, V., & Belitser, E. (2017). Feature selection using lasso. VU Amsterdam research paper in business analytics, 30, 1-25.

Fortin, V., Abaza, M., Anctil, F., and Turcotte, R. (2014). Why Should Ensemble Spread Match the RMSE of the Ensemble Mean? *Journal of Hydrometeorology*. <https://doi.org/10.1175/JHM-D-14-0008.1>

Förster, K. and Thiele, L.B., 2020. Variations in sub-daily precipitation at 493 centennial scale. *npj Climate and Atmospheric Science* 3, 1–7. URL: 494 <https://doi.org/10.1038/s41612-020-0117-1>, doi:10.1038/s41612-020-0117-1.

Gaume, E., Bain, V., Bernardara, P., Newinger, O., Barbuc, M., Bateman, A., Blaskovicova, L., Blöschl, G., Borga, M., Dumitrescu, A., et al., 2009. A compilation of data on european flash floods. *Journal of Hydrology* 367, 70–78. 503 doi:10.1016/j.jhydrol.2008.12.028

Giorgi, F. and E. Coppola (2007) European climate-change oscillation (ECO). *Geophys. Res. Lett.*, 34, p. L21703, <https://doi.org/10.1029/2007GL031223>

Green, W. H. and Ampt, G. A.: *Studies on Soil Physics. Part I. The Flow of Air and Water through Soils*, *J. Agric. Res.*, 4(1), 1–24, 1911.

Greve, P., T. Kahil, J. Mochizuki, T. Schinko, Y. Satoh, P. Burek, G. Fischer, et al. 2018. “Global Assessment of Water Challenges under Uncertainty in Water Scarcity Projections.” *Nature Sustainability* 1 (9): 486–94. <https://doi.org/10.1038/s41893-018-0134-9>.

Hallegatte, S., Green, C., Nicholls, R.J., Corfee-Morlot, J., 2013. Future flood losses in major coastal cities. *Nat. Clim. Chang.* 3, 1–5. <https://doi.org/10.1038/nclimate1979>

Hersbach, H., Bell, B., Berrisford, P., Hirahara, S., Horányi, A., Muñoz-Sabater, J., et al. (2020). The ERA5 global reanalysis. *Royal Meteorological Society*. <https://doi.org/10.1002/qj.3803>

Hinkel, J., Lincke, D., Vafeidis, A.T., Perrette, M., Nicholls, R.J., Tol, R.S.J., Marzeion, B., Fettweis, X., Ionescu, C., Levermann, A., 2014. Coastal flood damage and adaptation costs under 21st century sea-level rise. *Proc. Natl. Acad. Sci.* 111, 3292–3297. <https://doi.org/10.1073/pnas.1222469111>

Huizinga, J., de Moel, H., Szewczyk, W., 2017. Global flood depth-damage functions. Methodology and the database with guidelines. EUR 28552 EN. doi: 10.2760/16510.

Huizinga, Jan, De Moel, H., Szewczyk, W., 2017. Methodology and the database with guidelines Global flood depth-damage functions. <https://doi.org/10.2760/16510>

Imhoff, R. O., van Verseveld, W. J., van Osnabrugge, B., & Weerts, A. H. (2020). Scaling Point-Scale (Pedo)transfer Functions to Seamless Large-Domain Parameter Estimates for High-Resolution

Distributed Hydrologic Modeling: An Example for the Rhine River. *Water Res. Res.*, 56(4), <https://doi.org/10.1029/2019WR026807>

ISTAT, 2011. 15° censimento della popolazione e delle abitazioni.

Jackson, L.P., Jevrejeva, S., 2016. A probabilistic approach to 21st century regional sea-level projections using RCP and High-end scenarios. *Glob. Planet. Change* 146, 179–189. <https://doi.org/10.1016/j.gloplacha.2016.10.006>

Jacob, D., Teichmann, C., Sobolowski, S. et al. Regional climate downscaling over Europe: perspectives from the EURO-CORDEX community. *Reg Environ Change* 20, 51 (2020). <https://doi.org/10.1007/s10113-020-01606-9>

Jamil, R. A., Chaigneau, A., Gilloteaux, J. C., Lelong, P., & Babarit, A. (2019, October). Comparison of the capacity factor of stationary wind turbines and weather-routed energy ships in the far-offshore. In *Journal of Physics: Conference Series* (Vol. 1356, No. 1, p. 012001). IOP Publishing.

Jang, Y., & Byon, E. (2020). Probabilistic Characterization of Wind Diurnal Variability for Wind Resource Assessment. *IEEE Transactions on Sustainable Energy*, 11(4), 2535-2544.

Jongman, B, Kreibich, H., Apel, H., Barredo, J.I., Bates, P.D., Feyen, L., Gericke, A., Neal, J., Aerts, J.C.J.H., Ward, P.J., 2012. Comparative flood damage model assessment: towards a European approach. *Nat. Hazards Earth Syst. Sci.* 12, 3733–3752. <https://doi.org/10.5194/nhess-12-3733-2012>

Jongman, Brenden, Ward, P.J., Aerts, J.C.J.H., 2012. Global exposure to river and coastal flooding: Long term trends and changes. *Glob. Environ. Chang. Policy Dimens.* 22, 823–835. <https://doi.org/10.1016/j.gloenvcha.2012.07.004>

Jonkman, S.N., Brinkhuis-Jak, M., Kok, M., 2004. Cost benefit analysis and flood damage mitigation in the Netherlands. *Heron* 49, 95–111.

Jourdier, B. (2020). Evaluation of ERA5, MERRA-2, COSMO-REA6, NEWA and AROME to simulate wind power production over France. *Advances in Science and Research*, 17, 63-77.

Kind, J.M., 2014. Economically efficient flood protection standards for the Netherlands. *J. Flood Risk Manag.* 7, 103–117. <https://doi.org/10.1111/jfr3.12026>

Knijff, J. M. V. D., Younis, J. and Roo, A.P.J.D. (2010) LISFLOOD: a GIS-based distributed model for river basin scale water balance and flood simulation. *Int. J. Geogr. Inf. Sci.* 24, 189–212 (2010).

Kobayashi, S., Ota, Y., Harada, Y., Ebata, A., Moriya, M., Onoda, H., et al. (2015). The JRA-55 reanalysis: General specifications and basic characteristics. *Journal of the Meteorological Society of Japan.* <https://doi.org/10.2151/jmsj.2015-001>

Kreibich, H., Botto, A., Merz, B., Schröter, K., 2017. Probabilistic, Multivariable Flood Loss Modeling on the Mesoscale with BT-FLEMO. *Risk Anal.* 37, 774–787. <https://doi.org/10.1111/risa.12650>

Lehner, B. & Grill, G. Global river hydrography and network routing: baseline data and new approaches to study the world's large river systems. *Hydrological Processes* 27,2171-2186 (2013)

- Li, F., Gelder, P.H.A.J.M. van, Vrijling, J.K., Callaghan, D.P., Jongejan, R.B., Ranasinghe, R., 2014. Probabilistic estimation of coastal dune erosion and recession by statistical simulation of storm events. *Appl. Ocean Res.* 47, 53–62. <https://doi.org/10.1016/j.apor.2014.01.002>
- Lledó, Ll., Torralba, V., Soret, A., Ramon, J., and Doblas-Reyes, F. J. (2019). Seasonal forecast of wind power generation. *Renewable Energy*. <https://doi.org/10.1016/j.renene.2019.04.135>
- Loon, A. F. Van, T. Gleeson, J. Clark, A. I. J. M. Van Dijk, K. Stahl, J. Hannaford, G. Di Baldassarre, et al. 2016. “Drought in the Anthropocene.” *Comments and Opinion. Nature Geoscience*. February 2, 2016. <https://doi.org/10.1038/ngeo2646>
- Luijendijk, A., Hagenaars, G., Ranasinghe, R., Baart, F., Donchyts, G., Aarninkhof, S., 2018. The State of the World’s Beaches. *Sci. Rep.* 8, 6641. <https://doi.org/10.1038/s41598-018-24630-6>
- Mauritsen, T., Bader, J., Becker, T., Behrens, J., Bittner, M., Brokopf, R., et al. (2019). Developments in the MPI-M Earth System Model version 1.2 (MPI-ESM1.2) and its response to increasing CO<sub>2</sub>. *Journal of Advances in Modeling Earth Systems*. <https://doi.org/10.1029/2018MS001400>
- McCall, R.T., Van Thiel de Vries, J.S.M., Plant, N.G., Van Dongeren, A.R., Roelvink, J.A., Thompson, D.M., Reniers, A.J.H.M., 2010. Two-dimensional time dependent hurricane overwash and erosion modeling at Santa Rosa Island. *Coast. Eng.* 57, 668–683. <https://doi.org/10.1016/j.coastaleng.2010.02.006>
- McGranahan, G., Balk, D., Anderson, B., 2007. The rising tide: Assessing the risks of climate change and human settlements in low elevation coastal zones. *Environ. Urban.* <https://doi.org/10.1177/0956247807076960>
- Mechler, R., 2016. Reviewing estimates of the economic efficiency of disaster risk management: opportunities and limitations of using risk-based cost–benefit analysis. *Nat. Hazards* 81, 2121–2147. <https://doi.org/10.1007/s11069-016-2170-y>
- Merryfield, W. J., Baehr, J., Batté, L., Becker, E. J., Butler, A. H., Coelho, C. A. S., et al. (2020). Current and Emerging Developments in Subseasonal to Decadal Prediction. *Bulletin of the American Meteorological Society*. <https://doi.org/10.1175/BAMS-D-19-0037.1>
- Miao, C., Su, L., Sun, Q., & Duan, Q. (2016). A nonstationary bias-correction technique to remove bias in GCM simulations. *Journal of Geophysical Research: Atmospheres*, 121(10), 5718–5735.
- Mitchell, M. G. E., Bennett, E. M. and Gonzalez, A.: Linking Landscape Connectivity and Ecosystem Service Provision: Current Knowledge and Research Gaps, *Ecosystems*, 16(5), 894–908, doi:10.1007/s10021-013-9647-2, 2013.
- Mitchell, M. G. E., Suarez-Castro, A. F., Martinez-Harms, M., Maron, M., McAlpine, C., Gaston, K. J., Johansen, K. and Rhodes, J. R.: Reframing landscape fragmentation’s effects on ecosystem services, *Trends Ecol. Evol.*, 30(4), 190–198, doi:10.1016/J.TREE.2015.01.011, 2015.
- Muis, S., Verlaan, M., Winsemius, H.C., Aerts, J.C.J.H., Ward, P.J., 2016. A global reanalysis of storm surges and extreme sea levels. *Nat. Commun.* 7, 11969.

Müller, W., Jungclaus, J., Mauritsen, T., Baehr, J., Bittner, M., Budich, R., et al. (2018). A higher-resolution version of the Max Planck Institute Earth System Model (MPI-ESM 1.2-HR). *Journal of Advances in Modeling Earth Systems*. <https://doi.org/10.1029/2017MS001217>

Mysiak, J., Daniell, J. and Vanneuville, W.: Economic losses from weather and climate-related events in Europe, Technical report of the European Topic Centre on Climate Change Impacts, Vulnerability and Ad-aptation (ETC-CA), European Environment Agency, Copenhagen, Denmark, Copenhagen (Denmark)., 2022.

Nicholls, R.J., Cazenave, A., 2010. Sea-level rise and its impact on coastal zones. *Science* (80). <https://doi.org/10.1126/science.1185782>

Olaofe, Z. O. (2016). A surface-layer wind speed correction: A case-study of Darling station. *Renewable Energy*, 93, 228-244.

OpenStreetMap contributors, 2015. OSM coastline [WWW Document]. URL <https://planet.osm.org/> (accessed 2.22.18).

Open Street Map, 2019. Open Street Map data for Nord-Est Italy [WWW Document].

OSM: OpenStreetMaps, 2021.

Paprotny, D., Morales Napoles, O., Jonkman, S.N., 2017. Hanze database of historical damaging floods in europe, 1870-2016. URL: [https://data.4tu.nl/repository/collection:HANZE, doi:10.4121/uuid:5b75be6a-4dd4-472e-9424-f7ac4f7367f6](https://data.4tu.nl/repository/collection:HANZE,doi:10.4121/uuid:5b75be6a-4dd4-472e-9424-f7ac4f7367f6).

Pascual-Hortal, L. and Saura, S.: Comparison and development of new graph-based landscape connectivity indices: towards the prioritization of habitat patches and corridors for conservation, *Landsc. Ecol.*, 21(7), 959–967, doi:10.1007/s10980-006-0013-z, 2006.

Perini, L., Calabrese, L., Deserti, M., Valentini, A., Ciavola, P., Armaroli, C., 2011. Le mareggiate e gli impatti sulla costa in Emilia-Romagna 1946-2010, Quaderni ARPA.

Perini, L., Calabrese, L., Luciani, P., Olivieri, M., Galassi, G., Spada, G., 2017. Sea-level rise along the Emilia-Romagna coast (Northern Italy) in 2100: scenarios and impacts. *Nat. Hazards Earth Syst. Sci.* 17, 2271–2287. <https://doi.org/10.5194/nhess-17-2271-2017>

Perini, L., Calabrese, L., Salerno, G., Ciavola, P., Armaroli, C., 2016. Evaluation of coastal vulnerability to flooding: comparison of two different methodologies adopted by the Emilia-Romagna region (Italy). *Nat. Hazards Earth Syst. Sci.* 16, 181–194. <https://doi.org/10.5194/nhess-16-181-2016>

Piani, C., Weedon, G. P., Best, M., Gomes, S. M., Viterbo, P., Hagemann, S. et al. (2010), Statistical bias correction of global simulated daily precipitation and temperature for the application of hydrological models, *J. Hydrol.*, 395, 199–215, doi:10.1016/j.jhydrol.2010.10.024.

Portmann, F.T., Siebert, S. and Döll, P. (2010). MIRCA2000—Global monthly irrigated and rainfed crop areas around the year 2000: A new high-resolution data set for agricultural and hydrological modeling. *Global biogeochemical cycles*. <https://doi.org/10.1029/2008GB003435>

Prasad, A. M., Iverson, L. R., & Liaw, A. (2006). Newer classification and regression tree techniques: bagging and random forests for ecological prediction. *Ecosystems*, 9(2), 181-199.

Price, R., 2018. Cost-effectiveness of disaster risk reduction and adaptation to climate change 1–21.

Ramon, J., Lledó, Ll., Bretonnière, P.-A., Samsó, M., and Doblas-Reyes, F. J. (2021). A perfect prognosis downscaling methodology for seasonal prediction of local-scale wind speeds. *Environmental Research Letters*. <https://doi.org/10.1088/1748-9326/abe491>

Rehman, S., & Al-Abbadi, N. M. (2007). Wind shear coefficients and energy yield for Dhahran, Saudi Arabia. *Renewable Energy*, 32(5), 738-749.

Rhee, J., Park, S., & Lu, Z. (2014). Relationship between land cover patterns and surface temperature in urban areas. *GIScience & remote sensing*, 51(5), 521-536.

Price, R., 2018. Cost-effectiveness of disaster risk reduction and adaptation to climate change 1–21.

Roberts, S., Nielsen, O., Gray, D., Sexton, J., 2015. ANUGA User Manual. <https://doi.org/10.13140/RG.2.2.12401.99686>

Roelvink, D., Reniers, A., van Dongeren, A., van Thiel de Vries, J., McCall, R., Lescinski, J., 2009. Modelling storm impacts on beaches, dunes and barrier islands. *Coast. Eng.* 56, 1133–1152. <https://doi.org/10.1016/j.coastaleng.2009.08.006>

Rudd, A.C., Kay, A.L., Wells, S.C., Aldridge, T., Cole, S.J., Kendon, E.J., Stewart, E.J., 2020. Investigating potential future changes in surface water flooding hazard and impact. *Hydrological Processes* 34, 139–149. Doi: 10.1002/hyp.13572.

Samela, C., Persiano, S., Bagli, S., Luzzi, V., Mazzoli, P., Humer, G., Reithofer, A., Essenfelder, A., Amadio, M., Mysiak, J. and Castellarin, A.: Safer\_RAIN: A DEM-Based Hierarchical Filling-& Spilling Algorithm for Pluvial Flood Hazard Assessment and Mapping across Large Urban Areas, , 12(6), 1514 [online] Available from: <https://www.mdpi.com/2073-4441/12/6/1514> (Accessed 26 May 2020), 2020.

Scaife, A. A. and Smith, D. A. (2018). Signal-to-noise paradox in climate science. *npj Climate and Atmospheric Science*. <https://doi.org/10.1038/s41612-018-0038-4>

Sellar, A. A., Walton, J., Jones, C. G., Wood, R., Luke Abraham, N., Andrejczuk, M., et al. (2020). Implementation of U.K. Earth System Models for CMIP6. *Journal of Advances in Modeling Earth Systems*. <https://doi.org/10.1029/2019MS001946>

Sheffield, J., and E. F. Wood (2008), Projected changes in drought occurrence under future global warming from multi-model, multi-scenario, IPCC AR4 simulations, *Clim. Dyn.*, 31(1), 79–105.

Smith, D. M., Scaife, A. A., Eade, R., Athanasiadis, P., Belluci, A., Bethke, I., et al. (2020). North Atlantic climate far more predictable than models imply. *Nature*. <https://doi.org/10.1038/s41586-020-2525-0>

Soares, M.B., Alexander, M. and Dessai, S. (2018). Sectoral use of climate information in Europe: A synoptic overview. *Climate Services*. <https://doi.org/10.1016/j.cliser.2017.06.001>

Soille, P. and Vogt, P.: Morphological segmentation of binary patterns, *Pattern Recognit. Lett.*, 30(4), 456–459, doi:<https://doi.org/10.1016/j.patrec.2008.10.015>, 2009.

Soret, A., Torralba, V., Cortesi, N., Christel, I., Palma, Ll., Manrique-Suñen, A., et al. (2019). *Journal of Physics: Conference Series*. <https://doi.org/10.1088/1742-6596/1222/1/012009>

Stott, P. A., Christidis, N., Otto, F. E., Sun, Y., Vanderlinden, J. P., van Oldenborgh, G. J., ... & Zwiers, F. W. (2016). Attribution of extreme weather and climate-related events. *Wiley Interdisciplinary Reviews: Climate Change*, 7(1), 23-41.

Sudmeier-Rieux, K., Arce-Mojica, T., Boehmer, H. J., Doswald, N., Emerton, L., Friess, D. A., Galvin, S., Hagenlocher, M., James, H., Laban, P., Lacambra, C., Lange, W., McAdoo, B. G., Moos, C., Mysiak, J., Narvaez, L., Nehren, U., Peduzzi, P., Renaud, F. G., Sandholz, S., Schreyers, L., Sebesvari, Z., Tom, T., Triyanti, A., van Eijk, P., van Staveren, M., Vicarelli, M. and Walz, Y.: Scientific evidence for ecosystem-based disaster risk reduction, *Nat. Sustain.*, doi:10.1038/s41893-021-00732-4, 2021.

Swart, N. C., Cole, J. N. S., Kharin, V. V., Lazare, M., Scinocca, J. F., Gillett, N. P., et al. (2019). The Canadian Earth System Model version 5 (CanESM5.0.3). *Geoscientific Model Development*. <https://doi.org/10.5194/gmd-12-4823-2019>

Syvitski, J.P.M., Kettner, A.J., Overeem, I., Hutton, E.W.H., Hannon, M.T., Brakenridge, G.R., Day, J., Vörösmarty, C., Saito, Y., Giosan, L., Nicholls, R.J., 2009. Sinking deltas due to human activities. *Nat. Geosci.* <https://doi.org/10.1038/ngeo629>

Tarolli, P., Borga, M., Morin, E., Delrieu, G., 2012. Analysis of flash flood regimes in the north-western and south-eastern mediterranean regions. *Natural Hazards and Earth System Sciences* 12, 1255–1265. doi:10.5194/nhess-12- 667 1255-2012.

Tatebe, H., Ogura, T., Nitta, T., Komuro, Y., Ogochi, K., Takemura, T., et al. (2019). Description and basic evaluation of simulated mean state, internal variability, and climate sensitivity in MIROC6. *Geoscientific Model Development*. <https://doi.org/10.5194/gmd-12-2727-2019>

Tian, T., Yang, S., Karami, M. P., Massonnet, F., Kruschke, T., and Koenigk, T. (2021). Benefits of sea ice initialization for the interannual-to-decadal climate prediction skill in the Arctic in EC-Earth3. *Geoscientific Model Development*. <https://doi.org/10.5194/gmd-14-4283-2021>

Tian, Q., G. Huang, K. Hu, and D. Niyogi, 2019: Observed and global climate model based changes in wind power potential over the Northern Hemisphere during 1979–2016. *Energy*, 167, 1224–1235, doi:10.1016/j.energy.2018.11.027.

Torralba, V., Doblas-Reyes, F. J., MacLeod, D., Christel, I., and Davis, M. (2017). Seasonal climate prediction: a new source of information for the management of wind energy resources. *Journal of Applied Meteorology and Climatology*. <https://doi.org/10.1175/JAMC-D-16-0204.1>

Trenberth, K. E. and Shea, D. J. (2006). Atlantic hurricanes and natural variability in 2005. *Geophysical Research Letters*. <https://doi.org/10.1029/2006GL026894>

Van Den Dool, H.M. and Toth, Z. (1991). Why do forecasts for “near normal” often fail?. *Weather and forecasting*. [https://doi.org/10.1175/1520-0434\(1991\)006<0076:WDFFNO>2.0.CO](https://doi.org/10.1175/1520-0434(1991)006<0076:WDFFNO>2.0.CO)

- van Dongeren, A., Ciavola, P., Martinez, G., Viavattene, C., Bogaard, T., Ferreira, O., Higgins, R., McCall, R., 2018. Introduction to RISC-KIT: Resilience-increasing strategies for coasts. *Coast. Eng.* 134, 2–9. <https://doi.org/10.1016/j.coastaleng.2017.10.007>
- Vautard, R., Colette, A., Van Meijgaard, E., Meleux, F., Van Oldenborgh, G. J., Otto, F., ... & Yiou, P. (2017). Attribution of wintertime anticyclonic stagnation contributing to air pollution in Western Europe. *Bulletin of the American Meteorological Society*, 99(1), S70-S75.
- Vautard, R., Gobiet, A., Sobolowski, S., Kjellström, E., Stegehuis, A., Watkiss, P., ... & Jacob, D. (2014). The European climate under a 2° C global warming. *Environmental Research Letters*, 9(3), 034006.
- Vautard, R., Cattiaux, J., Yiou, P., Thépaut, J. N., & Ciais, P. (2010). Northern Hemisphere atmospheric stilling partly attributed to an increase in surface roughness. *Nature geoscience*, 3(11), 756-761.
- Venkataramanan, V., Lopez, D., McCuskey, D. J., Kiefus, D., McDonald, R. I., Miller, W. M., Packman, A. I. and Young, S. L.: Knowledge, attitudes, intentions, and behavior related to green infrastructure for flood management: A systematic literature review, *Sci. Total Environ.*, 720, doi:10.1016/j.scitotenv.2020.137606, 2020.
- Vogt, P., Ferrari, J. R., Lookingbill, T. R., Gardner, R. H., Riitters, K. H. and Ostapowicz, K.: Mapping functional connectivity, *Ecol. Indic.*, 9(1), 64–71, doi:<https://doi.org/10.1016/j.ecolind.2008.01.011>, 2009.
- von Döhren, P. and Haase, D.: Ecosystem disservices research: A review of the state of the art with a focus on cities, *Ecol. Indic.*, 52, 490–497, doi:<http://dx.doi.org/10.1016/j.ecolind.2014.12.027>, 2015.
- Von Storch, H. and Zwiers, F. W. (2001). *Statistical Analysis in Climate Research*. Cambridge: Cambridge University Press. <https://doi.org/10.1017/CBO9780511612336>
- Vousdoukas, M.I., Mentaschi, L., Feyen, L., Voukouvalas, E., 2017. Extreme sea levels on the rise along Europe’s coasts. *Earth’s Futur.* 5, 1–20. <https://doi.org/10.1002/ef2.192>
- Vousdoukas, M.I., Mentaschi, L., Voukouvalas, E., Verlaan, M., Jevrejeva, S., Jackson, L.P., Feyen, L., 2018. Global probabilistic projections of extreme sea levels show intensification of coastal flood hazard. *Nat. Commun.* 9, 2360. <https://doi.org/10.1038/s41467-018-04692-w>
- Vousdoukas, M.I., Ranasinghe, R., Mentaschi, L. et al. Sandy coastlines under threat of erosion. *Nat. Clim. Chang.* 10, 260–263 (2020). <https://doi.org/10.1038/s41558-020-0697-0>
- Wilks, D. S. (2011). *Statistical Methods in the Atmospheric Sciences*. International Geophysics Series, Academic Press. Volume 100, pp. 301-394. <https://doi.org/10.1016/B978-0-12-385022-5.00008-7>
- Wu, T., Lu, Y., Fang, Y., Xin, X., Li, L., Li, W., et al. (2019). The Beijing Climate Center Climate System Model (BCC-CSM): the main progress from CMIP5 to CMIP6. *Geoscientific Model Development*. <https://doi.org/10.5194/gmd-12-1573-2019>
- Yeager, S. G., Danabasoglu, G., Rosenbloom, N., Strand, W., Bates, S., Meehl, G., et al. (2018). Predicting near-term changes in the Earth System: A large ensemble of initialized decadal prediction

simulations using the Community Earth System Model. *Bulletin of the American Meteorological Society*. <https://doi.org/10.1175/BAMS-D-17-0098.1>

Yukimoto, S., Kawai, H., Koshiro, T., Oshima, N., Yoshida, K., Urakawa, S., et al. (2019). The Meteorological Research Institute Earth System Model Version 2.0, MRI-ESM2.0: Description and Basic Evaluation of the Physical Component. *Journal of the Meteorological Society of Japan*. <https://doi.org/10.2151/jmsj.2019-051>

Zampieri, M., Ceglar, A., Dentener, F. and Toreti, A., 2017. Wheat yield loss attributable to heat waves, drought and water excess at the global, national and subnational scales. *Environmental Research Letters*, 12(6), p.064008. <https://doi.org/10.1088/1748-9326/aa723b>

Zeng, Z. et al., 2019: A reversal in global terrestrial stilling and its implications for wind energy production. *Nature Climate Change*, 9(12), 979–985, doi:10.1038/s41558-019-0622-6.